Measurement of residual stresses in linear friction welded 18CrNiMo7-6 steel chains

Dinis Garcia Nunes

Thesis to obtain the Master of Science Degree in

Mechanical Engineering

Supervisors: Prof. Maria Luísa Coutinho Gomes de Almeida

Prof. Inês da Fonseca Pestana Ascenso Pires

Examination Committee

Chairperson: Prof. Rui Manuel dos Santos Oliveira Baptista

Supervisor: Prof. Maria Luísa Coutinho Gomes de Almeida

Members of the Committee: Prof. Rosa Maria Mendes Miranda

Eng. Pedro dos Santos Effertz

November 2017

À minha família

Acknowledgements

Resumo

As tensões residuais são as tensões que permanecem num componente após a remoção de todas as solicitações externas. A presença deste campo de tensões numa peça é muitas vezes o principal motivo para comprometer o seu desempenho, fiabilidade e ciclo de vida.

Este projeto pretende avaliar o campo de tensões residuais nas correntes de 18CrNiMo6-7 soldadas por fricção linear ao longo dos principais estágios de fabrico. A condição inicial forjada (antes da soldadura), condição soldada antes de remover o flash, como soldada após a remoção do flash através de um procedimento padrão e após realizar o tratamento térmico. Todas as soldaduras foram realizadas com os mesmos parâmetros para que se possa comparar em detalhe a influência de cada passo do fabrico no campo de tensões residuais. Os métodos utilizados para caracterizar o campo de esforço foram o método do furo cego incremental e a difração de raios x.

A técnica do furo cego incremental mostrou claramente que, independentemente do lado do elo da corrente (esquerda / direita, superior / inferior), o campo de tensão residual era o mesmo independentemente da geometria não axi simétrica das correntes. Campo de tensões na direção x é de tração perto da linha de soldadura. Longe da linha de soldadura, não foram observadas diferenças significativas entre a condição forjada e soldada. A remoção do flash não provoca diferenças significativas no campo de tensões. Os resultados da difração de raios x não mostraram variações significativas em nenhuma das condições avaliadas.

Palavras-chave

Tensões residuais; Correntes; Perfuração Cega; Difração de Raios-X; Soldadura por Fricção Linear

Abstract

Residual stresses are the stresses that remain in a component after removing all the external solicitations. The presence of this stress field in a part is often the main reason for compromising its in-service performance, reliability and life extent. They can also influence negatively the fatigue strength of a component, stress corrosion cracking and the crack propagation velocity itself. Therefore, knowing its magnitude and nature in detail, is an important matter to assure the pretended attributes during the whole life of a component.

Four different manufacturing stages of Linear Friction Welded chains were investigated: "As Forged", "As welded with flash", "As welded without flash" and after post weld heat treatment. The methods used to characterize the residual stress field were the hole-drilling and x-ray diffraction.

The results from the hole drilling technique clearly showed that independently from the side of the chain link (left or right) the residual stress field was the same. Also between the top and bottom regions of the chain link, symmetry was observed regardless the non-circular geometry of the chains studied. Close to the weld centre line, the compressive stresses in the "as forged" condition switched to tensile due to the welding process. Away from it, any significant changes were observed between "as forged" and "as welded without flash". No changes were observed in the flash removal process. The PWHT uniformizes the residual stress field along the whole weld region. The x-ray diffraction results did not show relevant changes between each of the conditions studied.

Keywords

Table of Contents

List of Figures

List of Tables

Nomenclature

RS	Residual stresses
AISI	American Iron and Steel Institute
SAE	Society of Automotive Engineers
DIN	Deutsches Institute für Normrung
BCC	Body-centred cubic
FCC	Face-centred cubic
BCT	Body-centred tetragonal
CCT	Continuous cooling transformation
TIG	Tungsten Inert Gas
ERW	Electrical resistance welding
RPW	Resistance projection welding
HAZ	Heat affected zone
RFW	Rotary friction welding
OFW	Orbital friction welding
FSW	Friction stir welding
LFW	Linear friction welding
FW	Friction welding
EDM	Electrical discharge machining
ESPI	Electronic speckle pattern interferometry
DIC	Digital image correlation
TMAZ	Thermomechanical affected zone
HD	Hole drilling
HSS	High strength steels
WCL	Weld center line
TL	Top Left
TR	Top Right
BL	Bottom Left
BR	Bottom Right
LS	Left Side
RSi	Right Side
DT	Destructive tests
SDT	Semi destructive tests
NDT	Non-destructive tests
PWHT	Post-weld heat treatment
BCC	Body cubic centered
FCC	Face cubic centered
SMAW	Shielded metal arc welding
OFW	Orbital Friction Welding
IFW	Inertia Friction Welding
WZ	Weld Zone
F	As forged initial condition
A	As welded with flash

N	As welded without flash
P	As welded without flash after PWHT
MCL	Material Center Leoben Forschungs GmbH

Chapter 1 - Objectives

The purpose of the present work is to access the differences in the residual stress field due the linear friction welding process, due to the flash removal and due to post welding heat treatment. To account the needs of a real industrial application the following objectives were established:

- Investigate the importance of knowing the extent of the residual stress field present in a component.

- Understand the advantages of the linear friction welding process relatively to most commonly used processes to join chain links.

- Understand the differences and applicability of methods that are used to residual stress measurements – Destructive Tests (DT), Semi-destructive Tests (SDT) and Non-Destructive Tests (NDT).

- Evaluate the reliability of the results obtained through the hole drilling and x-ray diffraction techniques, and ultimately correlate them. Understand the influence of the residual stress (RS) field in the in-service conditions and identify problems that may arise from them.

- Evaluate the residual stress field present in the as forged condition and understand the stress state evolution throughout the manufacturing process.

- Evaluate the applicability and reliability of the linear friction welding process in production of steel chains by studying the influence of the process in the residual stress field.

- Identify the microstructural differences in the different manufacturing stages.

- Evaluate the microhardness of the different weld zones and understand the effect the post weld heat treatment has on it.

- Evaluate the influence of the post welding heat treatments applied in the case of this steel alloy in the residual stress field.

Chapter 2 - Introduction and reading guide

2.1 Background

Joining steel components has been one of the most important manufacturing processes in industry since the steel demand worldwide keeps increasing until the present day. Although the usage and development of lighter, equally resistant, and not so harmless to the environment materials is also increasing, there are many applications where the use of steel is inevitable. Therefore, joining and forming steel are and will be, at least in a recent future, one of the biggest sources of investigation and research.

The first welds of metallic material date back to the Bronze Age. Since the beginning of the 19th century a lot of favourable discoveries to this topic have been made. Nowadays, optimizing the performance of a component by enhancing its relevant characteristics and reducing its costs is a top priority to most engineering industries. Therefore, discovering new joining processes and improving the existent ones is until this day a great topic of discussion [1].

Due to all the facts mentioned before, solid-state welding processes have seen an increasing development in its scope of applications since it has numerous advantages when compared to other commonly used joining processes. It does not require fluxes, protection gases or filler materials which traduces in a substantial reduction of costs. When reporting to Linear Friction Welding (LFW), the industrial applications of the process were limited for a long time to joining turbine blades to its disks (blisks). Most recently, in 2007, relevant investigation was conducted in the application of LFW to near-net-shapes, due to the ability of material cost reduction up to 90% when compared to traditional machining procedures [2]. Nowadays, the industry is focusing in the improvement of the productivity without compromising the performance of the component. Therefore, LFW scope of applications is increasing, since it provides superior quality welds (when compared to the resistance welding processes commonly used in chains) in a much more reduced timespan. Since solid-state welding processes bring many advantages when compared to conventional ones, multiple industries are studying the possibility to use LFW in their production chain. These facts make the knowledge about the residual stress field in this type of welded structures an important subject of investigation. The welding parameters for the investigated case were already optimized. Thus, it is not necessary to inspect this topic. If it is pretended to research different LFW applications these parameters should be evaluated and optimized [1], [3].

This work intends to study the residual stress field in the main different stages of steel chains` manufacturing: as forged initial condition, as welded condition without removing the flash, as welded condition after the flash is removed through a standard procedure and after the post welding heat treatment (PWHT) is applied. The methodologies used to measure the residual stresses are: the hole-drilling (HD) technique, which is an invasive method and allows measuring the stress state in a region close to the surface of the component; whereas the x-ray diffraction (XRD) method measures the stress field without damaging the specimens used. These methods were chosen considering its suitability for the case and the equipment available at the institution where the investigation was performed. It was

also taken into consideration that the data provided by HD at the surface of the specimens, is more susceptible to measurement errors. In such wise, both tests complement each other. The results obtained are thus compared and a correlation is established in order to acknowledge which one yields the most reliable results. Since there is no literature available related to residual stress measurements in this LFW steel alloy 18CrNiMo7-6, the work serves the intent to positively contribute to the lack of knowledge on this subject, as well as to expand the applications of the LFW process.

2.2 Reading guide

This section contains a brief description of the main topics covered in this dissertation. Primarily, the literature review presented in chapter three, provides an overview about the investigation already done in the subject of this thesis. This review is subdivided in 6 sections: 1) Classification and nomenclature of steel alloys by its chemical composition since the chemical composition of the material can directly influence its weldability and residual stresses; 2) An overview of the LFW processes and its applicability to the case studied when compared to the previously used resistant ones; 3) This section presents a comparative analysis of the different methods available to measure residual stresses. It is evaluated the suitability of each method to this project; 4) In the fourth section it is provided detailed information about the destructive technique used in this thesis (Hole-Drilling) to measure residual stresses. It is also explained the advantages of integrating optical measurement techniques in measurements of this nature; 5) Explains the theory behind the non-destructive method used (XRD); 6) The last section presents an analysis of different PWHT since it is pretended to study its influence in the residual stress field of a welded component.

The experimental procedure is reported in the fourth chapter of the thesis and it is divided in 3 main categories: 1) The workplan is described in a flowchart to easily understand the work stages that were followed in the project; 2) The second section states all the terminology used related to the location of the measurements and the manufacturing conditions of the chains; 3) the third and last section refers to the material and procedures followed in the residual stresses measurement.

All the residual stress results obtained throughout the project are shown and discussed in chapter 5 comprising five main topics: 1) Residual stress field in the as forged initial condition; 2) Analysis of the residual stress field in the as welded condition where it was proven that the welding process induces nearly the same residual stresses in all the locations of interest (symmetry); 3) Influence of the flash cutting on the residual stress field; 4) Analysis of the residual stress field after performing PWHT; 5) The last section of this chapter comprises the microstructural results obtained. A microhardness profile of the weld regions is also presented.

Ultimately, in the sixth chapter the conclusions obtained and future work developments relevant to this subject are addressed.

Chapter 3 - State of art of the problem under study

3.1 Classification of alloy steels by chemical composition

The steel alloy used to produce the chains studied in this dissertation has no specific classification through the American Iron and Steel Institute (AISI) standard but it is known by its Deutsches Institut für Normung (DIN) designation of 18CrNiMo7-6. The first number in the DIN standard always describes the carbon content with an applied multiplier of x100. The following numbers describe the percentage of the main alloying elements in the material. In this case, they are Cr and Ni (both with a x4 multiplier). The percentage of Molybdenum is unspecified [4]. The steel alloy used in this dissertation is a bainitic/martensitic steel alloy which can comprise some weldability problems that will be explained in the following section.

3.1.1 Martensitic steel alloys and their weldability

Iron is the best representation of allotropy in a metal. At atmospheric pressure, it is possible to identify three main allotropic forms: Ferrite which is subdivided in the δ or α iron form and austenite (γ iron). Delta-ferrite can be considered the high temperature form of iron. It is formed when the molten metal solidifies (at around 1500ºC) and presents a body-centred cubic (BCC) structure. When cooled further, the BCC structure changes to a face-centred cubic structure (FCC) and austenite starts to form. When this austenitic steel is slowly cooled, and therefore carbon is diffused outside of the alloy, α-ferrite forms and it is still evident at reference room temperature. Upon slow cooling (below 727ºC) of hypereutectoid steels (high carbon content), the still present carbon atoms react with iron ones, forming cementite (Fe_3C). When this precipitation of carbon occurs contiguously with ferrite formation, a constituent called pearlite can be identified [5]–[7]. When cooled until the range of 250-550ºC at a faster rate than to form pearlite, an intermediate form appears which is bainite. It can be considered intermediate because it forms at a faster cooling rate than pearlite but still slower than the one to obtain martensite. Martensite forms when a steel is cooled at a very high cooling rate (quenched). The austenitic microstructure (FCC) transforms into a body-centred tetragonal (BCT) structure which is highly strained. Since it cools at such a high rate the possibility of carbon to diffuse outside of the structure is greatly narrowed. The resulting shear deformations promote large dislocations which are considered to be the primary mechanism in steel strengthening [5] [8].

The martensite formation mechanism results in a very hard steel alloy, and therefore brittle, that still comprises great mechanical properties including corrosion resistance. Thus, martensitic steels are required in more challenging environments such as the application studied in this dissertation (conveyor 18CrNiMo7-6 steel chains).

Due to these facts, joining martensitic steel alloys has limitations and requires expertise in the choice of the welding process and joint preparation (which lowers the productivity). Steel producing companies provide information about this grade high weldability by fusion welding. This class of processes present numerous disadvantages when compared to friction techniques, as it will be explained in the next chapter. Some measures can be followed to lower the hydrogen intake, such as optimization of the

welding parameters (electrical stick-out is a relevant example) or using low hydrogen intake hydrogen electrodes [9]. The high production rates needed and the sensitivity to cracking in the case studied, turn resistance welding processes into the most used process until the 21st century in this application.

3.2 Steel welding

The steel demand worldwide keeps increasing every year. The requirements for the best performance and reliability is also gaining more importance day by day. Even with the improvement of previously existing materials and the development of new ones, the manufacturing of the best steel structures can still bring though complications to surpass. Therefore, the joining of these structures and the discovery of new procedures to do it, is until the present day, a very important subject of investigation. Welding steel presents some issues that should be addressed. Such as the composition and properties that the base material presents. The welding process should be chosen wisely in terms of cost, effectiveness and productivity. The material(s) used should also be known in detail to avoid weldability problems that may arise.

Until the beginning of the twentieth century, steel bonding was mostly made through brazing and acetylene open flames. Although the previously mentioned ones were important milestones in the development of welding technology, the discovery of shielded metal arc welding (SMAW), was a big breakthrough in the development of new processes. Although these processes were important in the evolution of welding processes, the weld quality was not still good enough to be used in structures with high responsibility. This last disadvantage mentioned was surpassed with the introduction of Tungsten Inert Gas (TIG) welding in the 1940s. Even providing good quality welds, this process revealed itself not economical for thick specimens where MIG is more advantageous [2],[3],[12].

It is of common knowledge that having a successful result in welds performed by fusion processes depends greatly on the surface preparation, pre/post weld heat treatment, surrounding conditions and the operator experience depending on the process chosen. Therefore, the use of friction welding processes allows to eradicate common problems in fusion ones such as hot cracking, porosities and slag inclusions. It also narrows the heat affected zone (HAZ) while allowing to diminish the bottleneck in the productivity at the same time due to undoubtedly lower cycle times [2],[13].

3.2.1 Linear friction welding

The first patent of the LFW process dates back to 1929. The relevant documentations about the process that followed it, were mostly about the reproduction of the linear reciprocation movement itself instead of the welding technology. The first major industrial application of the process was joining aero-engine compressor blades to its disks, the so called "blisks". This fact made the research about commercial applications of the process to focus greatly on this type of components. There were also perceived great advantages in the application of LFW to join near-net shaped components.

It is common knowledge that linear friction welding consists in a solid-state joining process where a moving part generates frictional heat against a stationary one due to reciprocate linear movement. This

frictional heat and the forging pressure applied transversely to the weld interface plasticizes the materials to be joined. Being a solid-state welding technology, as all the other friction welding processes, it does not involve the melting of the materials to be bonded which comprises great advantages in the reliability and performance of the components [5],[15]. The following Fig. 1 illustrates clearly how LFW is performed:
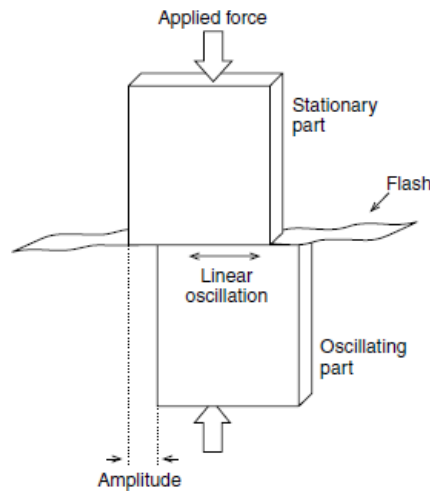
Figure 1 - Relative movement of both parts in linear friction welding

In LFW there are determinate stress conditions that must be achieved at the interface of the weld and in an adjacent region to it so the process undergoes its various phases correctly. Therefore, the whole process is performed under load control. LFW can be subdivided in four stages as it follows:

1. *Initial phase:*

At the beginning of the process, both parts to be joined are brought together under contact with each other. The true contact area of the parts increases during this phase of the process. The moving component oscillates linearly in a reciprocate manner to create frictional heat. Sufficient frictional heat should be generated to achieve the thermal softening pretended considering the radiation and conduction losses to the environment.

2. *Transition phase*

During this phase, if enough heat was produced to soften the material at the interface, big particles are expelled from it. The contact area between the two cross sections is 100% and due to the previously plasticization of the in-contact layers, the components stop supporting the axial force exerted.

3. *Equilibrium phase*

This is the stage of the process where the axial shortening of the pieces occurs due to the expelled material. This material is extruded outside from the WCL due to the reciprocate oscillatory movement creating the so-called flash. It is important to assure an even distribution of the heat so that the plasticized zone is not too big and the correct amount of material is extruded.

4. Deceleration phase

In this phase, the oscillatory motion stops abruptly and the forging force is applied to the joined component to consolidate the joint. This forging force is usually higher than the friction force and it is applied to the stationary component [8],[15]. The sequence of the phases of the process are illustrated in Figure 2.
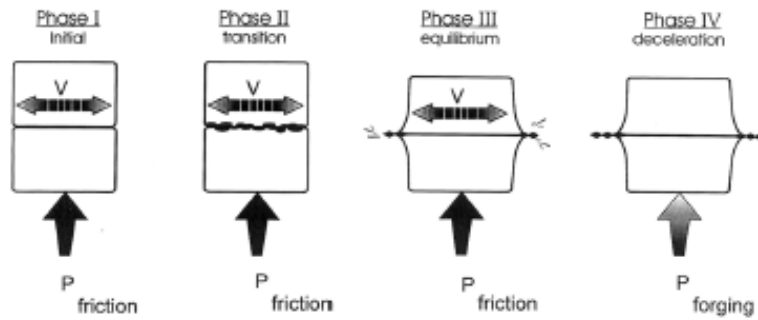
Figure 2 - Four stages of the LFW process

3.2.2 Linear friction welding equipment

The LFW machines consist mainly in two mechanisms: one that allows the oscillatory movement of one of the parts and a further one that permits exerting the forging force in the remaining part. The latter is always achieved by hydraulic means while the first one mentioned can be obtained either by mechanical or hydraulic systems. The following Figure 3 show an example of a hydraulic-type LFW machine and a schematic diagram of the hydraulic oscillation mechanism respectively. The hydraulic system consists mainly in the following components:

- A pump that makes the high-pressure hydraulic fluid flow into a stack of accumulators;
- A valve that allows the movement of the pressurized fluid;
- A cylinder-piston assembly to where the fluid flows through the valve that allows the creation of the reciprocate linear movement;
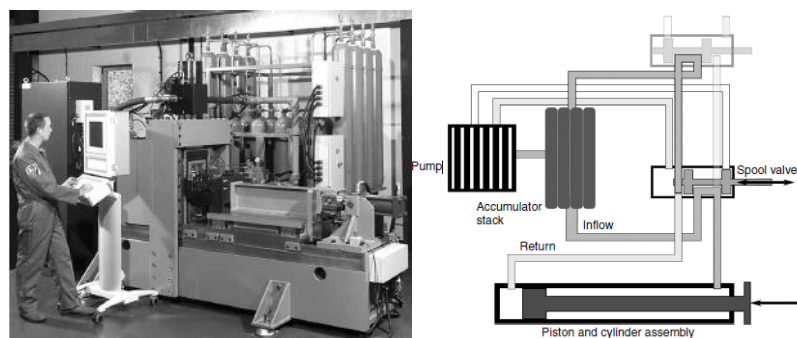
Figure 3 - Hydraulic LFW machine and respective hydraulic circuit

3.2.3 Process parameters in LFW

The main input variables of the process, whose typical evolution is shown in Figure 4, that can be easily adjusted and have been subject of the most thorough investigation are [15] the following:

- Frequency (number of oscillations per time unit);
- Amplitude (maximum displacement of the moving part relatively to the stationary one);
  - For the welding conditions to be achieved, the minimum power input required depend greatly on these two variables;
- Friction pressure (Applied pressure in the friction phase – This pressure is calculated using the nominal contact area at 0 amplitude);
- Burn-off distance, time or cycles (defines the axial shortening of the components until the start of the forging phase);
- Forging pressure (force applied during the forging phase);
- Forging time (timespan in which the forging pressure is applied);
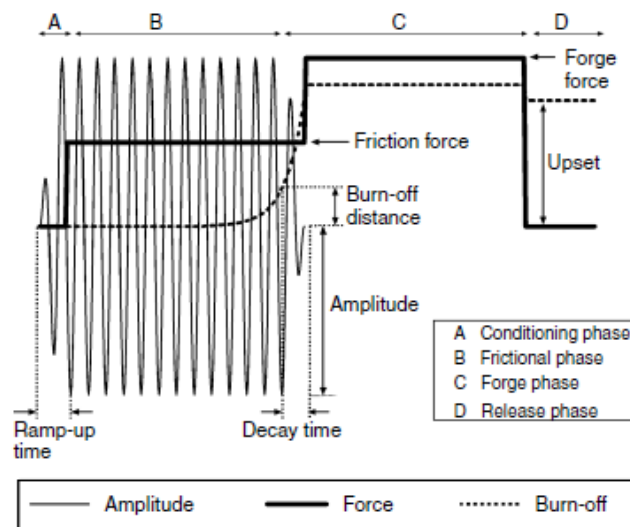
Figure 4 - Typical parameter evolution in a LFW process

Source: [15]

There are also important variables in the process that are a consequence of the ones mentioned above. These consequential ones, that are listed below, can't be changed with the necessary precision by adjusting the main input variables.

- Upset: The total shortening of the workpieces (the sum of the shortening in the equilibrium phase and the forging phase);
- Shear force (the force in the same direction of the oscillatory motion);
- Burn-off rate (the rate at which the shortening of the specimen occurs);
- Welding time (the total timespan taken to weld a component);

It was stated by *Bhamji et al.* [15] that higher forging pressures caused a decrease in the welding temperature peak due to the larger amount of flash expelled. A LFW titanium alloy was investigated in

1998 by *Vairis et al.* where it was discovered that the size of the HAZ was inversely proportional to the friction pressure applied [16]. Another author performed investigation with the same alloy and disclosed that the forging pressure used during the process had great influence on the residual stresses in the weld plane [17].

3.2.4 Heat input model of the process

As explained in [18], the shear stress that is applied at the interface of the weld can be defined by

$\tau = \mu P_N$

Where μ is the friction coefficient related to the rubbing of both parts and P_N is the pressure exerted in the normal direction to the WCL. The heat generation rate per unit of area and cycle can be described as in equation 3.2.1:

$$q = \tau v \tag{3.2.1}$$

Where v is the imposed rubbing velocity of the moving part. By combining the prior two equations, we obtain

$$q = \mu P_N v \tag{3.2.2}$$

for the heat generation rate. Although the exerted force remains constant during the process, the contact area of the interface oscillates. This makes the normal pressure P_N oscillate as well since it is described by the following:

$$P_N = \frac{F_{fr}}{Oscillating\ cross\ sectional\ area} = \frac{F_{fr}}{W(L - \alpha \sin(\omega t))} \tag{3.2.3}$$

Where F_{fr} is the frictional force exerted, W and L are the dimensions of the specimen (width and length respectively) and t is the time in which the oscillation occurs.

It is also known that the friction velocity varies with the following sinusoidal behaviour:

$$v = \alpha \omega \cos(\omega t) \tag{3.2.4}$$

Where ω is the angular velocity of the oscillatory movement and α is its amplitude. Thus, the heat generation rate of the process becomes:

$$q = \frac{\mu F_{fr} \alpha \omega}{W} \frac{\cos(\omega t)}{L - \alpha sen(\omega t)} \tag{3.2.5}$$

3.2.5 Microstructural characterization in LFW

All forms of friction welding process, such as LFW, orbital friction welding (OFW), and Inertia friction welding (IFW) present the same different microstructural regions: The weld zone (WZ), the thermomecanically affected zone (TMAZ), the HAZ and the base material (BM). The following Figure 5 shows these regions distinctively:
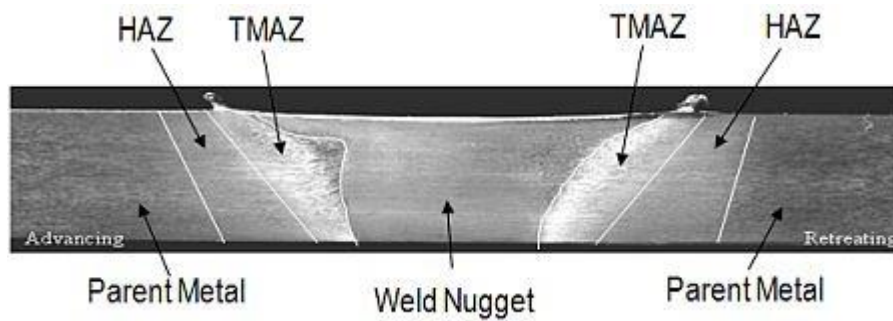
Figure 5 - Example of a typical weld zones in a FSW steel

The BM is characterized for not suffering any plastic deformation, nor changes in its microstructure and mechanical properties, due to the thermal cycle of the weld.

The TMAZ, as the name indicates, is an area where the welded material suffers moderate plastic deformation and some microstructural changes due to the thermal cycle. Even though recrystallization does not occur in this zone. In this region, the deformation observed in the grains is bigger than in the HAZ and more elongated grains can be observed. The size of this region is not straightforward, therefore a micrographic and hardness analysis is necessary to have a rigorous characterization [2],[19].

The HAZ is the region in which the material suffers alterations in its microstructure and mechanical properties although there is no plastic deformation. This happens due to its relatively small distance to the WZ that is enough to allow the region to be affected by the thermal cycle [2],[19].

The WZ is the only zone of the previously mentioned ones that is characterized by recrystallized grains and metallurgical phase transitions due to the high plastic deformation and temperatures reached [2],[19].

3.2.6 Manufacturing of steel chains

Steel chains as we know them, have been manufactured the same way since the beginning of the 20th century. A steel wire with the desired diameter is bent so the sides face each other, and the link is then joined with an energy intensive welding process. Most commonly, flash-butt welding for higher diameters. In flash-butt welding, the components to be joined are brought together end-to-end and the machine discharges a very high-density current in each part. This action makes the molten material blow out of the weld centre. This process can be subdivided in three phases: preheating, flashing and upsetting or butting [20], [21].

Although resistance welding processes provide good quality welds and allow the welding of multiple materials, in flash-butt welding the microstructure of the material is affected negatively in the HAZ since it is a fusion process [22]. The main advantages of this process are listed below.

- ✓ Not necessary to have skilled workforce (**present in LFW as well**);
- ✓ High quality welds obtained (**surpassed by LFW**);
- ✓ Can join a wide range of materials and shapes (**same as friction welding processes**);
- ✓ Contaminants are squeezed out of the weld (**the movement of the workpiece in LFW**

provides a similar benefit);

As mentioned above, there are a lot of inherent advantages of using a FW process instead of a fusion one. The suitability of LFW to the manufacturing of chains is being studied by Pewag Austria to refine the production of the next generation of chains [23]. Fig. 6 shows an illustration of the process applied to the chains manufacturing.

Figure 6 - LFW process applied to "hero" steel chains

These LFW chains are produced from forged half links instead of drawn steel wire or rolled bars. Besides the advantages mentioned before, every chain application has its own purpose. This fact makes the illimitability of shapes in LFW another big pro. As it is shown in the following Figure 7, the contact area in these "Hero" links is bigger than in the common round one. The "hero" link has the lifetime and the wear resistance increased by around 30%´
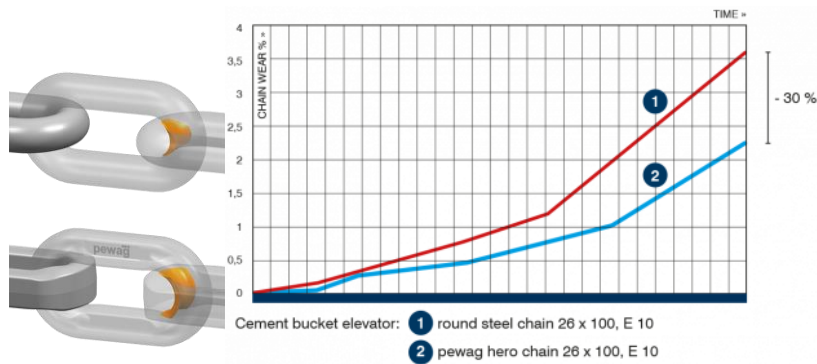
Figure 7 - Illustration of the increased wear resistance in "Hero" chains compared to round ones

3.3 Methods to measure residual stresses and its classification – comparative analysis

Residual stresses are loads that remain in the component even after the external solicitation was removed. Therefore, the specimen must be globally balanced when regarding to stresses:

$\int \sigma dA = 0$ where σ is the solicitation at a given point and dA is an infinitesimal area variation in the welded component. The residual stresses can be classified as suggested in [24].

1. Macro Residual Stresses – These stresses result in changes in macroscopic dimensions. They have

a bigger dimension than the grain.

2. Micro Residual Stresses – They have a scale smaller than the grain size.

3. Micro Residual Stresses II – Mainly caused by crystalline defects such as dislocations or vacancies. They exist within a grain. [25] [26] [27].

These stresses may be advantageous or not depending on the application, which justifies the need of understanding its behaviour and evolution attentively. Hence, it should be remembered that residual stresses in a welded structure are dependent of a great variety of factors since these stresses contain information about the full history of the part from material manufacture to all the following operations performed on the component as suggested in [28]. These factors include: the already existent residual stresses in both parts to be joined, the welding process and materials used, the geometrical restrictions and the ones imposed upon welding [29] [30].

3.3.1 Classification of methods to measure residual stresses

The methodology to measure residual stresses is usually classified considering the amount of damage that causes to the specimen. It is commonly divided in Destructive Tests, Semi Destructive Tests and Non-Destructive Tests.

-DT which count on the measurement of the deformation release upon cutting and material removal, damaging irreversibly the specimen of study. In this group, not only stress and hardness tests may be included but also tests with metallographic nature.

-SDT use the same principles as destructive tests nonetheless only a small amount of material is removed, therefore the overall integrity of the part is maintained. This group includes key-hole drilling and deep hole drilling.

-NDT as the name suggests does not damage the specimen and includes X-ray, neutron and electron diffraction. Magnetic and ultrasonic methods may also be included in this group [28].

The following Fig. 9 shows a comparison of the principal methods used to measure RS. The tests are compared by amount of removed material and the in-depth stresses that are possible to measure.
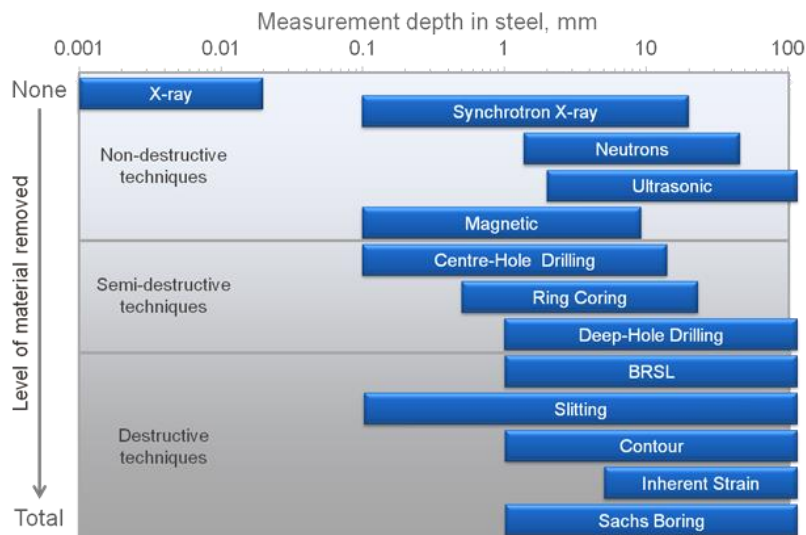
Figure 8 - Comparison between the main methods to measure RS

3.3.1.1 Destructive Tests

Sectioning

The sectioning method fall in the category of destructive testing since they damage the specimens completely. Therefore, it is always profitable to avoid this type of tests when NDT or SDT can be applicable. The sectioning method relies on the same fundaments as the methods explained before. It consists in removing a strip from the material analysed which reliefs the strains. Through that strain relief it is possible to measure the residual stresses that remain in the specimen [24] [26].

Countour

The contour method has also a much more complex implementation since it involves cutting through the full thickness of the specimen using a wire EDM machine which carries much bigger costs than the other methods mentioned before.

The measurement of residual stresses in friction welded structures has been broadly studied in a wide range of materials like aluminium, titanium, steel and stainless-steel alloys. The most widely used method to measure them has been for decades the afforementioned sectioning method since it is an accurate and economical method. However, the technological advances gave the scientific community the possibility of performing these tests with minimum material damage with semi destructive tests and non-destructive tests [24] [26].

3.3.1.2 Semi-Destructive Tests

Ring-core method

The ring-core method involves drilling a ring, as the name suggests, around the strain gauge rosette and posteriorly measuring the strain relief in the core of the drilled ring. This ring has typically 15 mm to 150 mm inner diameter and can be done with a suitable cutting tool, like a ring saw [31]. Figure 10 illustrates the ring core method apparatus. The residual stresses are acquired through strain-gauge

rosettes. They are calculated using mathematical functions (specific for each strain-gauge) and the derivative of the relaxed strains.
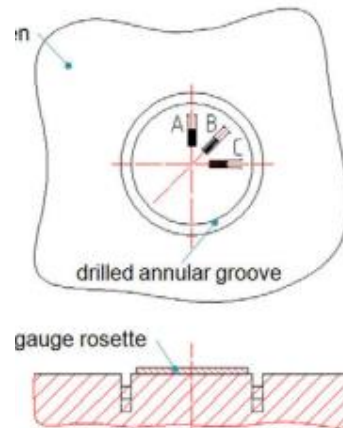
Figure 9 - Ring-core method apparatus

It is a method of relatively easy implementation, good accuracy and the residual stresses that can be measured are up to values of the yield strength of the material. Due to the geometry restrictions, it is not a reliable method to measure the stresses in the type of chains studied although it could be a reliable option in many other cases.

Deep hole method

The deep hole method is a way of measuring in depth residual stresses. It is basically composed by 4 steps: step 1 consists in drilling a reference hole. In step 2 the diameter of the reference hole made in step 1 is measured accurately in various angular positions. On the 3rd step a column of the metal that contains the hole done in step 1 is removed usually recurring to EDM. Finally step 4 involves measuring the distortion of the hole in the same depths and angular positions as in 1.. This method was not chosen due to the lack of equipment available in the institution where the research was performed. It was also considered that the damage caused to the specimen is much bigger than in other suitable SDT solutions. The test also comprises high costs not only on the EDM equipment as well as in the number of samples necessary to evaluate the stresses as pretended. Since one sample would not allow to measure the stresses in different regions [32].
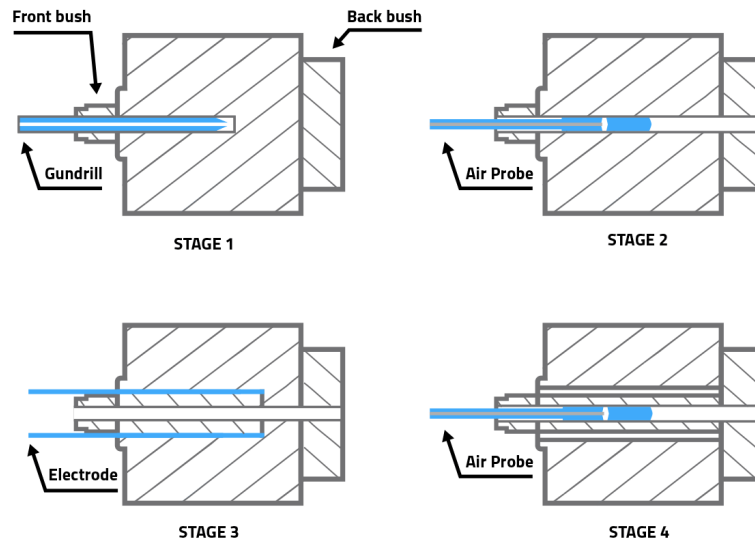
Figure 10 - Deep-hole drilling method apparatus

Hole Drilling

Regarding the scope of this dissertation, the most suitable mechanical method to measure residual stresses is the hole drilling method, which will be thoroughly discussed in the next chapter. The method is characterized for being the cheapest and most practical to implement, thus providing reliable and useful information about the residual stresses near the surface of the chain. Considering the application of the chains studied, it is known that crack initiation sites are regions where the highest stress concentration factors are obtained. Previous investigations concluded that the junction of the linear friction welded component with the flash, was prone to be one of those crack initiation sites. Hence, the residual stresses at the surface of the chains are critical to the stress concentration factor in these regions. It should also be considered that regions with high stress concentration factors are prone to initiate the fatigue fracturing process. This is another reason that highlights the importance of analysing the residual stresses near the surface of the component. Therefore, all the methods that can measure the residual stresses inside the components thickness can be considered irrelevant to the case of this dissertation. They usually also entail more expenses. To sum up, Table 2 presents the pros and cons of DT and SDT methods.

Sectioning	Contour	Ring Core	Deep hole	Hole drilling
-Accurate	-Accurate	-Accurate	-Accurate	-Accurate
-Reliable	-Reliable	-Reliable	-Reliable	-Reliable
-Standardized procedures	-Involves precise cutting often with EDM	-Standardized procedures	-Standardized procedures	-Standardized procedures
-Strip of material is removed which also implies greater damage to the specimen	-Much more expensive to implement	-Easy/cheap implementation	-Suitable to measure interior stresses	-Easy/cheap implementatio n
	-Much more time consuming	-Larger damage to the specimen than simple HD	-Larger damage to the specimen	-Small damage to the specimen

Table 1 - Pros and cons of semi destructive and destructive methods

3.3.1.3 Non-Destructive Tests

Ultrasonic

Ultrasonic residual stress measurement (URSM) relies on the acoustic-elasticity properties of a given material. It consists in measuring the sound velocity in a solid with two transducers, a transmitter and a receiver at a known distance. The velocity is measured through the time that the sound wave takes to cross the material. There are mainly two forms of receiving an ultrasonic wave: by reflection, where there is used only one transducer that acts as the transmitter and receiver as well as a reflector. Or by attenuation where a transmitter is placed on one side of the component and the receiver accounts the amount of sonic radiation that gets there [33]. This makes it possible to find defects in the interior of the part as illustrated in the figure 4 below. To measure residual stresses through the thickness of a component both longitudinal and shear waves can be used. The first ones are used mainly to measure stresses present in the thickness direction and shear waves are used to measure stresses in parallel direction to the surface of the specimen.
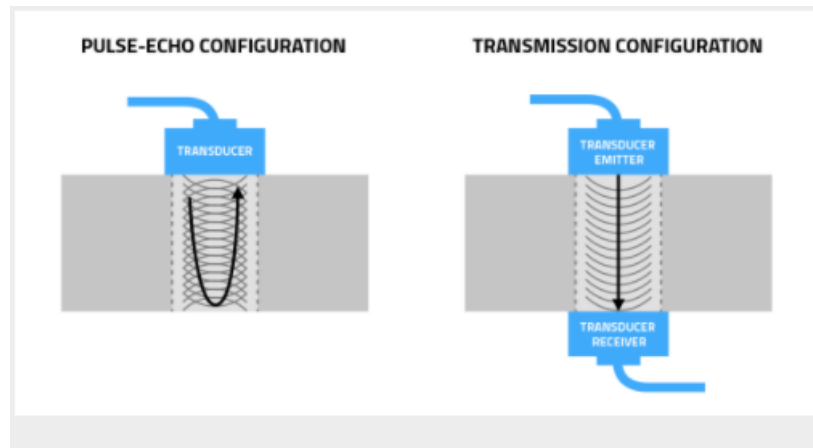
Figure 11 - Ultrasonic residual stresses measurement - Pulse echo and transmission configurations

The speed of ultrasonic waves is also dependant of the temperature and microstructure of the material. Therefore, the propagation time of an ultrasonic wave through a specimen is given by: $\Delta t = \Delta t_{AS} + \Delta t_{RS} + \Delta t_m + \Delta t_t$. Where Δt_{AS} is the change in propagation time due to applied stresses, Δt_{RS} is the change due to residual stresses, Δt_m is the change due to microstructural modifications and Δt_t corresponds to the change of time due to temperature changes [34].

The main reasons for URSM tests not being suitable to the case studied are listed as the following:

- Very sensitive to microstructural changes;
- Gives an average measurement in a large volume (which is not pretended);
- Not applicable to components with a complex shape (chains have an irregular shape);
- Requires a good surface finishing of the component which is not the case;

Neutron Diffraction

Relatively to NDT, neutron diffraction technique is a really powerful experimental tool to characterize residual stresses in the interior of solids. Although the data obtained can be extrapolated to the surface results. This data comparison between XRD and neutron diffraction is shown below on Figure 12. This method comprises a penetration power about three orders of magnitude higher than the conventional XRD method. It can focus on a specific lattice plane spacing of a group of grains, therefore it is also able to analyse the differences of separation of those planes in multiphase materials. Whatever the composition of the material, this method provides information about the strain response of each one of those faces, either in duplex stainless steel (50% austenitic and 50% ferritic) or composite materials, that are also multiphasic, as an example. Unfortunately, the only kind of neutron sources with enough power to provide strain measurements in the pretended way rely on nuclear reactors with neutron beam tubes and spallation neutron transmitters. Therefore, it wouldn't be possible to access such equipment at the given time [35].

Fonte: [36]
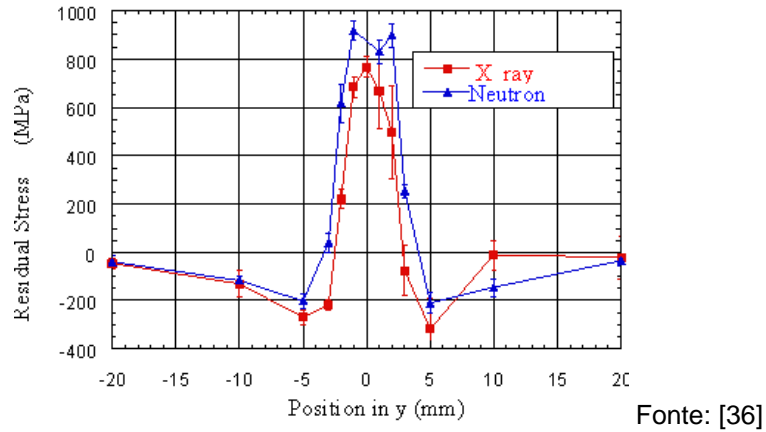
Figure 12 - Comparison between XRD and neutron diffraction residual stress results in a LFW wasp alloy

Taking all these explanations into account, and the result comparison in the figure above, the most suitable NDT is x-ray diffraction since the stress analysis with interest remains at the surface of the component. It is also practical to implement regarding the availability of the equipment and the nature of the component/material studied. This test will be explained in detail in the chapter 3.4 below. The following table summarizes the pros and cons of each NDT technique evaluated.

Ultrasonic measuring	Neutron diffraction	X-ray diffraction
Much more effective in determining interior residual stresses.	Neutrons penetrate the thickness of the material easier than the x-ray beams.	Only applicable to crystalline materials.
Requires surfaces with low roughness	More suitable for composites or multiphase material.	Suitable for computing strain fields in two or three dimensions.
Much more expensive than the others to implement		Possibility to monitor phase transformations.

Table 2 - Pros and cons of non-destructive techniques

3.4 Hole drilling and integration of optical techniques

The first use of Hole drilling as a method to measure residual stresses, dates back from 1966 [37]. When comparing to other conventional methods of measuring residual stresses, hole drilling is economical, practical and can be applicable to the majority of materials. As mentioned previously, the method is based on the principle of measuring strain-relief upon material removal. A small hole is drilled on the specimen usually with a cylindrical end-mill, and the deformation is often measured using a strain-gauge rosette [38] [39] . When using this method, the material must be isotropic and its elastic parameters must be known. The machining of the hole should not prejudice the strain measurement. The procedure to execute this test is normalized by the American Society of Testing and Materials

(ASTM) for cases where there is no significant variation of the stresses within the depth of the specimen (which does not happen in most practical cases). They also should not exceed one half of the yield stress. Not only, this fact makes it the only method to measure residual stresses accepted as an ASTM standard [24] but also excludes orthotropic materials from the scope of the test. The norm also contains coefficients for the hole diameter, hole depth and rosette type. It has been constantly revised since its publication in 1981 [40].

3.4.1 Kockelmann's method

In this investigation, residual stresses were yielded using the Kockelmann's method present in the SINT MTS3000 software, and was chosen due to exceptional results and knowledge gathered from previous tests conducted in similar conditions. It is based on the theory that the strain derivative and the distribution of the stress field are directly correlated [41].

1. In the first stage, the calibration functions K_x and K_y are evaluated according to the following equations 3.4.1 and 3.4.2.

$$K_x(\xi) = \frac{E}{\sigma}\frac{d\varepsilon_x}{d\xi} \tag{3.4.1}$$

$$K_y(\xi) = \frac{E}{\sigma}\frac{d\varepsilon_y}{d\xi} \tag{3.4.2}$$

Where ε_x and ε_y are the measured strains by the strain gauge rosette oriented in the direction of the load and transversely to it respectively in an uniaxially loaded specimen. ξ is a relation between the hole depth and its diameter, while E is the Young modulus of the material. These calibration functions are calculated in a simulation model. They can be obtained for all the standard HBM strain-gauges. Below in Figure 13 it is shown the type of strain gages used in this project.

a) Rosette HBM 1-RY61-
    1,5/120S

b) Calibration functions
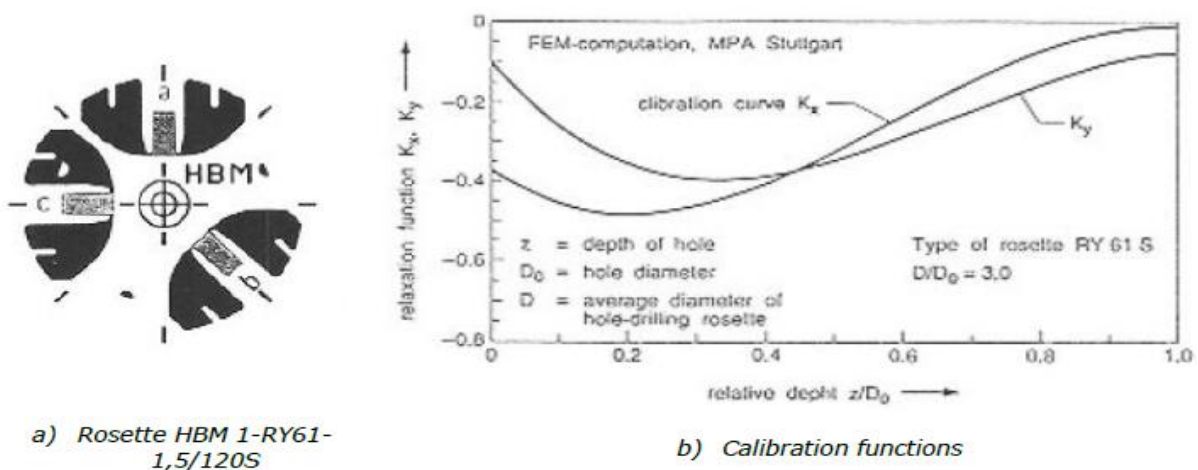
Figure 13 - Example of calculation of the calibration functions for this specific strain-gauge

2. After the calibration functions are obtained it is possible to calculate the stress field using the following relations 3.4.3-3.4.5:

$$\sigma_a(\xi) = \frac{E}{(K_x(\xi))^2 - v^2 \left(K_y(\xi)\right)^2} \left[K_x(\xi) \frac{d\varepsilon_a(\xi)}{d\xi} + \frac{vK_y(\xi)(d\varepsilon_c(\xi))}{d\xi} \right] \qquad (3.4.3)$$

$$\sigma_b(\xi) = \frac{E}{(K_x(\xi))^2 - v^2 \left(K_y(\xi)\right)^2} \left[K_x(\xi) \frac{d\varepsilon_b(\xi)}{d\xi} + vK_y(\xi) \left(\frac{d\varepsilon_a(\xi)}{d\xi} + \frac{d\varepsilon_c(\xi)}{d\xi} - \frac{d\varepsilon_{cb}(\xi)}{d\xi} \right) \right] \qquad (3.4.4)$$

$$\sigma_c(\xi) = \frac{E}{(K_x(\xi))^2 - v^2 \left(K_y(\xi)\right)^2} \left[K_x(\xi) \frac{d\varepsilon_c(\xi)}{d\xi} + \frac{vK_y(\xi)(d\varepsilon_a(\xi))}{d\xi} \right] \qquad (3.4.5)$$

The equations 3.4.3-3.4.5 are used to obtain the principal stresses present in the component and the orientation angle by the following relations 3.4.6 and 3.4.7:

$$\sigma_{1,2}(\xi) = \frac{\sigma_a(\xi) + \sigma_c(\xi)}{2} + \frac{1}{\sqrt{2}} \sqrt{(\sigma_a(\xi) - \sigma_b(\xi))^2 + (\sigma_c(\xi) - \sigma_b(\xi))^2} \qquad (3.4.6)$$

$$\alpha(\xi) = \frac{\frac{1}{2\arctan(2\sigma_b(\xi) - \sigma_a(\xi) - \sigma_c(\xi))}}{\sigma_a(\xi) - \sigma_c(\xi)} \qquad (3.4.7)$$

Source: [41]

The hole should be carefully machined to avoid the introduction of errors such as, introducing stresses due to the machining of the hole that add to the already present residual stresses; geometrical irregularities in the hole (not being completely cylindrical); and the eccentricity of the tool [24].

The test has been permanently progressing in its main features: drilling methods are evolving until the present day. Strain measuring procedures have also developed from using mechanical extensometers to strain gauges, and most recently full-field optical technologies, such as electronic speckle pattern interferometry (ESPI) and Digital Image Correlation (DIC). The evolution of computational techniques should also be taken into account, evolving from empirical calibrations to finite-element analysis methods, enabling the possibility of executing a great number of measurements of non-uniform stress fields in a small timespan [39]. There are also numerous published books regarding this measurement technique, comprising good practice guides [42].

3.4.2 Optical techniques used to measure displacements

Optical techniques have been introduced in the measurement of this type of stresses since the 1980s and brought undeniable benefits against the commonly used strain-gauge. Figure 14 illustrates perfectly the difference on the amount of information obtained when using a full-field analysis. Using these techniques in RS evaluation provides advantages since it relies on measurements with no direct contact with the specimens. They are also usually more sensitive than methods based on material removal and

reduced specimen preparation is required. This type of techniques are able to provide full field measurements of displacements and acquiring a huge amount of data to improve the reliability of the results [43].
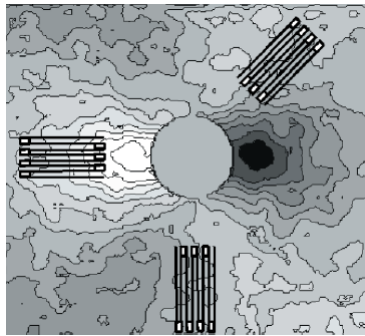
Figure 14 - Comparison of obtained data with a strain gauge rosette and optical techniques

Full-field techniques used in accounting residual stresses can be subdivided in three main categories [44]:

Moiré interferometry,

Finely ruled lines are made on the specimen and symmetrical light beams are pointed to the specimen. The light diffraction will draw dark and light lines that represent the contours of the in-plane displacement [45] [46] [47].

Electronic Speckle Pattern Interferometry (ESPI)

Also called TV holography, combines laser lights with video recording that also gives the possibility of obtaining static and dynamic displacements in fringe form [48] [49].

Digital image correlation (DIC)

Is the third category of optical methods to measure residual stresses. It involves painting a pattern on the specimen and recording it using a high definition camera pointed perpendicularly to the material. It records the pattern before and after the deformation correlating the differences mathematically which allows the calculation of the displacements [43],[50],[51].

There is a variation of this third method where three-dimensional displacements can be measured recurring to the use of a second video recorder. This allows the addition of out of plane deformation. Most of the times this deformation has lower greatness when compared to the in-plane strain. Taking this fact into account measuring the out of plane deformation does not improve the accuracy significantly with some exceptions. This double camera approach was used to compute radial displacements by *D. Thomas et al* [52] . The holographic hole drilling and image correlation hole drilling results were compared and a very good agreement was observed. It was also concluded that merging the conventional hole drilling method with image correlation made it possible to determine uniaxial and biaxial residual stresses in aluminium specimens.

The following Tab. 5 summarizes the advantages and disadvantages of using full-field optical techniques:

Evaluated parameters	Strain Gauge Measurements	Optical Measurements
Equipment cost and cost per measurement	Moderate equipment cost, high per-measurement cost	High equipment cost, moderate per-measurement cost
Test preparation time	Significant preparation and measurement time	Preparation and measurement time can be short
Accuracy	Small number of very accurate and reliable measurements	Large number of moderately accurate measurements available for averaging
Computational power required	Stress calculations are relatively compact	Stress calculations often quite large
Calculation capabilities	Modest capabilities for data averaging and self-consistency checking	Extensive capabilities for data averaging and self-consistency checking
Fieldwork suitability	Relatively rugged, suitable for field use	Less rugged, more suited to lab use
Sensivity to eccentricity of the hole	Sensitive to hole-eccentricity errors	Hole centre can be identified accurately

Table 3 - Pros and cons of using optical techniques

Source: [39]

3.5 X-ray crystallography

In the period between the world wars, x-ray was mostly used in the radiotherapy applications. However, in 1912 the Max von Laue discovered that x-ray beams were reflected and diffracted by crystallographic structures. That achievement was a major breakthrough to the development of new XRD applications. After von Laue's research, William Henry Bragg and his son brought up the first tool to analyse atomic structures through an x-ray beam diffracted by a crystal.

When an x-ray beam is incident on a material. Its atoms will diffract it in a certain way depending on its crystallographic structure. This method has been broadly used to measure residual stresses at the surface of a specimen. When a material is under stress its crystallographic planes have a spacing between them that can be measured through x-ray diffraction (XRD). This measurement will provide the possibility to compute the total stress that is present on the material knowing its elastic constants [24] [53] [54].

Standing in the non-destructive test category, x-ray diffraction is a test that provides information about the crystallographic structure, chemical composition and physical properties of materials. Bragg's formulation of X-ray diffraction was proposed by William Bragg in 1913 [55]. This formulation relates the scattering of an emissive source of x-ray (which has comparable wavelength to the interatomic distance in a crystalline material) with the scattering angle Θ and the spacing between the crystallographic planes d. If residual stresses exist on the sample, then the d spacing will be different from the one in an unstressed sample.

$$2d \sin \theta = n \lambda \qquad (3.5.1)$$

Where λ is the known wavelength of the x-ray and n is an integer. Peaks of very high intensity of radiation known as Bragg's peaks are obtained at points where the condition is satisfied by the Θ angle.

The following figure also illustrates the main principles of XRD where the x-ray beam is incident normal to the surface of the material and with a known rotation angle Ψ between the initial and final position of the normal to the surface.
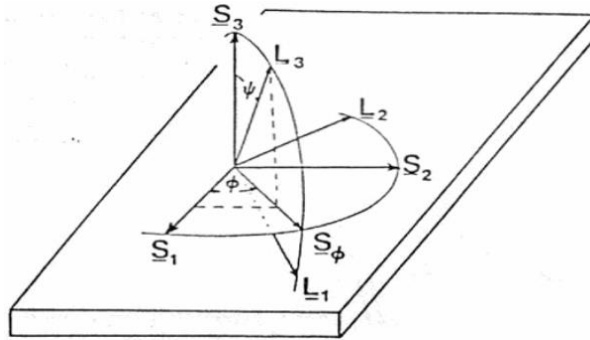
Figure 15 - Illustration of the main variables in X-ray diffraction

Source:[56]

Where S_1 and S_2 are the axes in the plane of the surface of the specimen. S_1 should be defined by the operator of the equipment. S_3 is the axis normal to that plane. L_1, L_2 and L_3 is the coordinate system used in the lab, where L_3 is normal to the lattice diffracting plane and bisects the incident and diffracting beam. Φ is the angle between S_1 and the projection of the normal to the diffracting lattice plane on the surface of the specimen. Ψ is the angle between the normal of the specimen surface S_3 and the normal to the diffracting lattice plane L_3.

The strain in the direction defined by Φ and Ψ can be calculated through the following equation for a crystalline isotropic material and for the family of lattice planes {hkl}:

$$\varepsilon_{\Phi\Psi}{}^{\{hkl\}} = S_1{}^{\{hkl\}}[\sigma_{11} + \sigma_{22} + \sigma_{33}] + \frac{1}{2}S_2{}^{\{hkl\}}\sigma_{33}\cos^2\Psi + \frac{1}{2}S_2{}^{\{hkl\}}[\sigma_{11}\cos^2\Phi +$$

$$\sigma_{22}\sin^2\Phi + \tau_{12}\sin2\Phi]\sin^2\Psi + \frac{1}{2}S_2{}^{\{hkl\}}[\tau_{13}\cos\Phi + \tau_{23}\sin\Phi]\sin2\Psi \qquad (3.5.2)$$

Where $S_1{}^{\{hkl\}}$ and $S_2{}^{\{hkl\}}$ are the elasticity constants of the X-ray diffraction for the family of planes {hkl}. σ_{11}, σ_{22} and σ_{33} are the normal stresses in the directions of S_1, S_2 and S_3 (Fig.8). τ_{12}, τ_{13} and τ_{23} are the shear stresses in the planes defined by S_1, S_2 and S_3. Considering a biaxial stress state and a

low penetration of the x-ray beams as it was assumed in this work, σ_{33}, τ_{13} and τ_{23} become null and the equation X becomes:

$$\varepsilon_{\Phi\Psi}{}^{\{hkl\}} = S_1{}^{\{hkl\}}Tr(\sigma) + \frac{1}{2}S_2{}^{\{hkl\}}\sigma_\Phi \sin^2 \Psi \tag{3.5.3}$$

Where $Tr(\sigma)=(\sigma_{11}+\sigma_{22})$ and $\sigma_\Phi = [\sigma_{11}\cos^2 \Phi + \sigma_{22}\sin^2 \Phi + \tau_{12}\sin2\Phi]$. This shows a linear dependence of $\varepsilon_{\Phi\Psi}$ with $\sin^2 \Psi$. The stress σ_Φ can be obtained through the slope of this linear function. An example with various measurements of $\varepsilon_{\Phi\Psi}$ fitted by a least squares method:
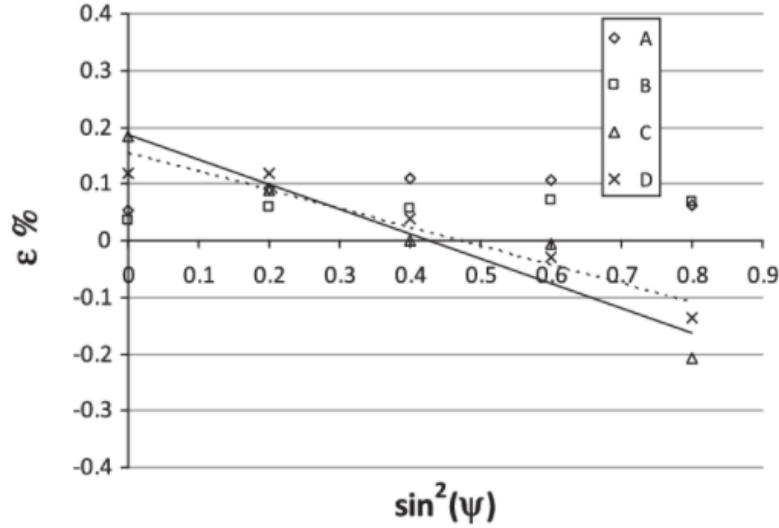
Figure 16 - Example of a linear strain $\varepsilon_{\Phi\Psi}$ over $\sin^2 \Psi$

This strain, $\varepsilon_{\Phi\Psi}$, can also be computed as a function of the lattice spacings through the following relation:

$$\varepsilon_{\Phi\Psi}{}^{hkl} = \ln\left(\frac{d_{\Phi\Psi}}{d_0}\right) = \ln\left(\frac{\sin\theta_0}{\sin\theta_{\Phi\Psi}}\right) \tag{3.5.4}$$

Where $d_{\Phi\Psi}$ is the spacing of the lattice planes from the family {hkl} in the direction defined by the angles Φ and Ψ. d_0 is the strain free lattice spacing of the same family of planes. Θ_0 is the Bragg's angle associated to d_0 and $\Theta_{\Phi\Psi}$ is the Bragg's angle associated to $d_{\Phi\Psi}$[56].

After measuring the angular change of the diffraction peak it is possible to obtain the stresses in the sample that are present in the diffraction plane through the lattice spacing of the crystalline structure. The four-main residual stress measurement techniques used in XRD is the single-angle, two-angle, $sin^2(\Psi)$ and Marion-Cohen method. They all consider plane stress at the surface of the specimen and rely on the following relation between the lattice spacing $d_{\Phi\Psi}$ and the in plane biaxial stresses [54].

$$d_{\Phi\Psi} = \left[\left(\frac{1+v}{E}\right)_{hkl}\sigma_\Phi d_0 sin^2(\Psi)\right] - \left[\left(\frac{v}{E}\right)_{hkl}d_0(\sigma_1 + \sigma_2)\right] \tag{3.5.5}$$

Fonte:[54]

Where the quantities σ_1 and σ_2 are the principal stresses, σ_Φ is the stress in the direction of the defined Φ angle and v and E are the Poisson modulus and the Young modulus of the material respectively.

The single-angle method is the least sensitive technique of the ones mentioned above because the scope of the angle Ψ is limited by the diffraction angle. Therefore, this technique is only used in very specific applications with high speed measuring equipment.

Two-angle technique as the name suggests can be used relying on the fact that two extreme values of Ψ are used considering the limitation imposed by the diffraction angle Θ (typically 0º and 45º). With this method, the stresses can be calculated using the relation:

$$\sigma_\Phi = \left(\frac{E}{1+v}\right)_{hkl} \frac{d_\Psi - d_0}{d_0} \left(\frac{1}{\sin^2(\Psi)}\right) \tag{3.5.6}$$

Fonte:[54]

Where $d_{\Phi 0}$ can be obtained through the equation 3.

The $\sin^2(\Psi)$ technique is in everything similar to the two-angle technique except the lattice spacing is calculated for various Ψ values to improve accuracy of the results. The stresses can also be computed through equation 4. There is no relevant accuracy improvement relatively to the two-angle method as long as the two Ψ angles are in the extremities of the $\sin^2(\Psi)$ range which is not always possible [54].

Marion-Cohen technique is characterized by relating the lattice spacing with the stresses in textured materials. It also assumes a biaxial stress state although the spacing has an additional dependence on a texture distribution function f(Ψ). The lattice spacing can be calculated as follows:

$$d_{\Phi\Psi} = \left(\frac{1+v}{E}\right)_{hkl} \sigma_\Phi d_0 sin^2(\Psi) + (d_{max} - d_B)f(\Psi) + d_B \tag{3.5.7}$$

Fonte:[54]

Where d_{max} and d_B are the maximum and minimum values, respectively, of the lattice spacing's range under study. When using this method, it is also necessary to calculate not only the lattice spacing but also the preferred texture of the specimen to compute f(Ψ) which can be done using multiple linear regressions [54].

The calculation method used in this dissertation was the $\sin^2(\Psi)$ method where the lattice spacing d is calculated through the diffraction angle 2Θ and the linear relation d-$\sin^2(\Psi)$ is plotted. The slope of this line is proportional to the stresses (negative slope in the case of compressive stresses).

Some limitations can be found on XRD when its applied to large welds since the x-ray beam must hit the area where the stresses will be measured and diffract to the device avoiding any obstacles between them. Also, when analysing a nanostructured material, diffraction techniques aren't useful because it is hard to find the location of the peak of diffraction. There can also be limitations when using this technique in hardened steels since some of them give very broad diffraction lines therefore, it is hard to obtain reliable values. There may also be problems when performing XRD measurements in materials that have big grain sizes, since not every diffraction domain will contribute to the diffraction line. Problems may arise when the penetration depth of the x-ray is too high because it will lead to a big offset between the irradiated volume and the surface of the specimen. It is also necessary to take special

care when analysing thin coated materials since the diffraction lines provided by the coating should be separated from the ones provided by the material itself. The elasticity XRD constants of the coating may also be thoroughly different from the substrate [56].

3.6 Summary

Since the friction welding processes are proven to be advantageous in all the fields explained in previous chapters, it is a subject of intensive investigation in the recent years with the objective of increasing the commercial applications range of this type of processes.

Friction stir welding is the most thoroughly investigated process since it is the one that can suit the biggest range of applications and has the biggest commercial value so far. The use of this process in a wide range of materials such as copper, aluminium, titanium, nickel steel and stainless-steel alloys is already broadly studied as well as the optimization of parameters for different cases. The residual stresses that remain in a component welded by this process are also well described in previous publications using different methods. There is also intensive work done on modelling that validate the experimental results obtained in the process [57],[58],[59].

Linear friction welding is also well investigated when it comes to parameters optimization for different materials and geometries [35], [37]. It was also proven to be suitable to join materials with different characteristics. The microstructural and mechanical properties changes that occur when joining components with this process is also well described in detail by previous authors [62]. Also, when it comes to modelling, some articles are published for different materials and geometries [63]– [65]. Specifically speaking about martensitic alloys and the case study of this dissertation (high strength steel chains) there are also published articles related to process optimization and modelling [1], [66], [67]. This dissertation pretends to continue the work performed in linear friction welding of high strength steel chains. The process is already optimized for this case, as well as the modelling of the flash formation. This work intends to study in detail the presence of residual stresses in this type of chains and evaluate the influence of the welding process on those stresses being an extent of the previous work done

Chapter 4 - Experimental planning and procedure

4.1 Experimental planning

In this section the experimental work plan performed in this project is described summarily using the flowchart below.

```
                    Testing axial symmetry in as
                        forged components
                              |
                              v
                           Passed
    HD (6 Samples)  <------ <> ------>  XRD 1 sample (5+5 Measurements)
                           Coherent
              incoherent      |
                              v
                    Testing axial symmetry in as
      Failed  <---  welded components with flash
                              |
                              v
                           Passed
    HD (3 Samples)  <------ <> ------>  XRD 1 sample (10+10 Measurements)
                          Coherent
              incoherent      |
                              v
                    Study the influence of LFW process
                         in the stress field
                              |
                              v
                    Testing axial symmetry in as
      Failed  <---  welded components w/o flash
                              |
                              v
                           Passed
    HD (3 Samples)  <------ <> ------>  XRD 1 sample (5+5 Measurements)
                          Coherent
              incoherent      |
                              v
                    Study the influence of the flash
                      removal in the stress field
                              |
                              v
                    Testing axial symmetry in as
      Failed  <---  welded with PWHT
                              |
                              v
                           Passed
    HD (3 Samples)  <------ <> ------>  XRD 1 sample (5+5 Measurements)
                          Coherent
              incoherent      |
                              v
                    Study the influence of PWHT in the
                         stress field
```

The steps followed in the experimental procedure give an overview of the phases of the project. The material and equipment used, as well as the methodology followed to measure residual stresses and to do the metallurgical characterization are presented on the following sections.

4.2 Material and equipment

This study was performed using a 18CrNiMo7-6 steel alloy, which is classified as a martensitic high strength steel, having Chromium (Cr), Nickel (Ni) and Molybdenum (Mo) as main alloying elements. This dissertation is directly applied to the manufacturing of steel chains. Therefore, having heat treatable alloys with high strength and tenacity is of upmost importance. This type of alloy is mostly used in components with large cross-sectional areas and permanently stressed parts for engineering applications. The material was delivered in the "as forged" half chain link form with the dimensions shown in Figure 17.
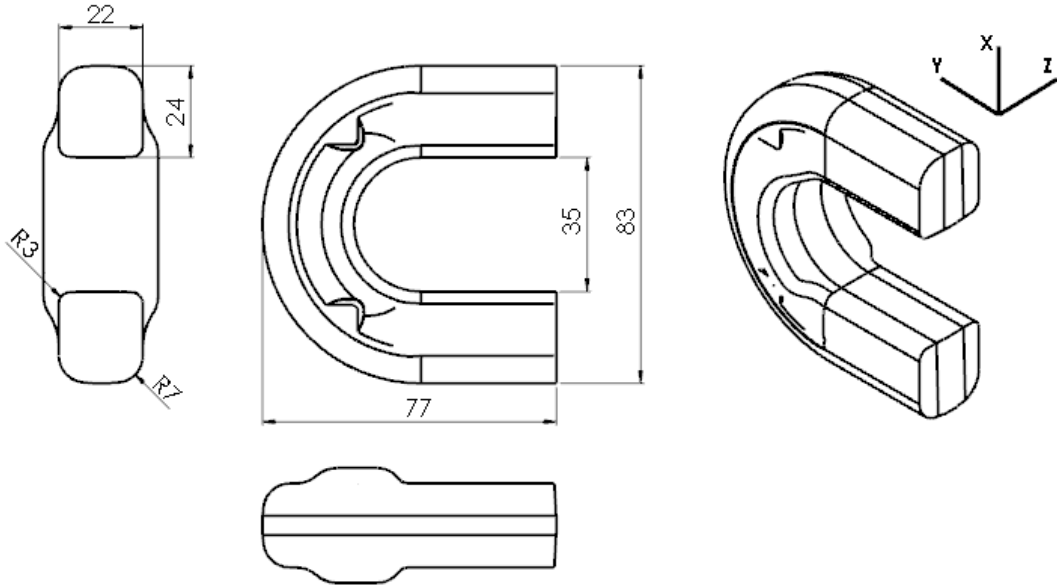

Figure 17 – Dimensions of test specimens under study

The chemical composition and mechanical properties of the material evaluated at the reference temperature (25ºC) are listed on the tables below:

C	Si	Mn	Ni	P	S	Cr	Mo
0.18	0.27	0.58	1.62	0.011	0.008	1.76	0.250

Table 4 - Chemical composition of 18CrNiMo7-6 steel (wt%)

Elasticity Modulus, GPa	200
Yield Strength, MPa	1050
Tensile Strength, MPa	1295
Elongation, %	14
Poisson Coefficient	0,3

Table 5 - Mechanical properties of 18CrNiMo7-6 steel

Pretending to evaluate the influence of the flash removing processes and the PWHT in the residual stress field, tests will be performed in specimens with different manufacturing conditions. The residual stresses will be studied in forged half chain links, as welded chain links with and without flash (using no PWHT) and without flash using PWHT. The equipment used for the HD and XRD tests performed is detailed in the next chapter.

4.3 Nomenclature/terminology

4.3.1 Conditions

Residual stress measurements throughout 4 different manufacturing stages were carried out:

- F_H - As forged chain links (where the stresses will be measured in one half link);
  - It is of extreme importance to know about the already present stress field before the welding process;
- A_H - As welded chain links (stresses will be measured in the complete link) where the formation of flash is considered;
  - To obtain information about the influence of the welding process;
- N_H - As welded chain links without flash (the same condition as before but after machining the flash out of the specimen with the standard procedure applied);
  - After laser cutting it is possible to understand the influence of flash and the removing process on the stress field.
- P_H - As welded chain links without flash, after the standard PWHT is performed;
  - Assess the influence of PWHT in the residual stress field;

The subscript "H" relates to pewag Hero chains.

4.3.2 Measurements Location

Each half chain link was subdivided in 6 different areas where it might be relevant to analyse the behaviour of the stresses. Looking from the stationary part as the origin into the moving one, the locations are defined as it follows:

- Top Left (TL)
- Top Right (TR)
- Bottom Left (BL)
- Bottom Right (BR)
- Left Side (LS)
- Right Side (RSi)

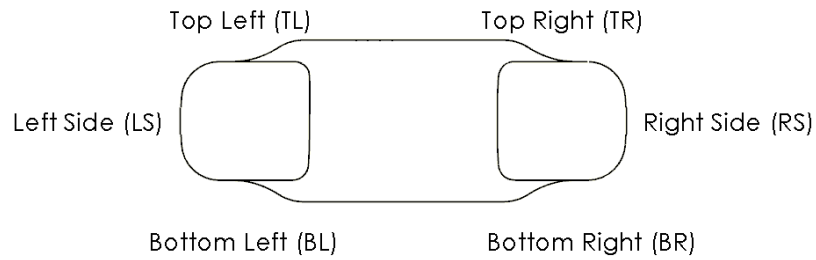The following Fig.18 explains the location of those areas:

Figure 18 - Locations where HD was performed

4.4 Hole drilling – Standards and equipment

The hole drilling method was performed using a SINT MTS 3000 system, shown in figure 6, according to the ASTM e837 standard. This system is constituted by four different components:

- An optical-mechanical drill to physically form the hole
  - This system contains a stepping motor and is powered by an air turbine that allows drilling at 350 rpm;
- An electronic controller;
- Controlling and operating software for the hole drilling;
- Reprocessing software that allows the calculation of residual stresses through the strain relieved;
  - The system allows the calculation of these stresses using four different algorithms;

The system is fully automatic during the drilling process and data acquisition. Each drilled hole has a diameter of 1,6mm and the distance between holes must be superior to 20 mm, to avoid influencing the measurement that follows. Great operator knowledge/expertise is required to apply the method correctly and obtain reliable results. The specimen should be carefully prepared and fixed, since the test deals with a precision equipment (drill).

The strain-gauge rosette used was a circular HBM RY3 like the one from the figure below. It comprises 3 grids with 0º, 90º and 135º between them. For measurements near the weld centre line (WCL), rectangular strain gages were used to overcome geometry limitations imposed by the flash.
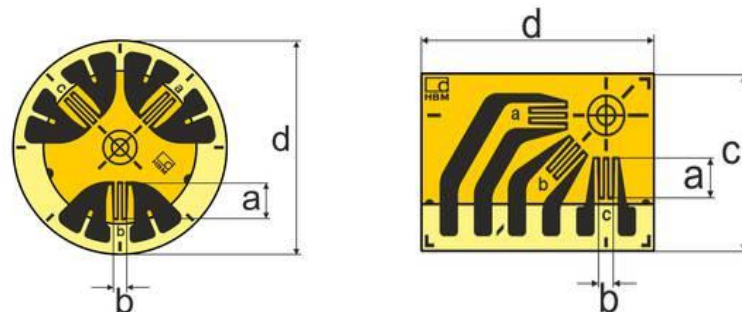

Figure 19 - Strain gauge rosettes used in the HD method

45

4.4.1 Preparation of the specimens – applying the strain gauge rosette and positioning the endmill

The steps followed to perform one measurement according to the ASTM e837 premises are listed below. It is divided in two sections: the application of the strain-gauge rosettes and the drilling procedure. The whole procedure should follow the order of implementation shown.

1. Grinding the sample with a 320-grade (46.2 µm) paper until the measurement area is completely flat;
    - If the strain gauge rosette is applied to a rough surface the reference position would not be the same in the whole rosette
2. Cleaning the grinded surface with a aceton+isopropanol solution;
    - The solution used was a HBM RMS1
3. Glue the strain-gauge rosette to the sample. Curing at ambience temperature with the pressure of a thumb;
    - The glue used was a cyanoacrylate HBM Z70
4. Apply a protection flux to each of the strain gauges in the rosette;
    - The flux used was a HBM FS01
5. Solder the data acquisition cables, using a standard soldering tool;
6. Tare balance (in the software) the strain measured in each strain-gauge to get zero strains;
    - Soldering and application of the strain-gauge itself can introduce strains that should be accounted in the measurement

The clamping of the component should be carefully thought given the geometry of the chains (similar to round geometry), to minimize vibrations and deformations induced by the driller.

The steps to position the endmill correctly are described below:

1. Using the optical microscope that is attached to the driller, align the centre of the cross with the exact centre of the rosette;
    - The drilling axis should be perpendicular to the drilled surface.
2. Advance the drilling tool until it touches the surface of the metallic foil of the rosette;
    - This task was performed manually advancing the driller in 0.1 mm intervals.
3. Drilling the centre foil of the strain-gauge until it is removed;
    - The zero-reference position for the driller is obtained.
4. Drilling the hole on the specimen;
5. Measuring the dimensions of the hole drilled and its eccentricity;
    - Using the microscope, two perpendicular diameters of the hole were measured.

The following test parameters were used in all the measurements performed:

- Maximum hole depth: 1.5mm (calculations until 1mm);
- Drilling step increment: 0,05mm;

- Number of drilling steps: 20
- Endmill diameter: 1.6mm
- Strain-gauge radius: 2,570mm

4.5 X-ray diffraction – Standards and equipment

The XRD was performed according to the EN 15305:2009 standard premises. The equipment used was a Stresstech G2 which is suitable for laboratory, factory or field use due to its portability, and can easily be assembled by one person alone. The main advantages are having the possibility to perform measurements in confined spaces and in complex geometries. The measurements were performed at Material Center Leoben Forschungs GmbH (MCL). This specific model has the following technical specifications provided by the manufacturer [68]:

G2 Goniometer

- Two symmetrically positioned MOS position sensitive detectors;
- Angular resolution of 0.03°–0.06°/pixel 2θ-angle;
- 2θ-range of the detectors is continuously adjustable within +100° to 165°.
- Possibility of usage of Cr, Cu, Co, Fe, V, Ti, Mn tubes. Cr-tube provided as a standard was the one used in this project.
- Replaceable collimator, to provide 1, 2, 3, 4 and 5 mm spot sizes. Special collimators available as an option; The one used in this dissertation was the 1mm.
- Measurement distance of 50mm;

X3000 main unit

- X-ray power supply 5–30 kV/0–10 mA freely adjustable within limits;
- High voltage generator;
- Self-contained liquid cooling system;
- Includes all interlocks required for complete safety;
- Universal power input;

The software used to analyse the results obtained was the Stresstech Xtronic with the following features:

- A Microsoft Windows-compatible application with a powerful performance level.
- One program for the user interface including measurement setup, data analysis and machine control;
- Simple Ethernet connection for control through PC;
- Provides user-friendly, menu-driven operations;
- d-sin²ψ measurement mode;

- Ω-measurement mode;
- Retained austenite measurement mode;
- Mapping capabilities for automatic measurements;
- Multiple exposure d-sin²Ψ and Ω-modes; peak shift calculation by cross-correlation and several other methods;

The following figure illustrates clearly the device and respective collimator used in the measurements of this project as well as the power supply and the placement of the samples.

Figure 20 - X-ray diffraction equipment used

4.6 Metallurgical and mechanical characterization

The metallurgical characterization was carried out firstly by cutting the welded samples as carefully as possible to avoid microstructural modification. The cutting machine used was a Struers Labotom 5. The selected samples were then embedded in a Struers CitoPress 20 machine with Multifast Black resin, grinded using a wet Silicon Carbide paper in 7 steps with ISO grit varying from 80 to 2000 (Average grain size from 201µm to 10.3µm) in a Struers Tegramin-30 machine and polished in the same machine in 2 steps with solution DiaPro 3µm and 1µm. All samples were cleaned with ethanol and chemically etched with Beraha I solution. Different etchants were experimented such as Nital 3% and LePera. A Zeiss microscope with polarized light was used in the analysis. The grain size was also measured recurring to the Hilliard single circle procedure, according to the standard ASTM E112 [66]. This method accounts for the grain boundary intersections with the circular path. This circle should never be smaller than the largest observed grain and Hilliard recommends at least 35 intersections per circle. The microhardness profile was made in a EMCO Duravision G5 machine.

Chapter 5 - Results and discussion

5.1 Hole Drilling results

The method provides the principal residual stress values and the orientation angle for each incremental step. Gathering the maximum and minimum stresses with the Mohr circle, it is possible to calculate the stresses in the direction of the WCL defined as σ_x and transversely to it σ_y. To perform these calculations, it is necessary to define the orientation of the strain gages a and c (Figure 19) relatively to the weld centre line.

5.1.1 As forged initial condition (F)

To have a starting condition to evaluate the effects of the welding procedure in the RS field, there were performed measurements in the "As forged" initial condition. Thus, the difference after welding can be measured close to the WCL and far away from it. To that end, three measurements were considered and are depicted in Figure 21 and in Figure 22 below.

When calculating the stresses in the x direction (Figure 22 a)), it is seen that the maximum compressive stress occurs in **LS** at a depth of around 0,1mm. The biggest difference in the stress values occurs closely to the surface (nearly 200 MPa between **TL** 23 mm and **LS** 23 mm) at around 0,2 mm depth from it. When progressing into higher depths, this difference starts to decrease reaching values of less than 50 MPa. The maximum absolute values for the locations **TL** 23 mm, **TL** 3 mm and **LS** 23 mm are -380 MPa, -530 MPa and -550 MPa respectively.

In the y direction (Figure 22 b)), the maximum absolute values of the stresses also occur close to the surface of the specimen (0,1 mm depth). This difference is observed when comparing the same locations referred before, although the maximum discrepancy only reaches 100 MPa instead of the 200 MPa referred in x. Again, when measuring the stresses at higher depths, the differences between each location tend to diminish (around 50 MPa). The maximum values for the locations **TL** 23 mm, **TL** 3 mm and **LS** 23 mm are -350 MPa, -410 MPa and -350 MPa respectively.

Typically, in the HD method, differences of around 100 MPa can be neglectable due to measurement errors such as: not gluing the strain gage in the exact same position (with a different angle between the WCL) will vary the results; Not drilling the strain gage foil properly can also cause errors in the values near the surface of the specimen. If the surface is not completely grinded or contains impurities the values will also differ. Therefore, it is considered that the stress values in all the conditions at depths higher than 0,2 mm are the same.

Having the maximum values of RS close to the surface, as in the curves obtained for the **F** condition, show a typical behaviour of a shot peened surface where the maximum value of the compressive stresses is strongly dependant on the shot peening conditions used. Therefore, further measurements were not performed in the previously planned locations since the stress state can be considered the same in the whole half chain. The RS results obtained are in good agreement with the existing literature for shot-peened specimens, in which the maximum absolute stress value remains close to the surface of the component and tend to zero when increasing the depth. The differences in the results close to

the surface might also be explained by the non-uniformity of the shot peening conditions. As an example, considering the groove present in the **LS** of the sample, if the same shot peening pressure was applied in the whole surface of the chain link, the stress absolute value can also differ when the surface's geometry changes.

Shot-peening is a surface treatment that imparts strong residual compressive stresses at a shallow depth of an engineering component. These compressive stresses are beneficial to the fatigue life and the resistance to stress corrosion cracking of a component. Which is very important to the chain application studied in this project [69]. The results shown in the graphs below can be explained by the positive values of plastic deformation caused by the treatment's peen. The dependency of the stresses in the positive plastic deformation values are illustrated in the following Figure 23. This issue was explained by *Torres et. Al.* [70]*,* where he studied the influence of shot peening conditions in the fatigue life of the component. He stated that the depth of the compressive stress state greatly depends on the shot-peening intensity.
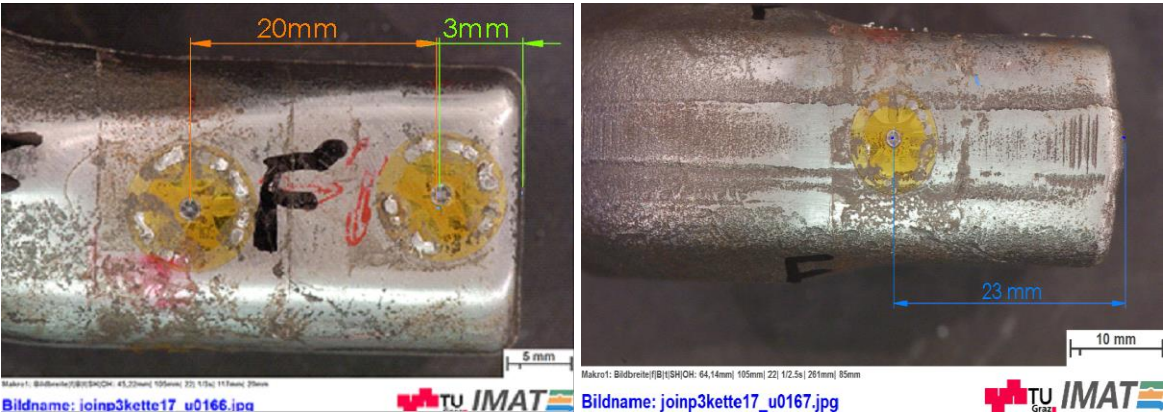
Figure 21 - Location of the measurements (**F** condition)

b)   a)
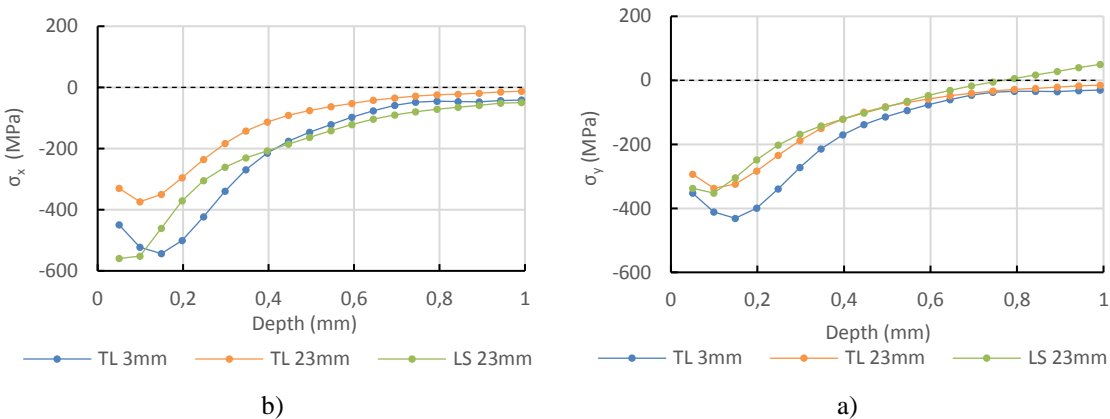
Figure 22 – Residual stress results parallel and transverse to the WCL for three different locations (as forged condition).
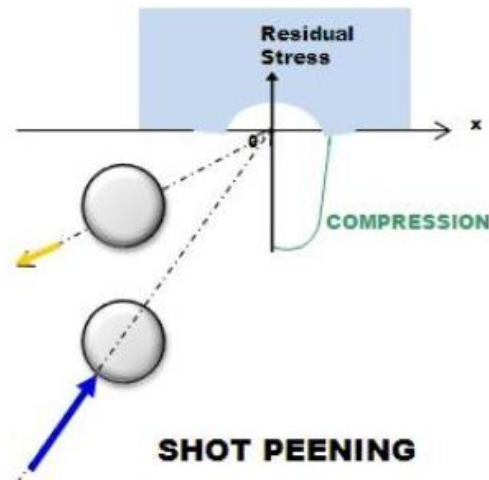
Figure 23 - Illustration of the peening influence in the residual stress values of a component

5.1.2   As welded with flash condition (A)

5.1.2.1   *Comparison between F and A*

In this section it will be evaluated the influence of the welding process in the RS field of the chain links. Therefore, there were carried measurements following the same procedure as before in the as welded samples at the same distances from the WCL. The following Figure 25 shows the comparison of the residual stress profile 3mm away from the WCL in the **F** and **A** conditions.

These measurements (see Figure 24) showed a clear tendency of relaxation of the compressive residual stresses caused by the shot peening. When comparing the stress field near the surface of both conditions, σ_x (Figure 25 a)) decreases from a maximum absolute value of around -400 MPa to -100 MPa. This value increases to a maximum of around 250 MPa when the depth of the hole is increased. This switch from compressive to tensile can be explained by the regions affected by the heating cycle during the friction phase of the welding process as well as by the axial shortening when joining both half chain links. The interface of the chain link is the region that takes longer to cool down. Thus, regions close to it (HAZ included) will be subjected to tensile residual stresses to oppose the compressive stresses due to the thermal cycle. The welding process has a critical effect on the RS state. By comparison of the residual stress field in regions far away from the heat affected zone (HAZ) for both conditions, significant differences were not observed.

There is neglectable difference in the stresses in a transverse direction to the WCL (σ_y, see Figure 25 b)) since the only force applied in this direction during the joining procedure is the forging force. In this direction the biggest difference only occurs close to the surface of the specimen (0,1 mm). This 200 MPa difference at the surface might be explained due to the measuring errors mentioned before (not drilling the centre of the strain gage properly), or by the variations in the temperature gradient at the surface of the chain after shot peening was applied. Besides this difference, both conditions tend to have the same values of the residual stress field after 0,3 mm were drilled without switching to tensile along the whole depth of the hole. This result is in great agreement with the investigation provided by Romero et al. [17], in a LFW joint of a titanium alloy and concluded that increasing greatly the forging

pressure doesn't cause any difference in the stresses in this direction. Thus, the effect that remains predominant in the RS state in this direction seems to be the shot peening one.

On the other hand, far away from the WCL, there is only a slight variation of the stress field in both the x and y directions. Figure 26 a) and b)) illustrates the location where the measurements were performed for each condition (**F** and **A**).

When comparing σ_x (see Figure 27 a)) for both conditions, there is a variation of 100 MPa after 0,2 mm depth. As explained before this is a typical difference to be found in HD measurements that can be neglected.

In the y direction (Figure 27 b)), the stress values are almost the same except for the initial steps of the HD (until 0,1 mm) and exactly at 0,4 mm depth. Although this difference never exceeds 100 MPa. Thus, the RS field in both directions can be considered the same for the **F** and **A** conditions in this position of the chain link.

This stress change in the x direction close to the WCL was observed by Smith *et Al.* [71] in the study of the RS field in LFW Inconel 718 where it was observed an increase of almost 300 MPa when comparing the stress values of the WCL with the BM. Also Xie *et al.* [72], when investigating the residual stress field in dissimilar titanium LFW joints. The authors concluded that the highest tensile stress values occurred close to the WCL where the material is subjected to extreme plastic deformation and temperature gradients.

Far away from the weld centre line, both the transverse and parallel residual stresses show a variation of less than 100 MPa. It was confirmed that 23 mm away from the WCL, the RS field does not change since it is far away from the HAZ. In this region the material is not affected neither by the thermic nor the plastic deformation cycles. Therefore, no significant differences were observed even after the welding procedure.
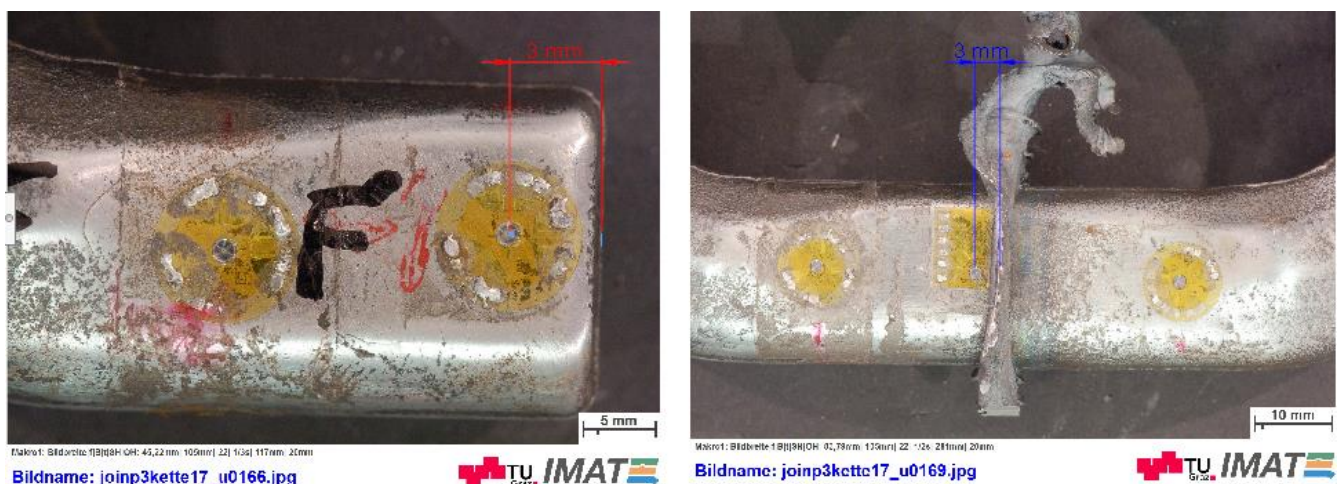

Figure 24 - Location of the measurements a) **F**, b) **A** condition (3mm away from WCL)
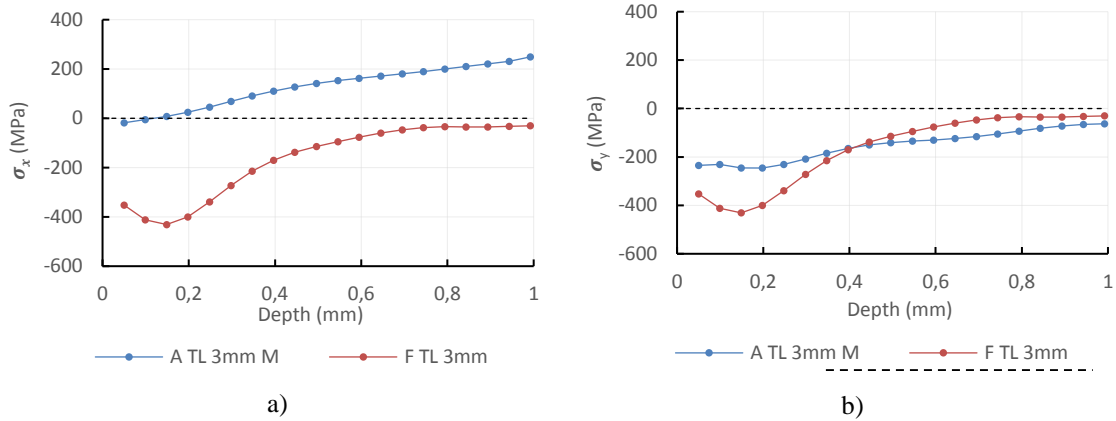
Figure 25 - Comparison between a) σ_x and b) σ_y for both the as forged and as welded conditions 3mm from the WCL
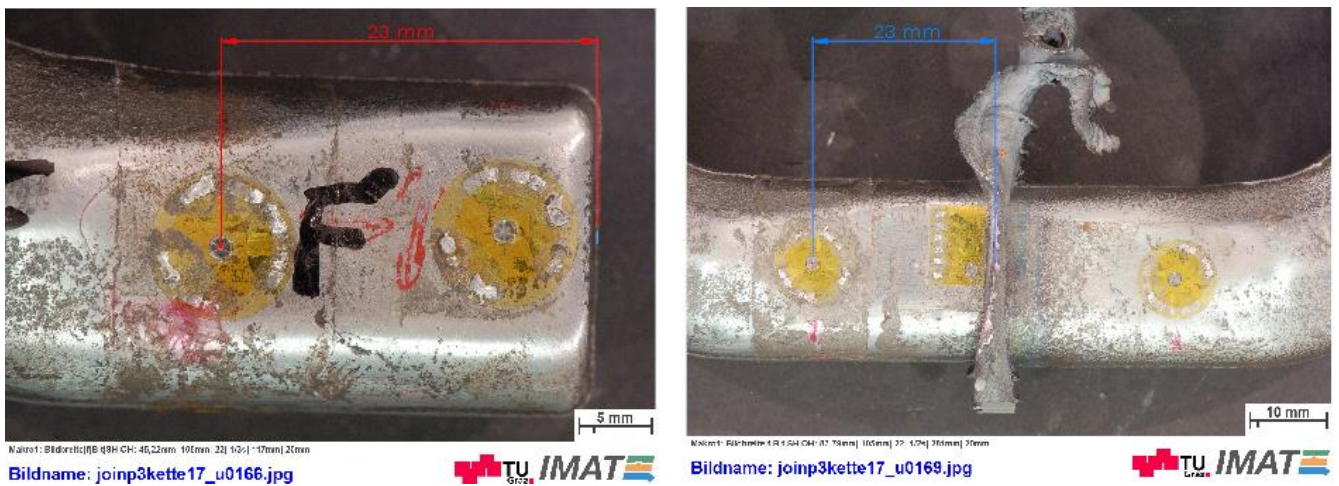

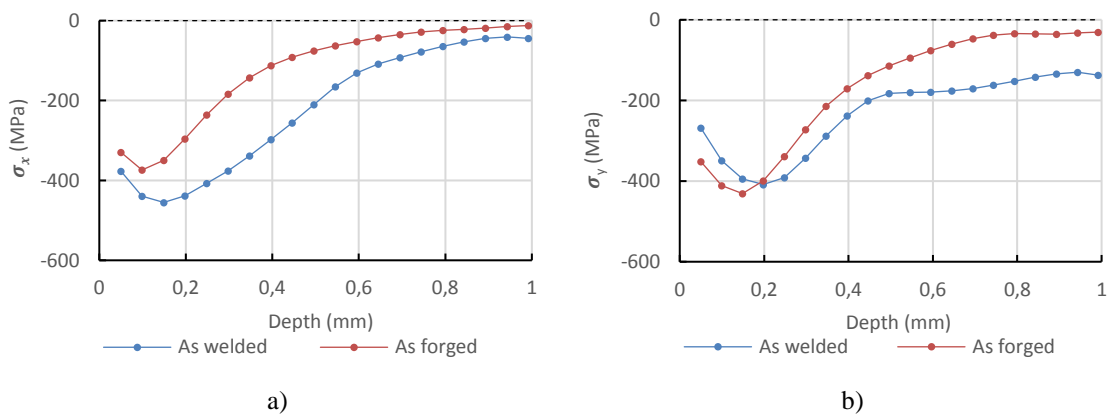Figure 26 - Location of the measurements a) **F**, b) **A** condition (23mm away from WCL)

Figure 27 - Comparison between a) σ_x and b) σ_y for both the as forged and as welded conditions 23mm from the WCL

5.1.2.2 *Symmetry of the process*

In the as welded with flash condition, there were performed measurements at the exact same distance of the weld centre line (3mm) in both the stationary and moving parts of the chain link so the symmetry of the RS field could be evaluated.

The results shown in the Figure 29 a) below, show that σ_x has higher absolute values in the moving part than in the stationary one. In both half chain links, it can be seen the switching from compressive stresses into tensile as stated before. The maximum compressive stresses in the moving part (around 100 MPa) occur nearly at 0,2 mm depth of the hole, while in the stationary they are already tensile at that depth. This difference starts decreasing and at 0,4 mm depth it is almost neglectable. The higher compressive stresses in the moving part close to the surface, might be explained by differences in the clamping system. The differences might also be explained by other uncontrolled factors since the RS field comprises the whole thermomechanical history of the component after forging. This clamping system differs from the moving to the stationary. The moving clamp is more susceptible to wear. This wear can cause clearance between the chain link which will make the half chain link oscillate unexpectedly. Therefore, the forces exerted on this part of the chain might be bigger than the ones exerted on the stationary one. This can explain the increased values of the compressive stresses only at the surface in the x direction.

In the y direction the difference is always lower than 100 MPa. This difference can be neglected as mentioned before although it starts tending to 0 MPa at higher depths than 0,4 mm. Again, the only force exerted in this direction during the joining process is the forging force which can explain the fact that the RS field in this direction is nearly the same. In both parts of the chain link the stress values remain compressive.

To evaluate the symmetry of the residual stress field between the Top/Bottom locations and Left/Right areas of the chain link, measurements were performed at an exact same distance of the WCL as illustrated in Figure 30 and Figure 32. The results are shown in Figure 31 and Figure 33.

When analysing Figure 31 a) it can be observed that the RS field is almost exactly the same for both the Top and Bottom regions of the chain link along the whole depth of the hole. As mentioned before, the stresses switch from compressive 50 MPa to tensile 250 MPa in this region due to the welding process.

Regarding the stresses in y direction (Figure 31 b)), there is a constant difference of around 50 MPa. For the reasons addressed previously this difference can be neglected. As discussed before, the stresses remain compressive during all the drilling steps, tending to 0 MPa as the depth is increased.

Besides the variation of the stress values (higher than 100 MPa) in the first 0,4 mm of the hole depth in the comparison of the **M** and **S** parts, the obtained results permit to conclude that LFW induces a symmetric RS field in the chain link. As mentioned before, this difference might be explained by the wear of the clamping system that increase the forces exerted in the **M** component in the direction of oscillation during the joining process.
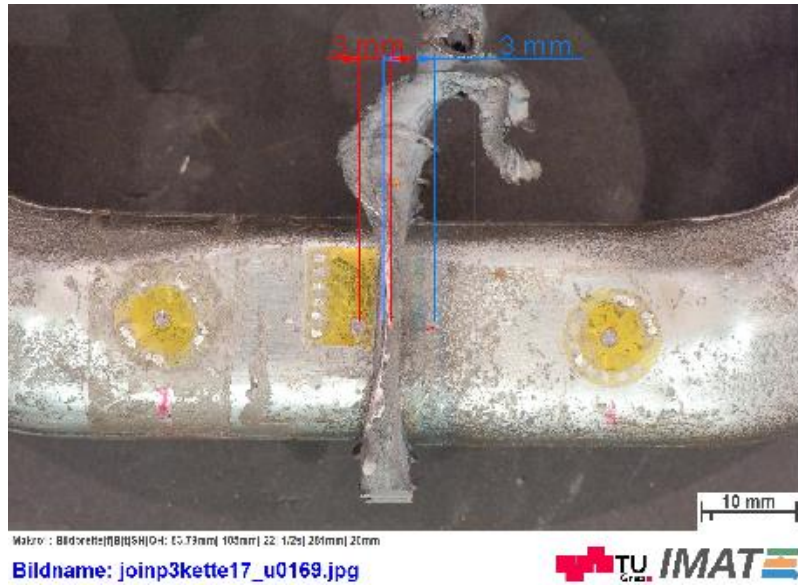
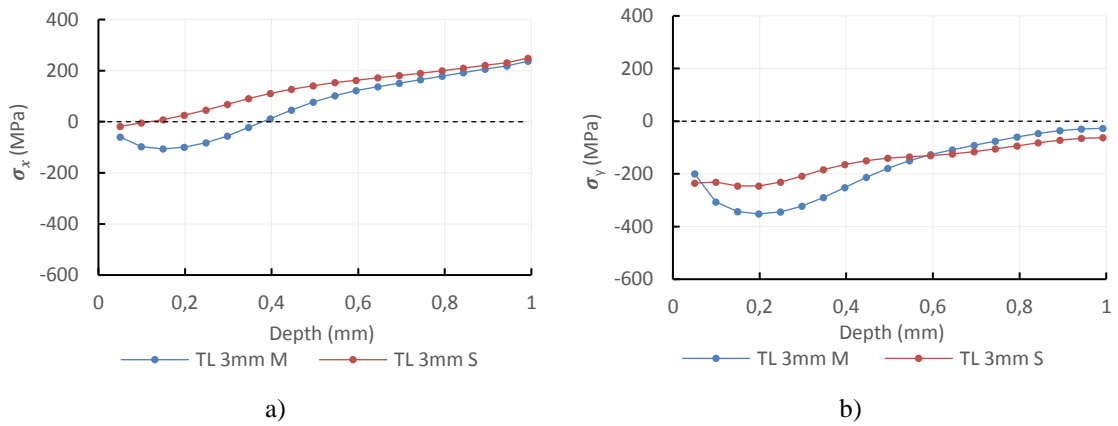Figure 28 - Location of the measurements (**A** condition **TL** location) moving/stationary.

a)

b)

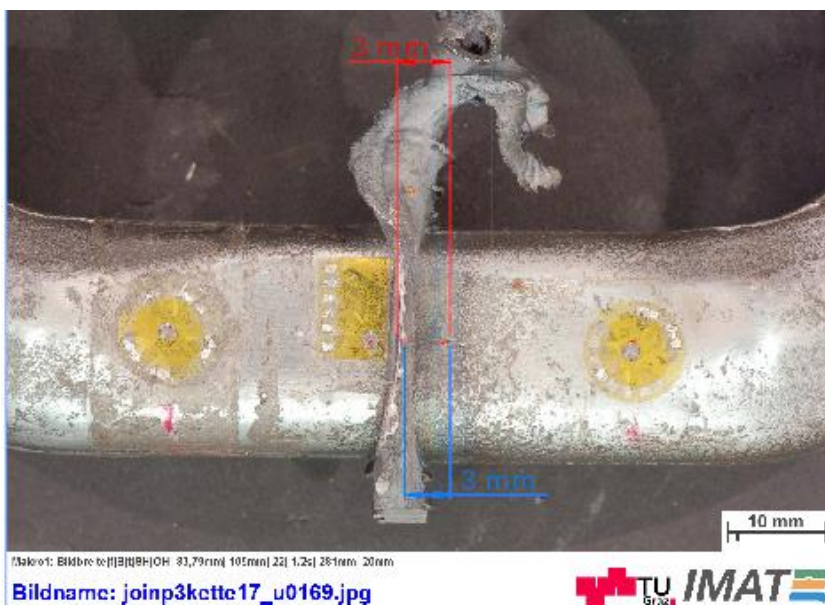Figure 29 – Comparison between a) σ_x and b) σ_y in both the stationary and moving side 3 mm away from the WCL

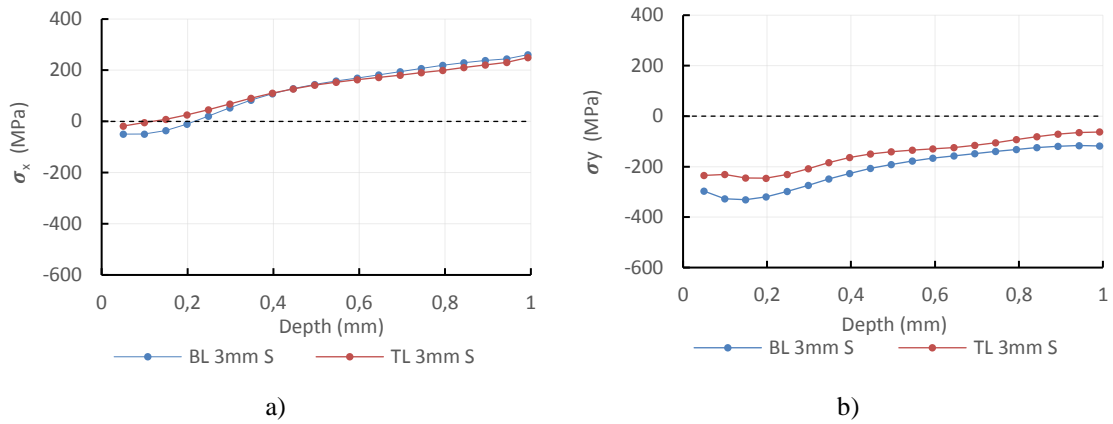Figure 30 - Location of the measurements (**A** condition **TL** and **BL** location).

Figure 31 - Comparison between a) σ_x and b) σ_y in both the TL and BL locations 3mm away from the WCL.
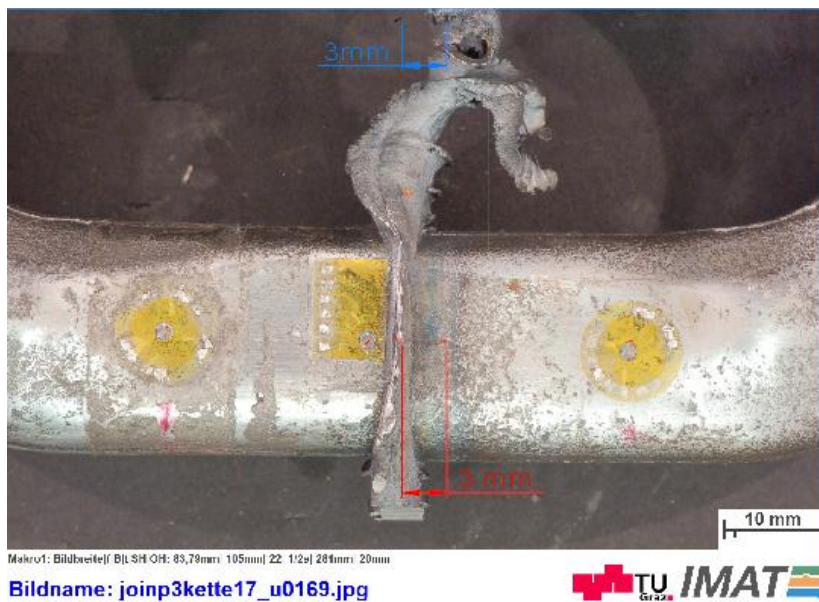
Figure 32 - Location of the measurements (**A** condition **TL** and **TR** location) moving/stationary.
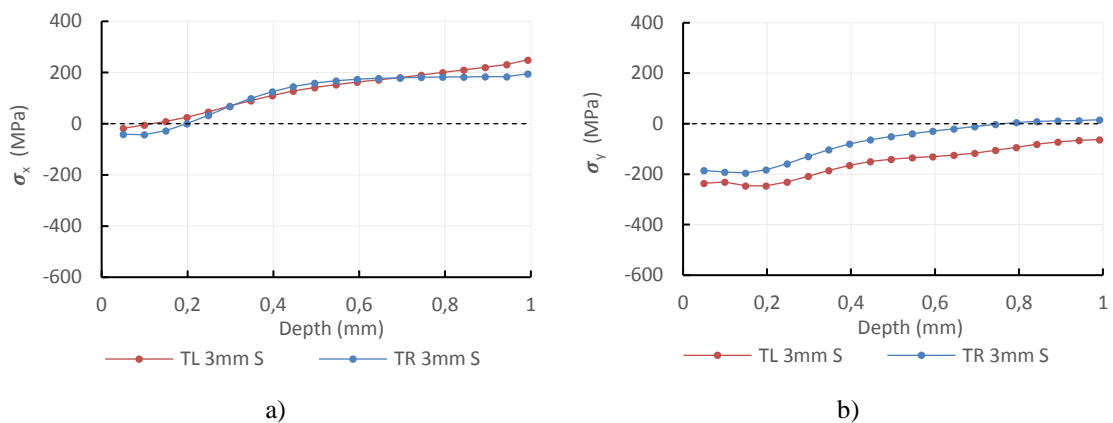
Figure 33 - Comparison between σ_x and σ_y in both the TL and TR locations 3mm away from the WCL.

5.1.2.3 *Comparison between HAZ and BM*

In this section it is presented an overall comparison between the RS field in the BM for both moving and stationary parts of the component. In Figure 33 and Figure 36 the location of the measurements is

56

illustrated.

In the x direction it is seen that the BM has almost the same RS profile in both the **M** and **S** parts of the component (see Figure 35 a). Besides the 200 MPa difference that starts to decrease nearly at 0,2 mm depth from the surface of the chain link, the RS field is almost the same at 0,5 mm depth. From that point onwards, the difference obtained was always below 50 MPa which can be neglected as referred before. Inside the boundaries of the HAZ, the **M** part tends to have a higher compressive value of the RS field until 0,5 mm depth. This was not verified in the **LS** measurement since the point **LS** 3mm **M** was performed without respecting the minimum distance between holes. Therefore, this point was neglected in the analysis. This is seen to be a great motivation for the company to study the clamping system in detail. Considering the high pressures exerted during the friction phase of the LFW process, it is valid to assume that the forces exerted by each part of the clamping tool at the surface of the chain link are different.

When analysing the RS field regarding the y direction on the **BM** (see Figure 35 b and Figure 37 b)), there are observed stress variations around 100 MPa after 0,6 mm of the hole was drilled. This means that in this direction at this depth, it can be assumed the RS field in both **TL** and **LS** regions is nearly the same. When comparing the HAZ of both sides in both regions, the stress field does not seem to be influenced by the LFW process at the same depth mentioned before.

The predominant effect on the RS field in the **BM** is the one induced by the shot peening. Although at lower depths, there seems to be an influence of the wear in the clamping system. The stress values increase in regions where the material was subjected to higher thermal or plastic deformation cycles.
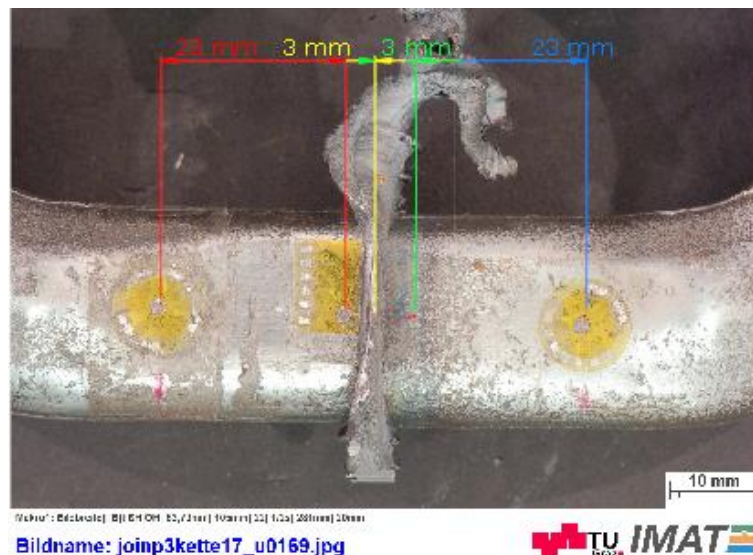

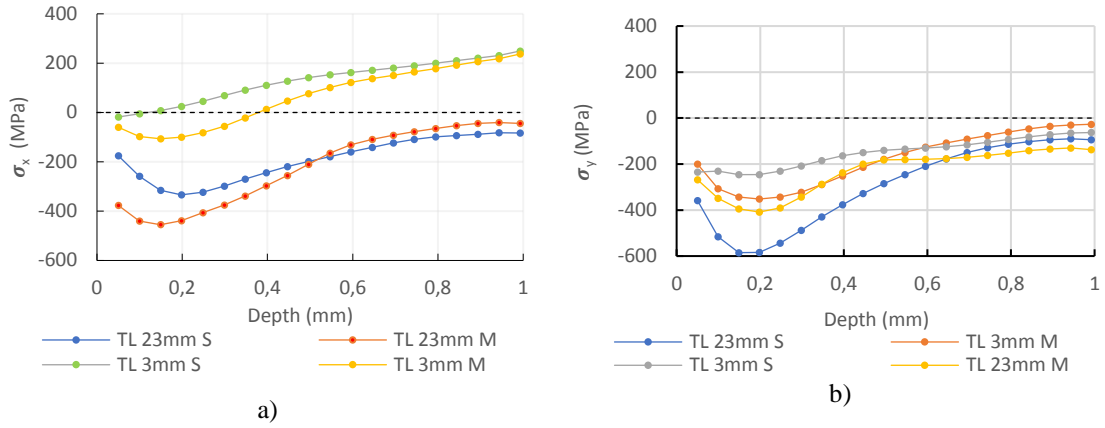Figure 34 - Location of the measurements (**A** condition **TL** location)

Figure 35 – Comparison between a) σ_x and b) σ_y **TL** location (A condition).
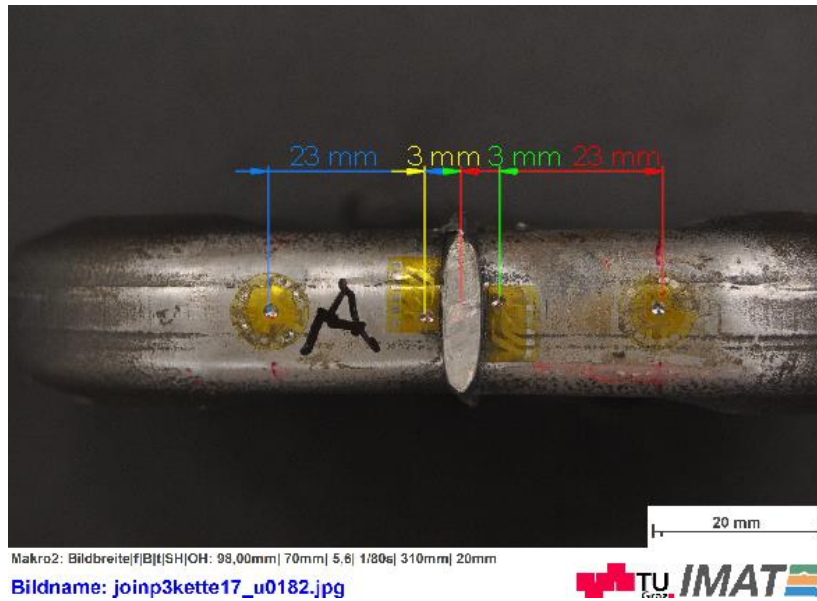
Figure 36 - Location of the measurements (**A** condition **LS** location)
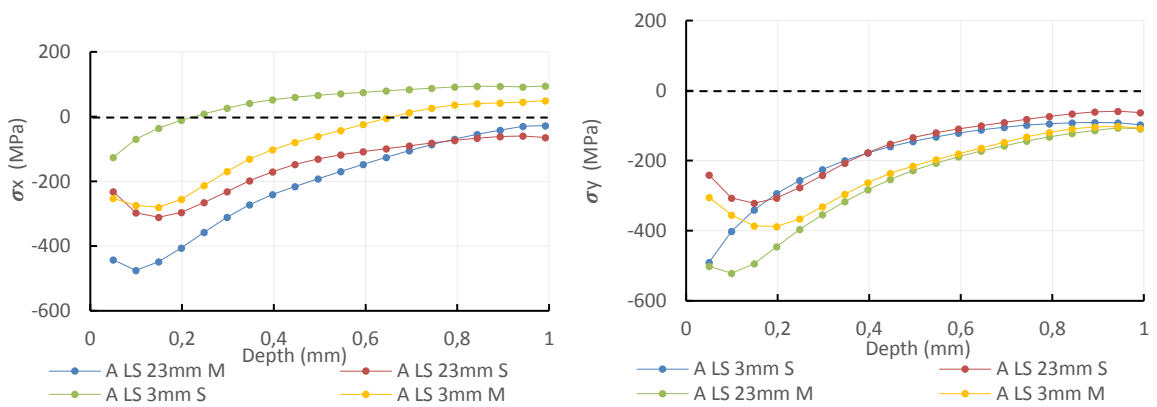
Figure 37 - Comparison between a) σ_x and b) σ_y in the **LS** location (A condition).

5.1.3 As welded without flash condition (N)

The flash removal from the samples was carried out by laser aided machining. In this section, there is discussed the influence of the flash cutting in the RS fields. The results are shown below being

compared to the previously obtained ones for the **A** condition. The location of the measurements is illustrated in Figure 38 and Figure 40. The measurements in **M** and **S** parts 3mm away from the WCL were always done in different samples due to the minimum 20mm distance recommended by the ASTM standard. In the **A** condition 23mm away from the WCL in the **M** part this requirement was not fulfilled. This might explain the compressive stress results in this point. The results obtained for the y direction show that the stresses in the y direction never switch to tensile as it was observed in previous conditions.

In the **TL** region of the chain there seems to be almost no influence of the residual stress field in both x and y directions Figure 39 a) and b). Due to the geometry of the surface, it was only possible to perform HD measurements 3 mm away from the WCL. Although theoretically the removal of the flash would cause differences in the RS field in order to maintain equilibrium, those differences would only occur in the exact location of the WCL where the RS were not measured. Therefore, it can be stated that independently of the direction (x or y), there are no significant differences derived from the flash removal

In the **LS** location it was observed the same behaviour besides the difference of the moving part of the **N** condition at 0,6 mm depth. This might be explained due to the groove present in the **LS** of the specimen. In some samples it was impossible to grind that grove away from the chain, since the grinding was performed manually to avoid the introduction of RS in the component. Again, 3 mm away from the WCL in the **M** part there seem to be an abnormal increase in compressive stress values.
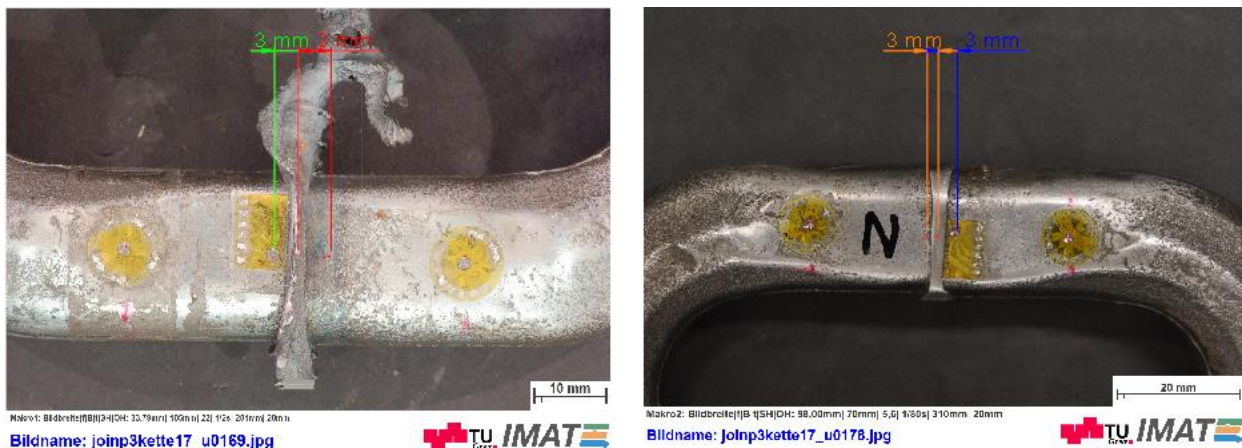

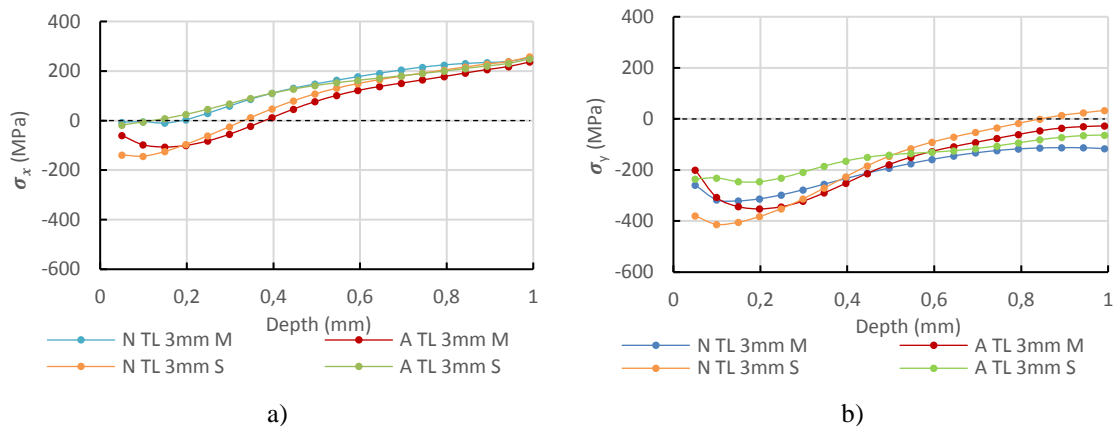Figure 38 - Location of the measurements a)**A** and b)**N** conditions **TL** location

a)   b)

Figure 39 - Comparison between a) σ_x and b) σ_y in the **TL** location (A and N conditions).
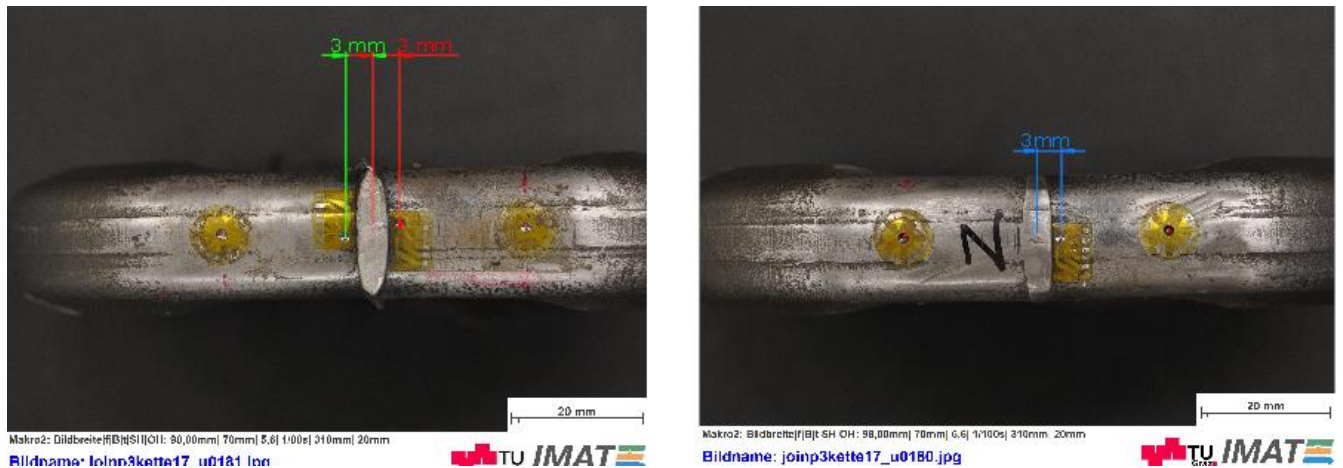
Figure 40 - Location of the measurements a) **A** and b)**N** conditions **LS** location
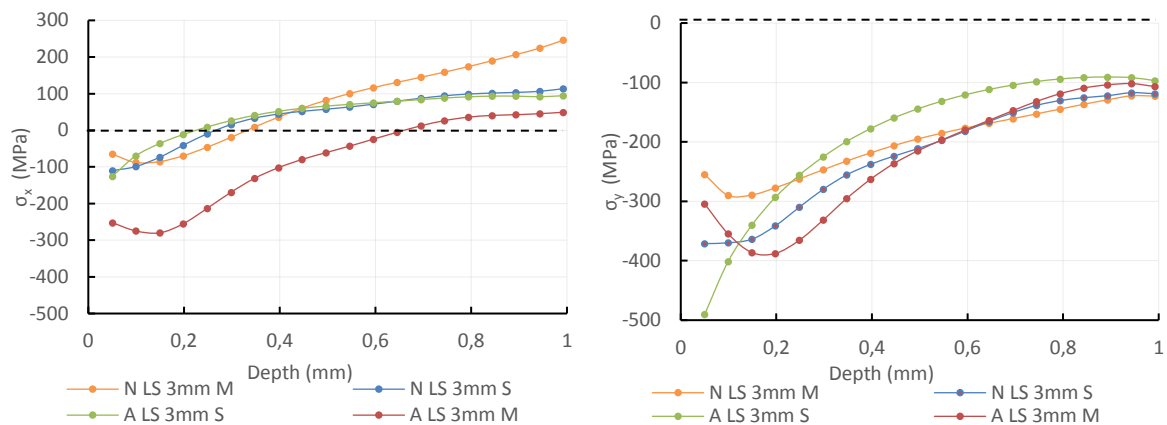
Figure 41 - Comparison between a) σ_x and b) σ_y in the **LS** location (A and N conditions).

5.1.4 Post Weld Heat Treated (P)

5.1.4.1 *PWHT condition results*

The last manufacturing step performed by the company is the PWHT. The PWHT consisted in three different phases: heating up in a salt bath at approximately 40 ºC/min; quenching at 130 ºC/min and annealing in a furnace at approximately 5 ºC /min. These cooling rates are illustrated in the following Figure 42. The RS values for the **P** condition are shown in the following Figure 44 and Figure 46. Since it was concluded that the flash cutting does not influence the RS field in the measured locations, the results from the **P** condition are compared with the ones obtained in the **A** one. The illustration of the locations where the measurements were performed are shown in Figure 43 and Figure 45.

As it can be seen from the figures below, the residual stress values of the **P** condition are nearly the same in every location in both x and y directions. The results only showed a minimal change of 100 MPa between the **TL** and **LS** locations that can be explained by the present groove in **LS**.

Jang et. Al. [73] studied the influence of the stress relieving annealing in A335 P12 steel welds. The authors concluded that the annealing clearly decreases the amplitude of variation of the RS field. Even

in regions affected by the weld thermomechanical cycles. This result is shown in the following Figure 48 for the **TL** location and it is also verified in the **LS** region in Figure 52. The switch from tensile to compressive stresses is clearly happening due to the PWHT performed.
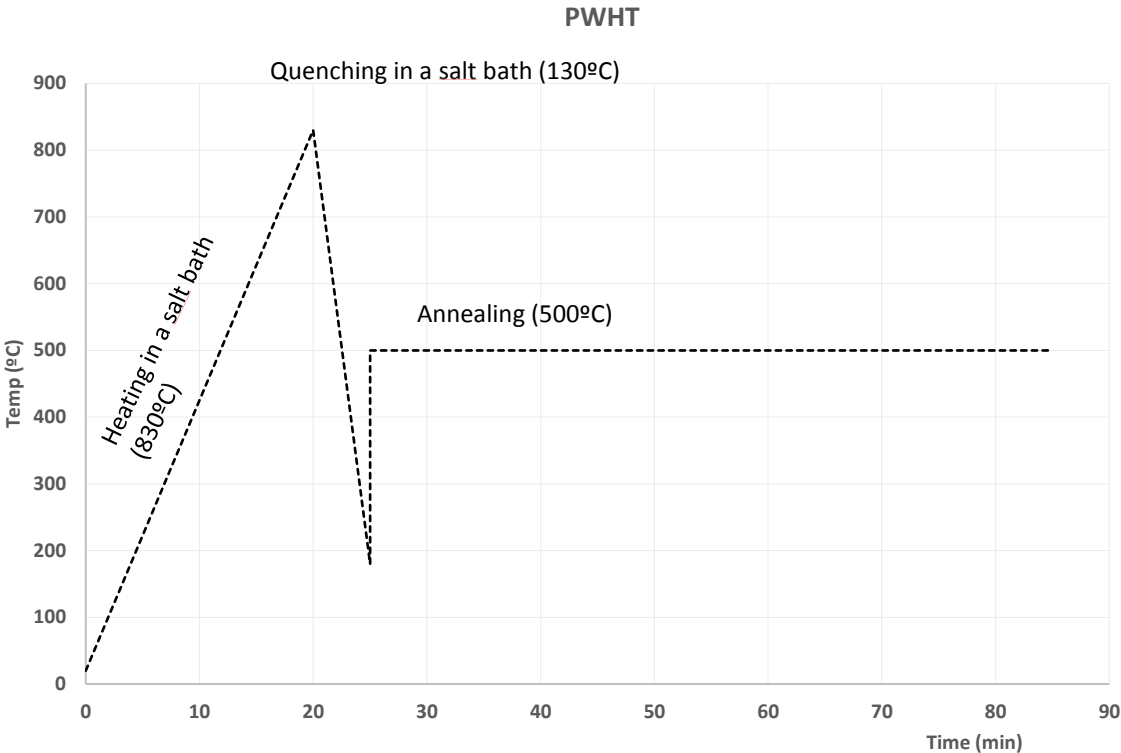
PWHT

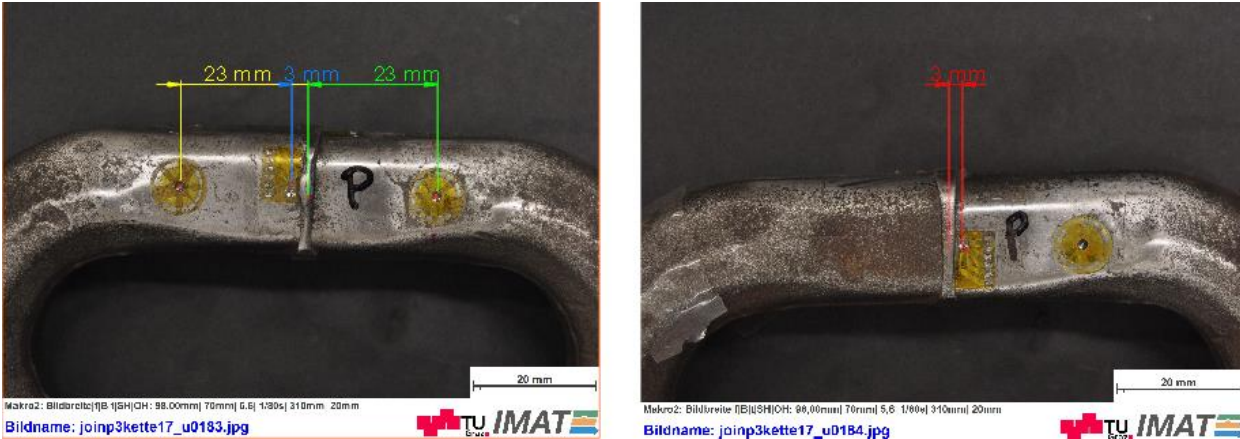Figure 42 - Illustration of the cooling rates achieved in the PWHT steps.

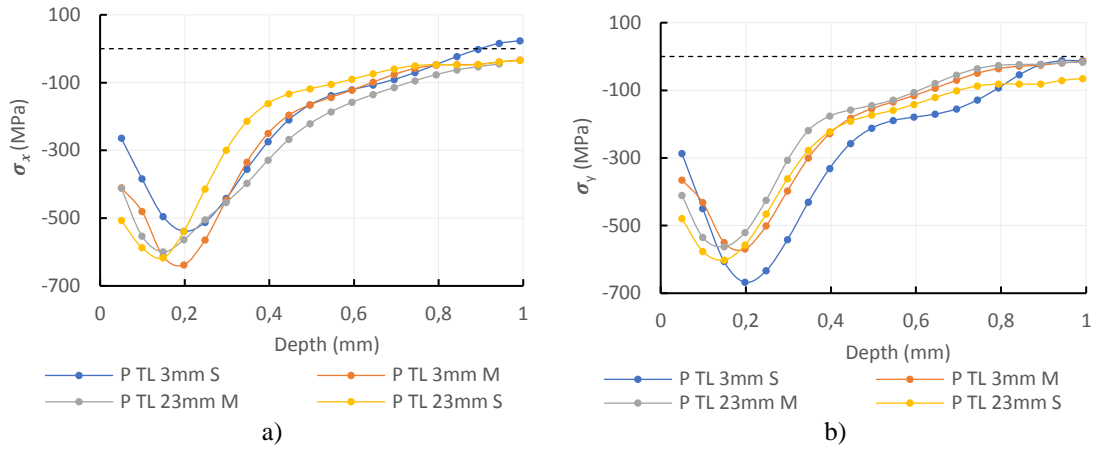Figure 43 - Location of the measurements (**P** conditions **TL** location)

Figure 44 - Comparison between a) σ$_x$ and b) σ$_y$ in the **TL** location (**P** condition)
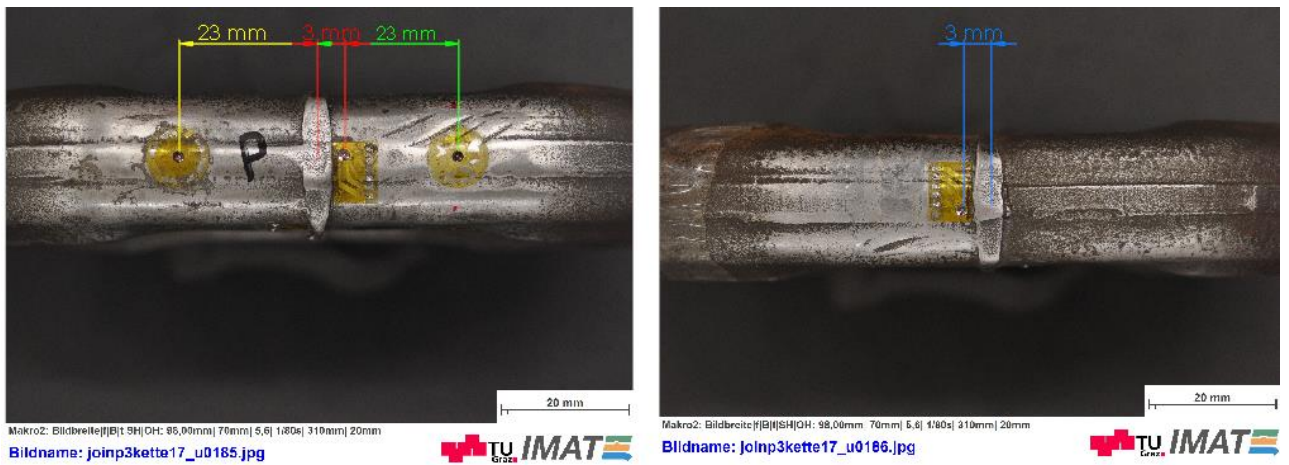

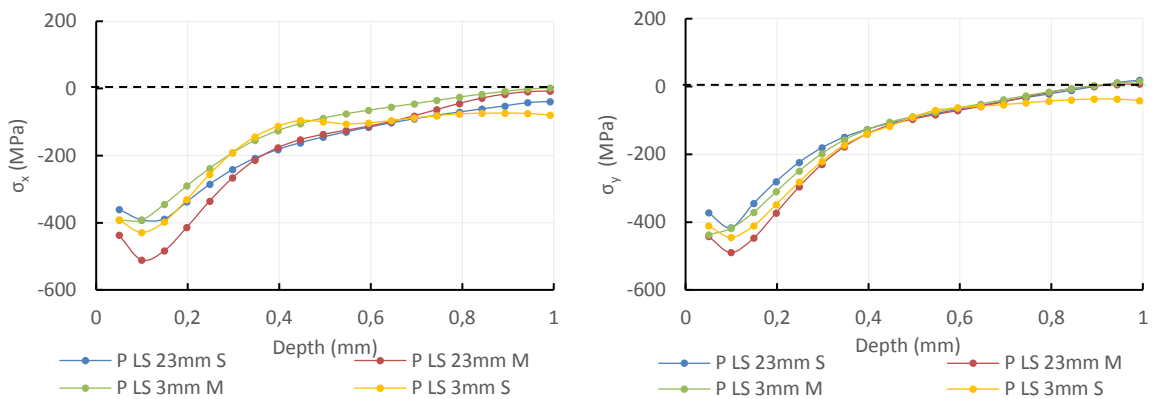Figure 45 - Location of the measurements (**P** condition **LS** location)

Figure 46 - Comparison between a) σ$_x$ and b) σ$_y$ in the **LS** location (**P** condition).

5.1.4.2 *Comparison between A and P*

To understand the influence on the RS field caused by the PWHT, there was made a direct comparison between the results obtained for **A** and **P**. These results are depicted in Figure 48, Figure 50, Figure 52.

The maximum effect of the PWHT can be observed when comparing the stationary part of the **A**

condition with the moving part of the **P** condition. These two conditions show a difference of approximately 600 MPa at 0,2 mm depth. Although this value is around 50% of the yield strength of the material, there were obtained compressive stresses. As it was mentioned before, compressive residual stresses increase the fatigue life and the stress corrosion cracking resistance of the component. Therefore, it is reasonable to assume that the RS state of the final manufacturing **P** condition has acceptable values. It can also be observed that the stress field after PWHT has approximately the same values either in the x or y direction. This result is also in agreement with the investigations mentioned below. The RS values show that the annealing with the heating rate used influences mostly the regions near the surface of the specimens.

There is a uniformization of the stress field along the whole surface of the chain link. This result is in accordance with previous literature on this topic. *Zeng et. Al.* [74] investigated the annealing effect in the RS distribution of CdZnTe wafers and showed that this heat treatment is able to reduce high tensile stresses into compressive ones. This discovery was also corroborated by *Preuss et Al.* [75] where the author compared residual stresses of "as welded samples" with specimens that were subjected to different PWHT conditions in IMI 550 LFW joints. He concluded that the annealing could even relieve hydrostatic residual stresses. The author also concluded increasing the annealing temperature would cause a bigger stress relief.
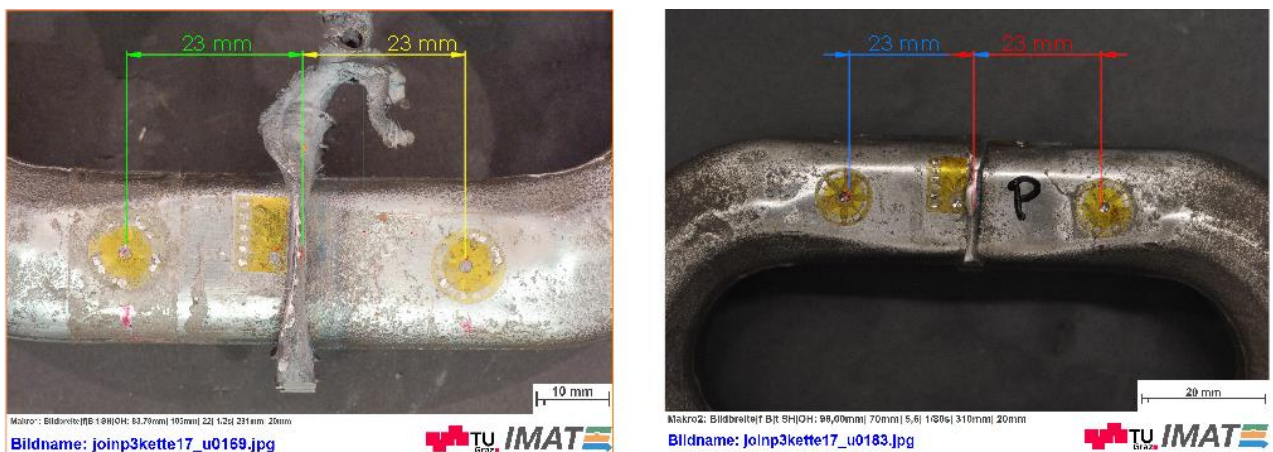

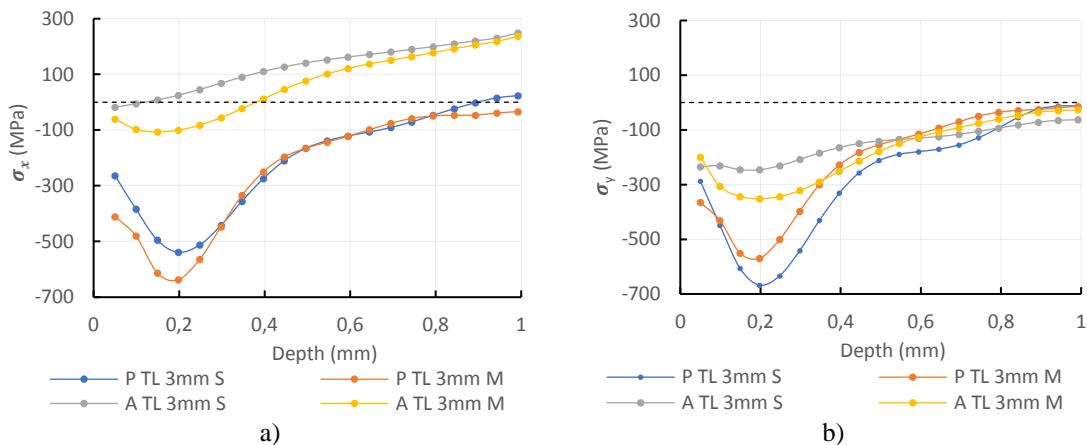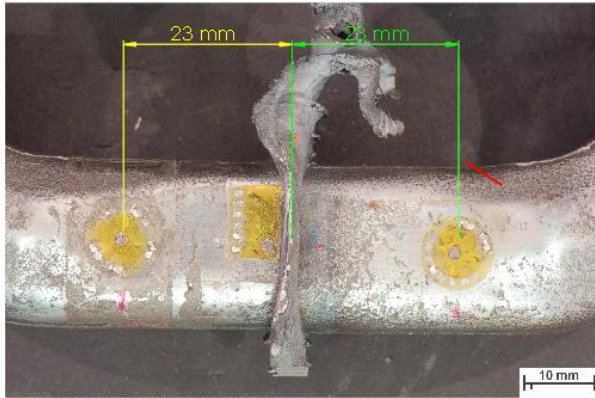Figure 47 - Location of the measurements a)**A** and b)**P** condition in **TL** location

Figure 48 - Comparison between a) σ_x and b) σ_y in the **TL** location (**A** and **P** conditions)
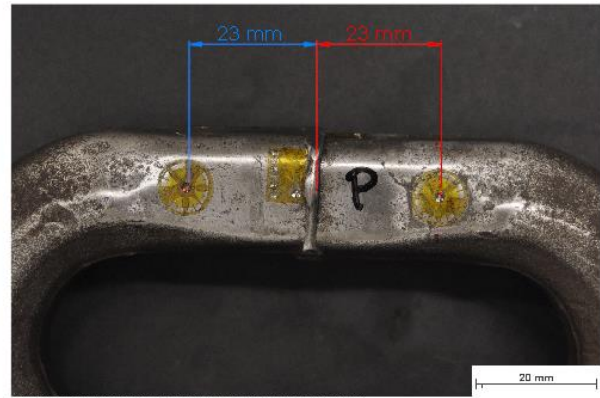
Figure 49 - Location of the measurements (**A** and **P** condition in **TL** location away from WCL)
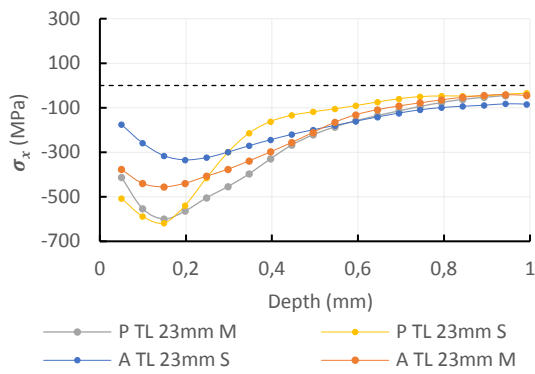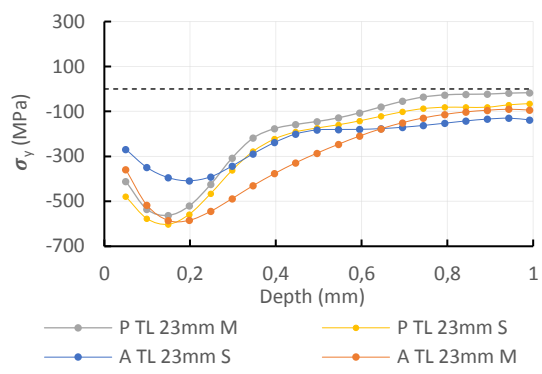
a)   b)

Figure 50 - Comparison between a) σ$_x$ and b) σ$_y$ in the **TL** location (**A** and **P** conditions)
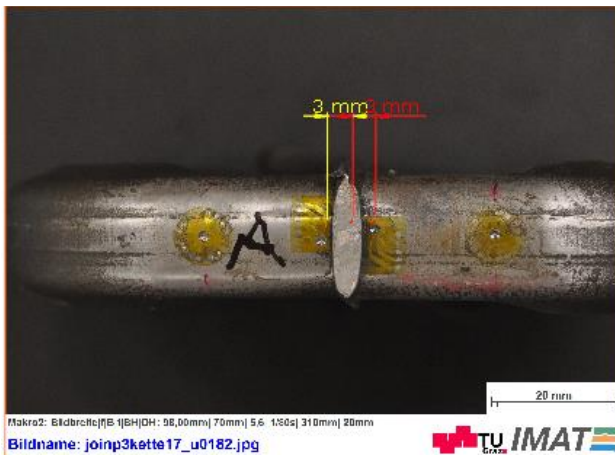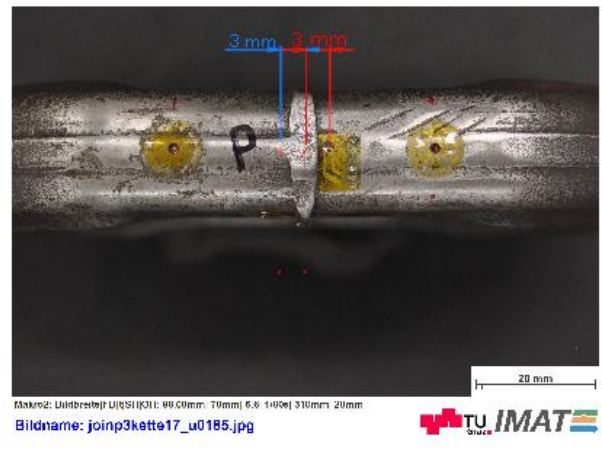
Figure 51 - Location of the measurements a) A condition and b) **P** condition **LS** location)

Figure 52 - Comparison between a) σ_x and b) σ_y in the **LS** location (**A** and **P** conditions)

5.2 X-Ray Diffraction results
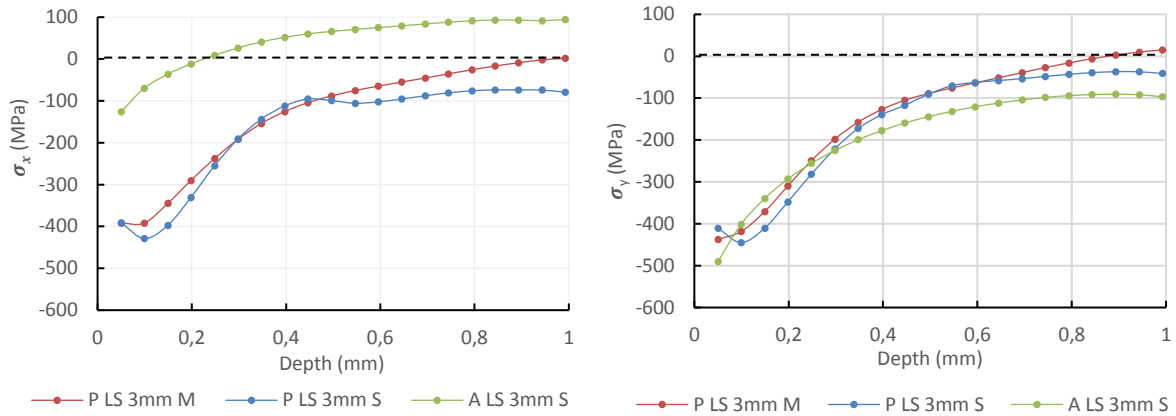
XRD measurements, mainly served the purpose of confirm the results obtained in the HD methodology and are discussed in this section. **$\sigma_{45°}$** is defined as the stress in a bisecting direction between **σ_x** and **σ_y**. The standard deviation of the stress values obtained is due to the deviation in the measurement of the d-spacing (plotted d curve against $sin^2(\varphi)$). Since it was not pretended to evaluate the symmetry (proven in **P** condition) while knowing that the **N** condition did not cause significant differences, there were not performed measurements in both **M** and **S** parts of the chain link in the **N** and **P** conditions. Away from the HAZ, what predominates in the RS field is the shot peening effect. At the end of the section, a summary of all conditions is presented.

5.2.1   *F condition*

The results for the **F** condition are presented in the following Table 6 and Figure 53. All the stresses obtained are from compressive nature as it was expected from the shot peening condition. When referring to the x direction, it is seen that the highest stress in absolute value is 25mm away from what would be the WCL and the lowest one is at 20mm. The difference between the maximum and minimum values is bigger in the **LS** location in both x and y directions which might be explained to the geometry of the surface since it is not completely flat. According to the literature, a minimal sample or diffractometer positioning error of 0,025mm can cause errors of ±14 MPa [76]. The difference between the maximum and minimum values is 90 MPa which might be due to the roughness introduced to the surface by the shot peening effect. On the **LS** surface, the biggest variation also occurs in the x direction (116 MPa). In the y direction on the **TL** surface, there was a variation of only 28 MPa. The discrepancy was bigger again on the **LS** reaching an 85 MPa difference. This behaviour was also verified in the **$\sigma_{45°}$**, since the difference reached 55 MPa on the **LS** while reaching only 45 MPa on the **TL**. Nonetheless for each individual position the standard deviation did not surpass 8 MPa

Condition F	TL surface			LS surface		
Distance (mm)	σ_x(Mpa)	σ_{45^o}(Mpa)	σ_y(Mpa)	σ_x(Mpa)	σ_{45^o}(Mpa)	σ_y(Mpa)
5	-387±8	-383±3	-386±4	-302±5	-354±6	-389±5
10	-395±6	-416±5	-412±6	-416±6	-398±5	-395±4
15	-361±6	-371±4	-400±4	-418±5	-409±6	-412±7
20	-360±4	-397±5	-414±5	-380±7	-383±6	-438±6
25	-430±7	-409±4	-398±13	-379±7	-372±5	-353±6
Average	-386,6	-395,2	-402	-379	-383,2	-397,4

Table 6 – Results obtained by XRD for the as forged condition.
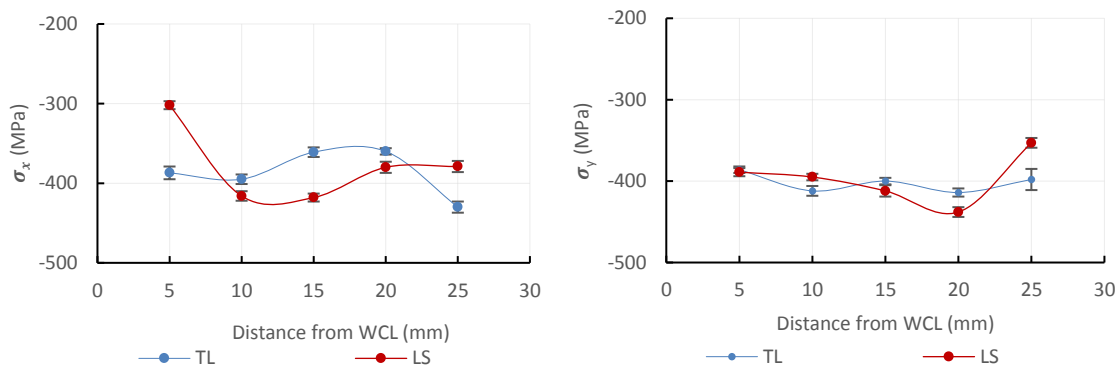

Figure 53 - XRD results obtained for the F condition

5.2.2 A condition

The measurements in both the **S** and **M** parts were performed only in the **A** condition to confirm the symmetry obtained in the HD method. The graphs for each point are also shown below in Figure 54, Figure 55 and Table 7.

In the **TL** location of the chain links, in x and 45º directions, the variations between the stationary and moving parts are small. There are big variations 25mm away from the WCL which might be due to the curvature present on this chain model in this position. Therefore, this point will be neglected in the following analysis. In all the other points, the results can be considered symmetric since the biggest variation occurs at 15mm from the WCL (56 MPa). Consequently, the XRD results in the direction of the oscillatory movement, confirm the symmetry obtained in the HD. In the direction of the forging force, the highest variation is at 5mm. Where the differences observed were also bigger in this direction although they could be considered neglectable.

In the **LS** location, the variations are higher which might be due to the present groove caused by the forging procedure (before welding). The highest variation in the stress magnitude between the stationary and the moving parts occurs at 10 mm and -10 mm from the WCL. This result is also in agreement with the HD results since the biggest variations were also observed in the **LS** location (probably due to the non-flatness of the surface).

Condition A	TL surface			LS surface		
Distance from WCL (mm)	σ_x(Mpa)	$\sigma_{45°}$(Mpa)	σ_y(Mpa)	σ_x(Mpa)	$\sigma_{45°}$(Mpa)	σ_y(Mpa)
-25	-376±6	-405±6	-446±5	-323±13	-313±8	-379±14
-20	-374±5	-368±6	-424±5	-416±11	-426±5	-411±27
-15	-422±4	-452±7	-467±5	-363±7	-376±8	-357±21
-10	-464±5	-455±5	-440±8	-396±9	-371±11	-341±25
-5	-409±7	-381±6	-413±4	-318±6	-290±5	-259±12
5	-381±3	-375±4	-337±7	-427±8	-413±7	-400±8
10	-459±5	-449±7	-411±7	-539±9	-556±9	-421±12
15	-379±9	-396±4	-403±5	-447±7	-478±14	-485±10
20	-383±6	-422±6	-442±4	-422±11	-470±7	-509±16
25	-271±8	-268±8	-311±7	-436±13	-466±8	-543±25
Average	-391,8	-397,1	-409,4	-408,7	-415,9	-410,5

Table 7 - Results obtained by XRD for the as welded condition
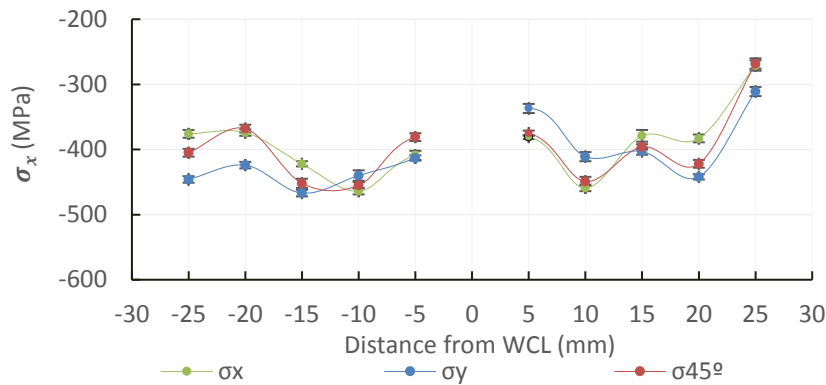

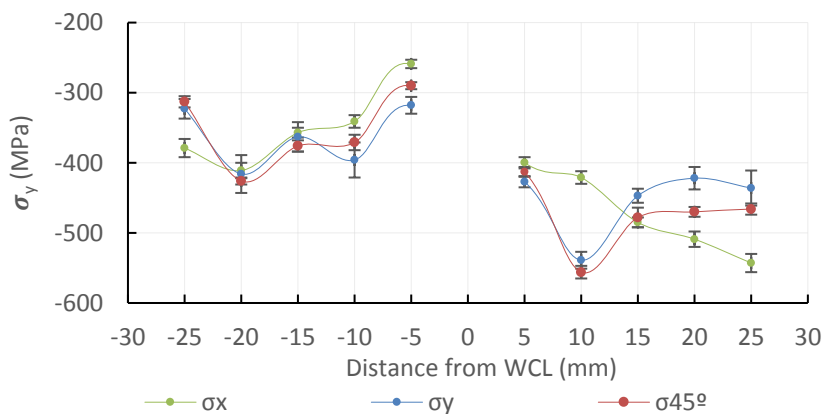Figure 54 - XRD results obtained for the A condition (TL location)

Figure 55 - XRD results obtained for the A condition (LS location)

5.2.3 N condition

The results for the **N** condition are summarized in the following Figure 56 and Table 8. σ_y seems to

have overall higher absolute values than σ_x. Also, as referred before, the effect that predominates in inducing RS field in the regions where the measurements were performed is the shot peening one. Thus, significant differences were not observed although along the whole surface besides the measurement at 25 mm from the WCL. This might be due to the non-flatness of the surface in this region as addressed before.

Condition N	TL surface			LS surface		
Distance from WCL (mm)	σ_x(MPa)	σ_{45^o}(MPa)	σ_y(MPa)	σ_x(MPa)	σ_{45^o}(MPa)	σ_y(MPa)
5	-385±5	-314±5	-299±3	-327±5	-354±6	-370±5
10	-376±6	-334±5	-323±4	-430±7	-398±5	-441±3
15	-372±5	-378±4	-398±4	-411±4	-409±6	-459±5
20	-431±6	-414±5	-416±6	-413±5	-383±6	-477±5
25	-183±8	-193±6	-172±9	-372±5	-372±5	-466±6
Average	-349,4	-326,6	-321,6	-390,6	-383,6	-442,6

Table 8 – Results obtained by XRD for the as welded without flash condition.
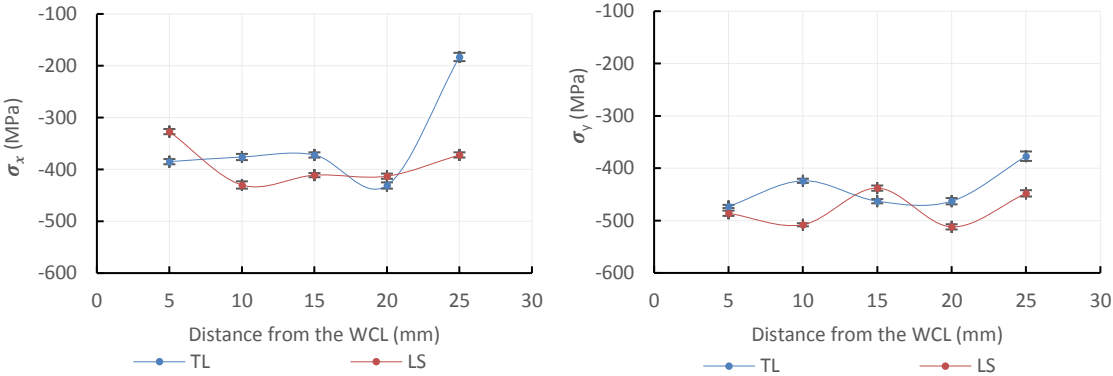

Figure 56 - XRD results obtained for the **N** condition.

5.2.4 P condition

To understand the effect of the PWHT at the surface of the specimens, there were performed measurements in the exact same locations as for the **F**, **A** and **N** conditions. The stress values obtained for **P** are summarized in the following Figure 57 and Table 9.

The results obtained after PWHT seemed to show higher absolute values of the compressive stress state field in both **TL** and **LS** which can increase the fatigue life of the component. It also showed an overall stabilization (smaller maximum amplitudes) when compared to the **N** and **A** conditions as it is shown in the graphs below.

When superposing the XRD results for all the conditions (see Figure 58 and Figure 59), there seems to be no pattern in the differences between them. At the surface of the specimen there are almost no differences observed due to the welding procedure, nor to the flash removal. In the regions where XRD was performed, the effect that predominates is the shot-peening peening effect. It was proven by

previous authors that the RS results from the shot peening effect can have variations like the ones obtained in this project. *Prevey et al.* [77] concluded that XRD by itself is not enough to characterize the shot-peening effects. The author stated that in-depth measurements would be the only way to characterize this condition in a reliable way since the obtained RS values also depend on the thermomechanical history of the component prior to the shot peening surface treatment.

Condition P	TL surface			LS surface		
Distance from WCL (mm)	σ_x(MPa)	σ_{45^o}(MPa)	σ_y(MPa)	σ_x(MPa)	σ_{45^o}(MPa)	σ_y(MPa)
5	-423±14	-430±10	-473±9	-467±6	-314±5	-486±7
10	-401±4	-388±6	-424±6	-451±7	-334±5	-508±3
15	-424±4	-408±6	-463±7	-405±5	-378±4	-438±7
20	-394±6	-427±6	-463±6	-454±7	-414±5	-512±6
25	-377±9	-381±6	-377±11	-414±6	-193±6	-448±5
Average	-403,8	-406,8	-440	-438,2	-326,6	-478,4

Table 9 - Results obtained by XRD for the as welded without flash after PWHT condition.
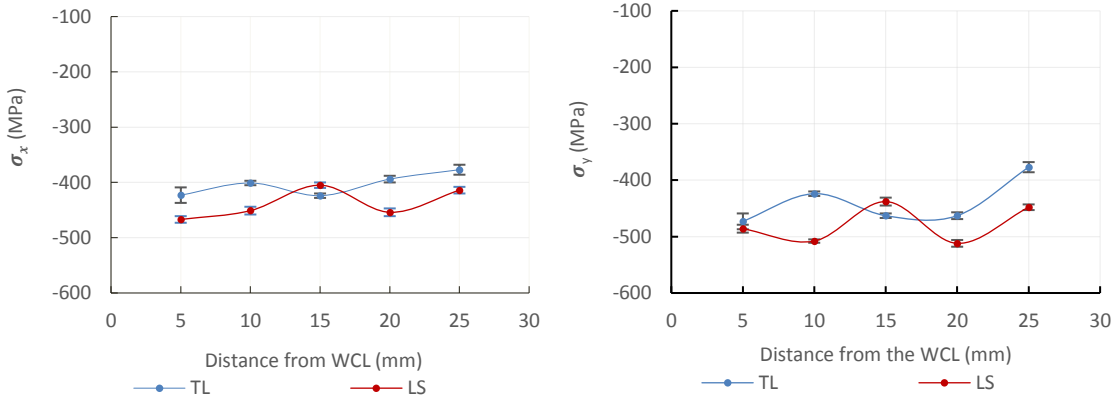

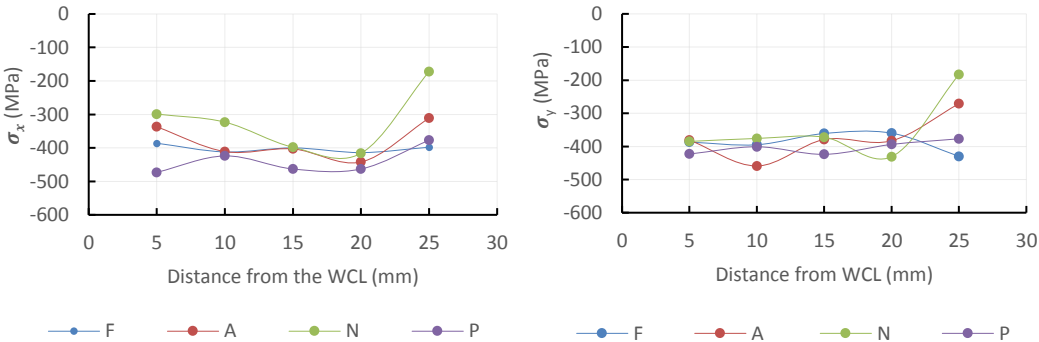Figure 57 - XRD results obtained for the P condition

Figure 58 - Comparison of xrd measurements in all conditions for TL location
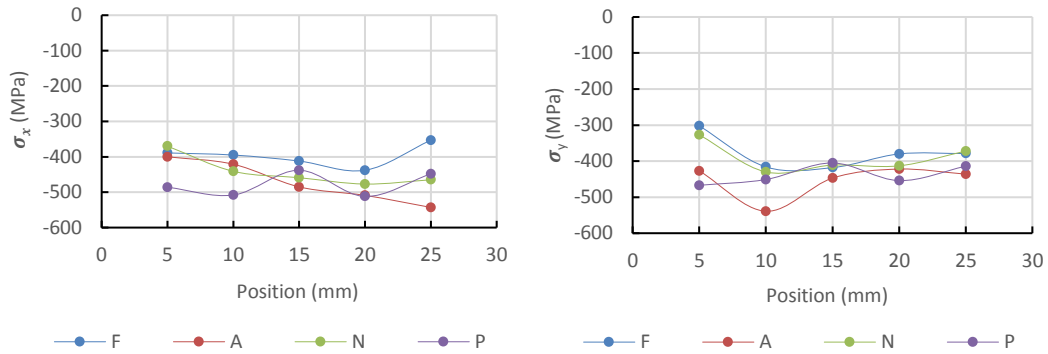
Figure 59 - Comparison of xrd measurements in all conditions for LS location

5.3 Agreement between both methods

In the previous section, an interpolation of 20 steps was used to calculate the RS values obtained in the HD since the stress values didn't change significantly with a bigger number of steps. Previous expertise in HD showed that the Kockelmann method was the calculation method that provided the best results to perform these measurements. However, when it is pretended to compare HD results with XRD measurements, more calculation methods should be tested to see which ones fits the best. It is expected that the values of both methods are not quantitatively equal. Although there are some patterns that show that the results obtained in each method are in quite good agreement. To compare the HD Kockelmann results with XRD ones, a 200 steps interpolation was used. In the case of the Integral method, 100 steps were used to obtain the same minimum depth (0,005 mm). This method relies on using step-wise functions constant throughout the hole depth to calculate the strain relief. It is based on the calculation three integral functions that contain influence parameters that can be obtained through finite element model (fem) computations. This way the results of both calculation methods are in line with the penetration of the x-ray beam (5 µm). The ASTM method could also be compared although it didn't show reliable results to the analysis performed. To obtain the exact comparison of both methods, the XRD measurements should also be performed in depth using surface layer removal methods such as electrolytic polishing [78].

5.3.1 *F condition*

When comparing the stress values obtained from each method it is seen that both provide compressive stress values with the same order of magnitude. As shown before, the XRD measurements for this condition provide systematically higher stresses in the y direction which opposes the HD results. Below, in Table 10 there is a comparison of the result obtained in the first depth increment in the HD at 23 mm from what would be the WCL with the surface measurement at 20mm obtained by XRD for both **TL** and **LS** locations.

It is seen that all the XRD points provide higher compressive stresses than the ones obtained in HD except the point in **LS** 20 mm. This location is more susceptible to measurement errors in both tests since the surface is not completely flat. There might be differences related to misalignment of

diffractometer and surface roughness in the XRD measurements as explained in [78]. There can also occur errors in HD tests if the strain-gage foil is not completely drilled. In the **TL** location, all XRD methods provide higher residual stresses than the HD either using the Kockelmann or the integrals method. In the **LS** location it can be observed the opposite. Besides all the previous considerations the results are in good agreement since all the variations are small and the **LS** location has a groove that may influence the diffraction peak. It should also be considered that the HD results obtained at this depth will contain errors since 0,005 mm depth has the same order of magnitude than the strain-gage foil. *Frendo et al.* [78] studied the RS field in a shot-peened aluminium alloy using the same techniques and obtained similar differences. The authors also obtained higher values of compressive stresses in XRD measurements.

Location of the Measurement	HD Kockelmann σx (MPa)	HD Kockelmann σy (MPa)	HD Integral σx (MPa)	HD Integral σy (MPa)	XRD σx (MPa) (20mm)	XRD σy (MPa) (20mm)
TL 23mm	-329,6	-293,3	-322,8	-288,7	-360	-414
LS 23mm	-336,2	-417,7	-604,2	-340,2	-438	-380

Table 10 – Stress values of different calculation methods used in HD and XRD measurements compared (**F** condition).

Location of the measurement	XRD/Kockelmann x direction (%)	XRD/Kockelmann y direction (%)	XRD/Integral [x direction] (%)	XRD/Integral [y direction] (%)
TL 23mm	8,4	29,2	10,3	30,2
LS 23mm	23,2	-9,9	-37,9	-10,4

Table 11 - Differences between XRD measurements and different calculation methods (**F** condition).

5.3.2 *A condition*

Again, to this comparison there were used the HD points at 23mm from the WCL at the first depth increment (0,005 mm) for both the **S** and **M** conditions. The results obtained for each method and the comparison between them is shown in Table 12 and Table 13.

Again, there is a sistematic increase in the compressive stress values in the XRD results except for the measurement in the **LS** 23mm **M** in the y direction. As explained before, 5 to 25 mm away from the WCL the condition that imposes the RS field is the shot-peening. Therefore, comparisons were not made with the HD measurements at 3 mm. Again, it is observed the same behaviour where the XRD values are slightly more compressive than the HD ones for all locations except for the **LS** when using the integral method. This difference in the values might be explained by the present groove in this location as explained before. The integral method seems to have an overall better agreement with the XRD measurements as stated in previous literature. This difference was stated in previous literature, [79] in

which there was made a comparison of the results obtained from both calculation methods.

Location of the Measurement	HD Kockelmann σx (MPa)	HD Kockelmann σy (MPa)	HD Integral σx (MPa)	HD Integral σy (MPa)	XRD σx (MPa) (20mm)	XRD σy (MPa) (20mm)
TL 23mm S	-112,2	-164,2	-185,6	-256,5	-374	-424
TL 23mm M	-256,5	-153,84	-392,7	-246,2	-442	-383
LS 23mm S	-121,9	-115,3	-171,9	-180,8	-438	-411
LS 23mm M	-336,16	-417,7	-493,7	-601,6	-422	-509

Table 12 - Stress values of different calculation methods used in HD and XRD measurements compared (**A** condition).

Location of the measurement	XRD-Kockelmann x direction (%)	XRD-Kockelmann y direction (%)	XRD-Integral [x direction] (%)	XRD-Integral [y direction] (%)
TL 23mm S	70	61,3	50,4	39,4
TL 23mm M	43,75	59,8	11,2	35,7
LS 23mm S	72,2	71,9	60,8	-6,6
LS 23mm M	20,3	17,9	-16,9	-18,2

Table 13 - Differences between XRD measurements and different calculation methods (A condition).

5.3.3   *N condition*

Again, the method that gives the best comparison is the Integral one. The high differences between the XRD and the HD results might be explained by a variety of factors: the fact that the location of each HD and XRD measurement performed is not the same; by the fact that the penetration depth of the x-ray beam is assumed as a constant in this calculation (5 μm); and from errors that may come due to the bad surface preparation or drilling the strain gage forl. Although both HD methods and the XRD results remain in the same order of magnitude. The trend that the XRD results give higher absolute stress values is confirmed between all methods except for **TL** 23mm **M** when compared with 20 mm with the integral method.

Location of the Measurement	HD Kockelmann σx (MPa)	HD Kockelmann σy (MPa)	HD Integral σx (MPa)	HD Integral σy (MPa)	XRD σx (MPa) (20mm)	XRD σy (MPa) (20mm)
TL 23mm M	-88,4	-28,1	-327,3	-591,2	-431	-416
LS 23mm M	-145,5	-100,8	-218,5	-159	-413	-477

Table 14 - Stress values of different calculation methods used in HD and XRD measurements compared (**F** condition).

Location of the measurement	XRD-Kockelmann x direction (%)	XRD-Kockelmann y direction (%)	XRD-Integral [x direction] (%)	XRD-Integral [y direction] (%)
TL 23mm M	88	93,2	24,1	-42,1
LS 23mm M	64,8	78,9	47,9	66,6

Table 15 - Differences between XRD measurements and different calculation methods (N condition).

5.3.4 *P condition*

In this condition, only one point stood out, where the stresses from the HD method were bigger than in the XRD measurements. It happened only at **TL** 23 mm **M** when using the integral calculation method. Besides this point, all the values showed the same trend mentioned before. Again, the integral method is the one that provides lower error margins when compared to the XRD (see Table 16 and Table 17).

Location of the Measurement	HD Kockelmann σx (MPa)	HD Kockelmann σy (MPa)	HD Integral σx (MPa)	HD Integral σy (MPa)	XRD σx (MPa) (20mm)	XRD σy (MPa) (20mm)
TL 23mm M	-49,8	-28,07	-327,3	-591,2	-360	-414
LS 23mm M	-145,5	-100,78	-218,5	-159	-438	-380

Table 16 - Stress values of different calculation methods used in HD and XRD measurements compared (**F** condition).

Location of the	XRD-Kockelmann x direction (%)	XRD-Kockelmann y direction (%)	XRD-Integral [x direction] (%)	XRD-Integral [y direction] (%)

measurement				
TL 23mm M	86,1	93,7	9,1	-42,8
LS 23mm M	66,7	73,5	50,1	58,1

Table 17 - Differences between XRD measurements and different calculation methods (N condition)

5.4 Microstructural and microhardness characterization

5.4.1 Microstructural characterization

In this section, there are shown the different microstructure zones observed after the welding procedure. It is also shown the difference of the average grain size in all zones. The differences in the microstructure of the 4 conditions studied in this dissertation are also analysed globally and locally (for the weld centre zone WCZ, the TMAZ, the HAZ and the BM). In the following Figure 60 there are shown the differences between each region of the weld in a **N** specimen. Since the cutting of the flash doesn't produce any microstructural changes, the microstructure was considered the same for the **A** and **N** conditions. It was also analysed the microstructure of the **P** condition to understand the main differences between them. Since the BM does not suffer any microstructural changes either, this region in the **N** condition can be assumed to have the same microstructure than the **F** condition.

Regarding the post weld heat treated condition, no significant changes were observed in the microstructure along the whole weld region. The grain size remained constant along the whole weld having around 11 ±1,45 μm.

The BM presented in Figure 61 Figure 60 - Macrograph of the different weld zones (N condition). a) shows a very homogeneous grain with the same microstructure in the whole surface of this region. The grain size calculated for this region was 8,371 ±0,57 μm showing an elongation in the direction of the rolling.

The HAZ presented in Figure 61 b) is still affected by the thermic cycle of the welding process although the changes observed in the microstructure were not so evident as in the other weld regions. The grains are more elongated than the ones observed in the BM with a size of 13,425 ±1,413 μm.

The TMAZ shown in Figure 61 c) is characterized by highly elongated and deformed grains since it is a zone that is subjected both to the thermic cycle and plastic deformation due to the friction force. The grain size increases to 24,19 ±4,52 μm.

The WCZ shown in Figure 61 d) is the zone subjected to the highest temperature exposure and plastic deformation. This promotes the dynamic recrystallization of the material. This region is also

characterized by its fully martensitic structure and highest hardness among all regions analysed. Due to recrystallization, it's the region with the smallest grain size (~5,989 ±0,63 µm). The high standard deviations are mainly due to the complications found in distinguishing the grain boundaries with all the etchants tried in this project. All these different zones have previously been reported in the literature such as the publication by Zhao *et al.* [19], where he concluded that the microstructure of a LFW titanium joint consisted mainly in a recrystallized grain zone (WCZ), and highly deformed and partially recrystallized area (TMAZ) and dissolved secondary α in the HAZ.
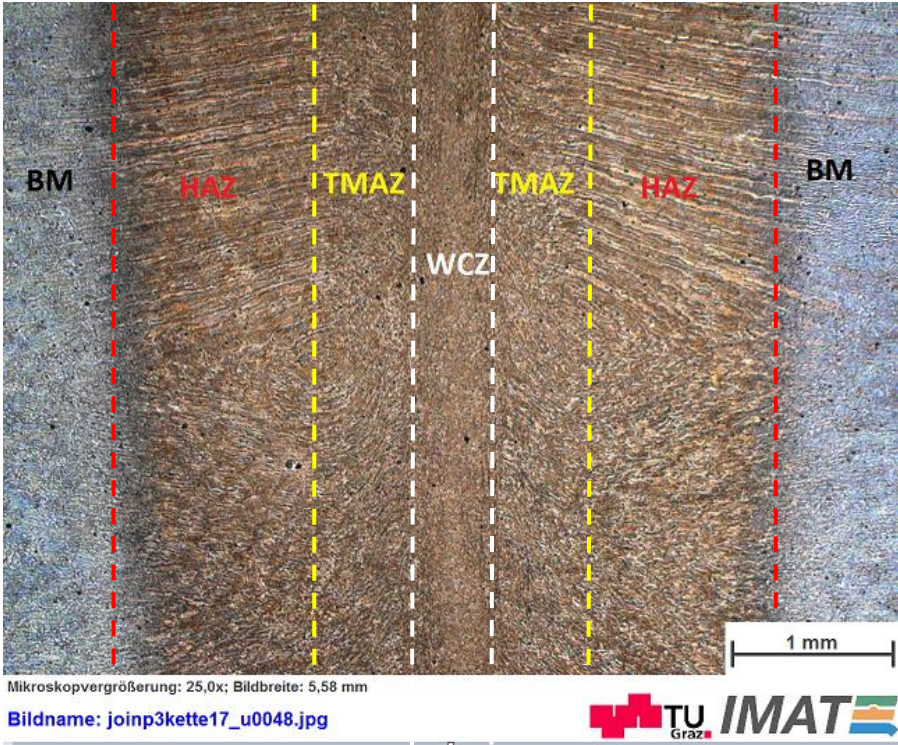
Figure 60 - Macrograph of the different weld zones (N condition).
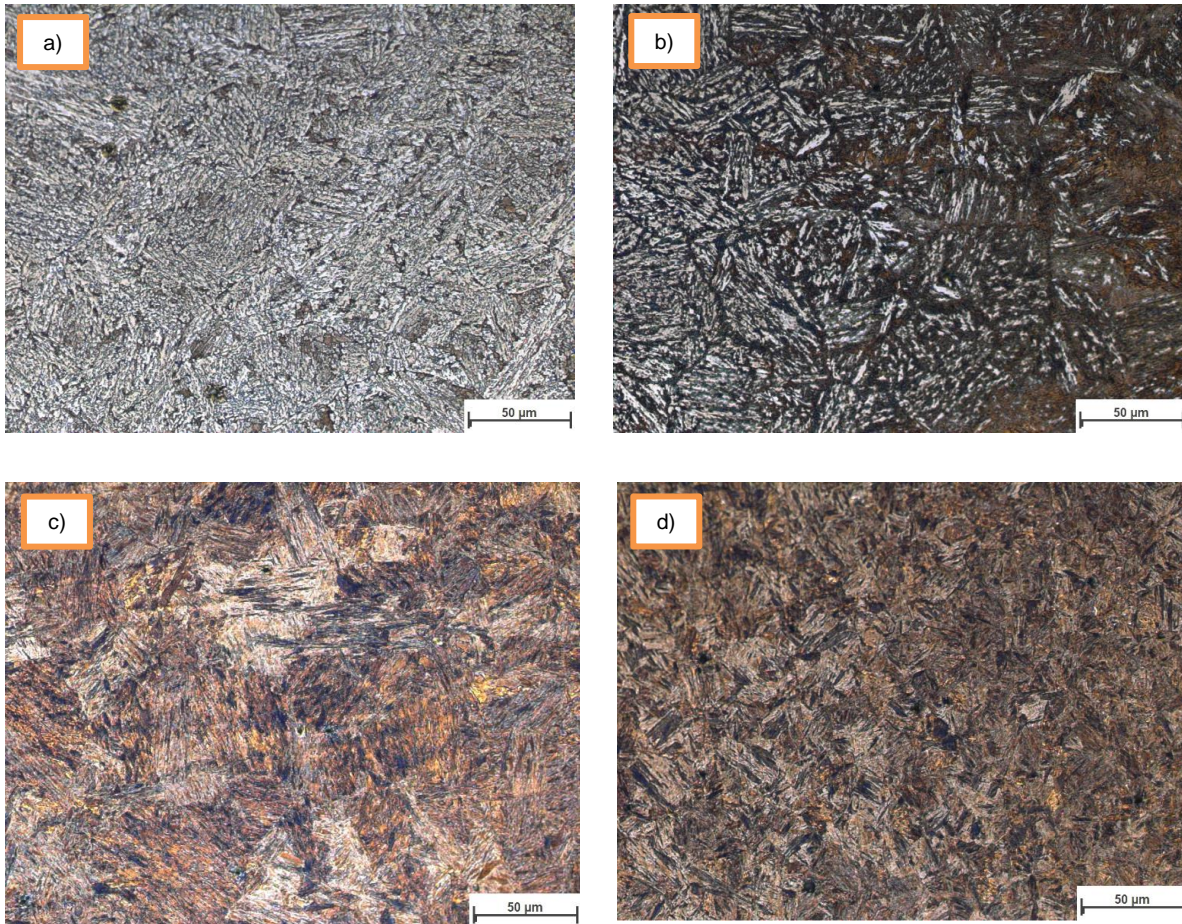
Figure 61 - Micrographs of the different weld zones (500x – Lepera etching): a) BM; b) HAZ; c) TMAZ; d) WCZ

5.4.2 Microhardness measurement

Considering that the size of the HAZ and TMAZ is not easily measurable, it was performed a microhardness mapping of the weld. Again, it was considered that the flash cutting didn't induce any microstructural/microhardness changes in the weld zone. Thus, this condition (**N**) was the one to characterize. To compare the effect of the PWHT, the same microhardness profile was calculated along the weld. The base material has an average of 350 $HV_{0,5}$. When approaching the weld region, this value starts to decrease in the HAZ to a minimum of 338 $HV_{0,5}$. Considering that in this region the temperature reached is not as high as in the TMAZ and WCZ, it can be observed a recovery effect in the BM zone adjacent to the HAZ which lowers the hardness values.

When approaching the TMAZ, where the material suffers higher thermal cycles and plastic deformation, the hardness values also start to rise until around 500 $HV_{0,5}$ due to the higher cooling rates experienced after the weld. In this zone there is an important phenomenon of coarsening of the grains that should be considered.

In the WCZ, the plastic deformation and temperature to which the material is subjected is extreme.

These thermomechanical cycles cause the dynamic recrystallization of the microstructure greatly diminishing the grain size. This fact, along with the high cooling rates experienced in this region are strengthening mechanisms that notably increase the hardness values to a maximum of 517 $HV_{0,5}$ as shown in Figure 62.

With the microhardness map it is also possibly to identify the width of each of the weld regions stated before:

- WCZ has approximately 1,5 mm.
- TMAZ has roughly 0,2 mm
- HAZ has nearly 1,2 mm
- BM around 3,1 mm

When analysing qualitatively the microhardness profile, good agreement was obtained with the width of the different weld regions seen in the micrographs as well as with the average grain size calculations. The hardness values are also in agreement with the Hall-Petch relation where it is said that the grain size is inversely proportional to hardness values. In the **N** condition, the grain size is bigger in the TMAZ showing the lowest hardness result. Through dynamic recrystallization the grain size starts to decrease when it gets to the WCZ which causes the hardness in this region to increase greatly. In the **P** condition, it is observed that the grain size does not vary significantly between the WCL and BM. Thus, the hardness is maintained the same along the whole weld. In the annealed samples (**P** condition) it was quite difficult to distinguish the different weld regions when looking at it at the microscope. Therefore, in the creation of the microhardness profile it was assumed that they have the exact same extent of the ones obtained in the microhardness of the **N** condition. This profile is shown below in Figure 63 superposed with the previous one. In the **P** condition it can be seen the hardness increase when compared to the base material that was not post weld heat treated. This condition has an average hardness of 400 $HV_{0,5}$ along the whole weld (base material to the WCZ) and no significant differences were observed. The microhardness map of the **P** condition shows the hardness recovery of around 100 $HV_{0,5}$ in the WCZ and TMAZ. It should be also taken into consideration that the **P** and the **N** samples compared were not the same. Therefore, differences that may recall the forging procedure will be reflected in these hardness values. The hardness increase when comparing it to the base material and the decrease of values in the weld region due to the annealing are both stated in the literature. *Mohamed et al.* [80] investigated different annealing times and temperatures in nanocrystalline nickel and they discovered that until a certain annealing temperature the hardness values increased and only started to decrease at a determinate temperature depending on the annealing time used.
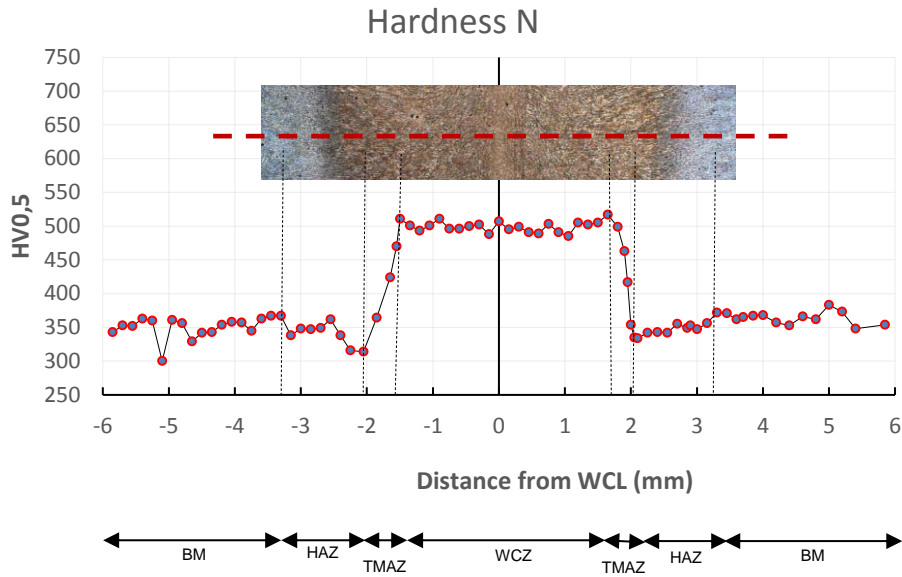
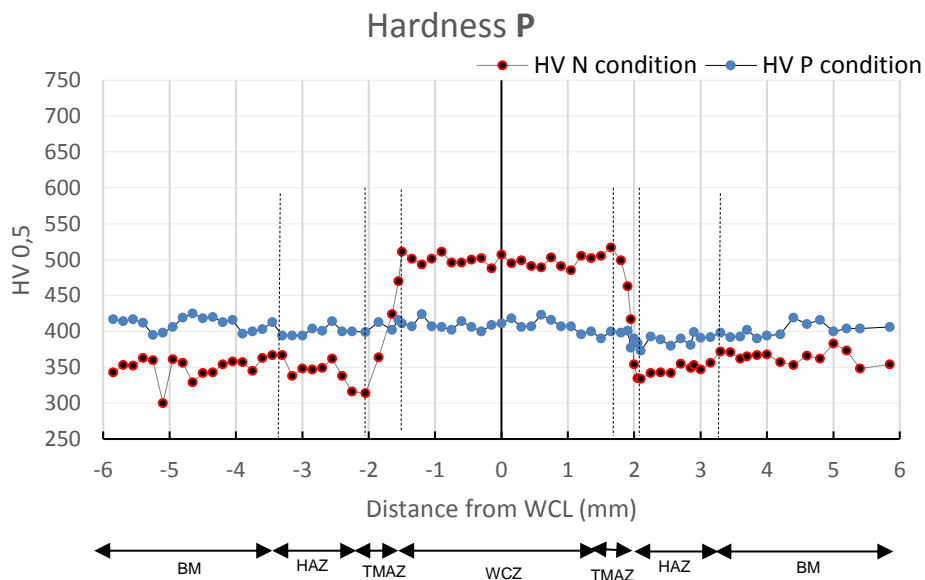Figure 62 - Microhardness profile of the **N** condition

Figure 63 - Microhardness profile of the **P** condition

This project allowed to fully understand the evolution of the RS field along the main manufacturing steps of the linear friction welded "Hero" chain link. The influence of the welding process, flash removing process and PWHT were investigated using both SDT and NDT and the results compared. A microstructural and microhardness characterization was also performed in the conditions thought to be relevant to analyse (**N** and **P**). The results obtained are reliable since the tests were performed according to the standards available. The project permitted to obtain concluding remarks that will be stated in the following Chapter 6. Although this project allowed to enrich the scientific knowledge on the topic there is still investigation that could be done to improve the expertise in LFW of high strength steel chains which is proposed in the same chapter.

Chapter 6 - Conclusions and future work

The main conclusions to this work are presented in this chapter according to the objectives addressed before. The work performed allowed to characterize the RS field in the LFW chain links close to its surface. It also confirms the success in manufacturing steel chains using LFW with the inherent advantages that arise from it.

- Both the HD and the XRD proved to be complementary solutions when analysing the residual stress field. The results from each method were in good agreement considering the differences present in the previous literature on the subject;

- The HD method showed that the **F** condition had similar residual compressive stresses in all the locations measured. It confirmed the shot peened condition of the samples;

- It was proven that due to the welding process the residual stresses switched from compressive to tensile near the WCL. Away from it, the stresses did not change significantly. This proved that the joining process has a great degree of influence in the RS field

- The HD has shown symmetry of the residual stress field between the stationary and the moving parts of the LFW process. In the x direction there was observed a difference of less than 100 MPa in the first half of the hole depth, decreasing to almost no difference in the second half. In the y direction, the behaviour of the stress field is nearly the same with the stresses having nearly the exact same value at 0,6mm depth;

- Symmetry was obtained when comparing the RS field of the Top and Bottom sides of the chain link. In the x direction there was only observed a difference of less than 50 MPa in the first 0,2mm of depth in the hole drilling and around 10 MPa at the last 0,2mm. In the direction of the forging force there is a constant difference of less than 100 MPa along the whole depth of the hole which can also be neglected;

- When comparing the left and the right regions of the chain links, symmetry was also observed. In the x direction, there was a slight difference in the first and last 0,2mm of the hole depth. In the y direction, an almost constant difference of less than 100 MPa was obtained along the whole depth of the hole;

- The flash removal procedure used by the company seems to have no influence on the RS field either close or away from the WCL. It also seemed to not cause any differences whether considering the x or the y direction;

- Away from the WCL, in the **P** condition, the RS field has higher values of compressive stresses when compared to conditions not subjected to PWHT.

- The PWHT applied switches the tensile stresses due to the welding process into compressive stresses.

- The PWHT applied uniformizes the stress field in every location (either on the WCL or away from it). It also uniformizes the hardness along the whole weld. Both the hardness and the RS field seem to have no significant differences between the different locations measured

(close and far away from the WCL) after the PWHT was applied.

- There was an increase of 50 $HV_{0,5}$ in comparison with the conditions before and after PWHT.
- The PWTH seemed to have influence only in the stresses measured close to the surface of the component. Inside the chain link all the results tend to the same values.
- The XRD results confirmed the HD results for the **P** condition with a smaller maximum amplitude between the stress values when compared to **A** and **N.**
- The integral method of calculation from the HD showed better agreement in the RS values than Kockelmann's.

Future work steps:

Future investigations in what concerns the RS field of LFW high strength steel chains are suggested to enrich the knowledge shown in previous chapters:

- Investigate the behaviour of the temperature profile after the welding process. Study if both the stationary and the moving components have the same cooling rates;
- Measure the RS field in steel chains welded with different forging forces or other welding parameters to study its influence in the stresses in the y direction;
- Study the influence of the direction of the movement in the LFW process in the RS field;
- Perform in-depth measurements of the RS field using the neutron diffraction to understand the maximum magnitude of the tensile stresses close to the WCL;
- Perform XRD measurements in the WCL to characterize the RS field at its surface;
- Perform XRD measurements in different samples in the same condition so it can be proved the repeatability of the method;
- Investigate the effects of surface preparation and geometry in XRD results;
- Investigate the evolution of the residual stress field along the whole manufacturing process in the exact same chain link. This could be achieved by performing XRD measurements in the same sample in-between each of the manufacturing steps studied.
- Use a numeric model to predict the residual stress field and compare it with the experimental results obtained;

References

[1]   K. Mucic, N. Enzinger, and F. Fuchs, "Linear Friction Welding of High Strength Chains," *Trends Weld. Res. Proc. 9th Int. Conf.*, no. January, pp. 752–756, 2013.

[2]   A. Vairis and M. Preuss, "Linear and rotary friction welding review," no. February, 2016.

[3]   A. Vairis and M. Frost, "Modelling the linear friction welding of titanium blocks," *Mater. Sci. Eng. A*, vol. 292, no. 1, pp. 8–17, 2000.

[4]   "DIN And EN Steel Standards Naming Conventions." [Online]. Available: http://zknives.com/knives/steels/stlhowtoreadendin.shtml.

[5]   The Welding Institute, "What are the microstructural constituents Austenite, Martensite, Bainite, Pearlite and Ferrite?" [Online]. Available: http://www.twi-global.com/technical-knowledge/faqs/material-faqs/faq-what-are-the-microstructural-constituents-austenite-martensite-bainite-pearlite-and-ferrite/.

[6]   M.-X. Zhang and P. M. Kelly, "The morphology and formation mechanism of pearlite in steels," *Mater. Charact.*, vol. 60, no. 6, pp. 545–554, 2009.

[7]   "Allotropes of iron," 2000. [Online]. Available: https://www.revolvy.com/main/index.php?s=Allotropes of iron.

[8]   "The Strengthening of Iron and Steel." [Online]. Available: http://www.totalmateria.com/articles/Art107.htm.

[9]   "The Hydrogen Problem _ WIA." [Online]. Available: http://www.welding.com.au/resources-articles/view/the-hydrogen-problem.

[10]   G. Murry and D. Kaplan, *Metallurgy and Mechanics of Welding*. 2008.

[11]   "History of welding." [Online]. Available: https://www.gowelding.org/articles/history-of-welding/.

[12]   K. Weman, *Welding processes handbook*. 2003.

[13]   W. Thomas, "Friction Stir Welding, FSW, Wayne Thomas and Solid state welding at TWI,." .

[14]   I. Bhamji, M. Preuss, P. L. Threadgill, and A. C. Addison, "Solid state joining of metals by linear friction welding: a literature review," *Mater. Sci. Technol.*, vol. 27, no. 1, pp. 2–12, 2011.

[15]   I. Bhamji, A. C. Addison, P. L. Threadgill, and M. Preuss, *Linear friction welding in aerospace engineering*. Woodhead Publishing Limited, 2012.

[16]   a. Vairis and M. Frost, "High frequency linear friction welding of a titanium alloy," *Mech. Eng. Univ. Bristol*, vol. 217, no. 1, pp. 117–131, 1998.

[17]   M. Romero, J. ; Preuss, "Effect of the forging pressure on the microstructure and residual stress development in Ti – 6Al – 4V linear friction welds," no. October, 2009.

[18]   A. Vairis and M. Frost, "On the extrusion stage of linear friction welding of Ti 6Al 4V," *Mater. Sci. Eng. A*, vol. 271, pp. 477–484, 1999.

[19]   Y. Ji, S. Wu, and D. Zhao, "Microstructure and Mechanical Properties of Friction," pp. 1–11, 2016.

[20]   T. Kuroda, K. Ikeuchi, and H. Ikeda, "Flash butt resistance welding for duplex stainless steels," *Vacuum*, vol. 80, no. 11–12, pp. 1331–1335, 2006.

[21] F. Zhang, B. Lv, B. Hu, and Y. Li, "Flash butt welding of high manganese steel crossing and carbon steel rail," *Mater. Sci. Eng. A*, vol. 454–455, pp. 288–292, 2007.

[22] TWI Ltd, "Resistance and Mechanical Joining." 2016.

[23] "pewag hero friction welded chain." [Online]. Available: https://hero.pewag.com/english.

[24] N. S. Rossini, M. Dassisti, K. Y. Benyounis, and A. G. Olabi, "Methods of measuring residual stresses in components," *Mater. Des.*, vol. 35, pp. 572–588, 2012.

[25] P. Sketchley, P. Threadgill, and I. Wright, "Rotary friction welding of an Fe 3 Al based ODS alloy," *Mater. Sci. …*, vol. 331, pp. 756–762, 2002.

[26] D. Walker, "Residual Stress Measurement Techniques," *Adv. Mater. Process.*, vol. 159, no. 8, pp. 30–33, 2001.

[27] C. Ruud, "Residual Stress Measurement," in *Analytical Characterization of Aluminum, Steel, and Superalloys*, CRC Press, 2005, pp. 429–471.

[28] R. H. Leggatt, "Residual stresses in welded structures," *Int. J. Press. Vessel. Pip.*, vol. 85, no. 3, pp. 144–151, 2008.

[29] P. M. Hansen, "Metallurgy and metallurgical engineering series." p. 678, 1958.

[30] P. J. Withers and H. K. D. H. Bhadeshia, "Residual stress part 1 - Measurement techniques," *Mater. Sci. Technol.*, vol. 17, no. 4, pp. 355–365, 2001.

[31] A. Civin and M. Vlk, "Theoretical Analysis of Ring-Core Method for Residual Stress Determination," *Konf. ANSYS 2009*, 2009.

[32] A. H. Mahmoudi, S. Hossain, C. E. Truman, D. J. Smith, and M. J. Pavier, "A New Procedure to Measure Near Yield Residual Stresses Using the Deep Hole Drilling Technique," *Exp. Mech.*, vol. 49, no. 4, pp. 595–604, 2009.

[33] Y. Kudryavtsev, J. Kleiman, O. Gushcha, V. Smilenko, and V. Brodovy, "Ultrasonic Technique and Device for Residual Stress Measurement," *2004 SEM X Int. Congr. Expo. Exp. Appl. Mech.*, pp. 1–7, 2004.

[34] "Ultrasonic _ VEQTER _ Residual Stress Experts." [Online]. Available: http://www.veqter.co.uk/residual-stress-measurement/ultrasonic.

[35] T. Hutchings, M., J. Withers, P., M. Holden, T., and T. Lorentzen, *Introduction to the characterization of residual stress by neutron diffraction*. .

[36] A. Youtsos, C. Ohms, and E. Commission, "NDT Based on Neutron Techniques in Support of Structural Integrity Assessment," vol. 7, no. 8. 2002.

[37] N. J. Rendler and I. Vigness, "Hole-drilling strain-gage method of measuring residual stresses," *Exp. Mech.*, vol. 6, no. 12, pp. 577–586, 1966.

[38] G. S. Schajer, "Measurement of Non-Uniform Residual Stresses Using the Hole-Drilling Method. Part I—Stress Calculation Procedures," *J. Eng. Mater. Technol.*, vol. 110, no. 4, pp. 338–343, Oct. 1988.

[39] G. S. Schajer, "Hole-Drilling Residual Stress Measurements at 75: Origins, Advances, Opportunities," 2009.

[40] ASTM E 837:2008, "Standard Test Method for Determining Residual Stresses by the Hole-Drilling Strain-Gages," vol. 1, pp. 1–17, 2008.
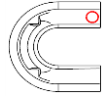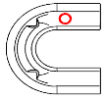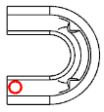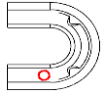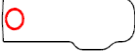
[41] "SINT MTS 3000 Manual," no. 4185870484. .

[42] P. V Grant, J. D. Lord, and P. Whitehead, "The Measurement of Residual Stresses by the Incremental Hole Drilling Technique," *Meas. Good Pract. Guid. No. 53 - Issue 2*, no. 2, p. 63, 2006.

[43] A. Baldi, "Residual Stress Measurement Using Hole Drilling and Integrated Digital Image Correlation Techniques," *Exp. Mech.*, vol. 54, no. 3, pp. 379–391, 2014.

[44] J. Lee, A. Vautrin, J. R. Lee, J. Molimard, and Y. Surrel, "Full-field optical techniques : Applications to strain measurement and mechanical identification Full-Field Optical Techniques : Applications to Strain Measurement and Mechanical Identification," no. August 2017, 2002.

[45] W. Wang, "Moiré Interferometry," pp. 1–41.

[46] D. Post and B. Han, "Moiré Interferometry," pp. 627–653.

[47] A. Asundi, "Moire Interferometry for Deformation Measurement," vol. 11, no. June, pp. 281–292, 1989.

[48] O. J. Løkberg, "Electronic Speckle Pattern Interferometry," in *Optical Metrology: Coherent and Incoherent Optics for Metrology, Sensing and Control in Science, Industry and Biomedicine*, O. D. D. Soares, Ed. Dordrecht: Springer Netherlands, 1987, pp. 542–572.

[49] W.-C. Wang, C.-H. Hwang, and S.-Y. Lin, "Vibration measurement by the time-averaged electronic speckle pattern interferometry methods," *Appl. Opt.*, vol. 35, no. 22, pp. 4502–4509, 1996.

[50] P. Whitehead, J. D. Lord, and D. Penn, "The Application of Digital Image Correlation for Measuring Residual Stress by Incremental Hole Drilling," in *Advances in Experimental Mechanics VI*, 2008, vol. 13, pp. 65–73.

[51] A. M. Korsunsky, M. Sebastiani, and E. Bemporad, "Residual stress evaluation at the micrometer scale: Analysis of thin coatings by FIB milling and digital image correlation," *Surf. Coatings Technol.*, vol. 205, no. 7, pp. 2393–2403, 2010.

[52] D. V Nelson, A. Makino, and T. Schmidt, "Residual Stress Determination Using Hole Drilling and 3D Image Correlation," vol. 0, no. 1, pp. 31–38, 2006.

[53] N. Sasaki and S. Odajima, "Stress-strain curve and Young's modulus of a collagen molecule as determined by the X-ray diffraction technique," *J. Biomech.*, vol. 29, no. 5, pp. 655–658, 1996.

[54] P. S. Prevéy, "a Method of Determining the Elastic Properties of Alloys in Selected Crystallographic Directions for X-Ray Diffraction Residual Stress Measurement," *Adv. X-Ray Anal.*, vol. 20, pp. 345–354, 1977.

[55] W. H. Bragg W. L., Bragg, "The Reflection of X-rays by Crystals," 1913.

[56] B. Standard, "Non-destructive Testing — Test Method for Residual Stress analysis by X-ray Diffraction," 2008.

[57] "Parameter Optimization of Friction Stir Welding Of AA8011-6062 Using Mathematical Method," *Procedia Eng.*, vol. 97, pp. 775–782, 2014.

[58] Y. M. Hwang, P. L. Fan, and C. H. Lin, "Experimental study on Friction Stir Welding of copper metals," *J. Mater. Process. Technol.*, vol. 210, no. 12, pp. 1667–1672, 2010.

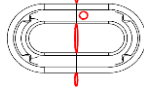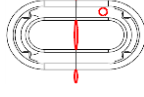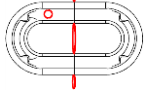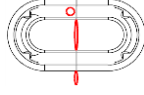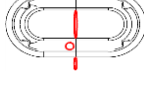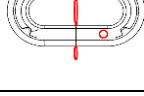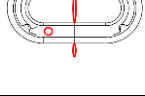[59] P. Heurtier, M. J. Jones, C. Desrayaud, J. H. Driver, F. Montheillet, and D. Allehaux, "Mechanical

and thermal modelling of Friction Stir Welding," *J. Mater. Process. Technol.*, vol. 171, no. 3, pp. 348–357, 2006.

[60]   M. E. Nunn, "Aero engine improvements through linear friction welding," *1st International Conference on Innovation and Integration in Aerospace Sciences, 4-5 August 2005, Queen's University Belfast, Northern Ireland, UK.* 2005.

[61]   B.J.Ginn and T. G. Gooch, "Toughness of 12 % Cr Ferritic / Martensitic Steel Welds Produced by Non-Arc Welding Processes," 1998.

[62]   B. Lang, T. C. Zhang, X. H. Li, and D. L. Guo, "Microstructural evolution of a TC11 titanium alloy during linear friction welding," *J. Mater. Sci.*, vol. 45, no. 22, pp. 6218–6224, Nov. 2010.

[63]   A. R. McAndrew, P. A. Colegrove, B. C. D. Flipo, and C. Bühr, "3D modelling of Ti–6Al–4V linear friction welds," *Sci. Technol. Weld. Join.*, no. December, pp. 1–9, 2016.

[64]   A. Vairis, "Mathematical modelling of the linear friction welding process," *J. Eng. Sci. Technol. Rev.*, vol. 5, no. 3, pp. 25–31, 2012.

[65]   R. Turner, J.-C. Gebelin, R. M. Ward, and R. C. Reed, "Linear friction welding of Ti–6Al–4V: Modelling and validation," *Acta Mater.*, vol. 59, no. 10, pp. 3792–3803, Jun. 2011.

[66]   K. Mucic, F. Fuchs, and N. Enzinger, "Process optimization for linear friction welding of high strength chain," in *EUROJOIN Conference*, 2012, pp. 157–166.

[67]   P. S. Effertz, F. Fuchs, and N. Enzinger, "Modelling the flash formation of linear friction welded 30CrNiMo8 high strength steel chains," *Int. J. Adv. Manuf. Technol.*, 2017.

[68]   "Stresstech - Xstress G3." .

[69]   C. H. Gür and S. Savas, "Measuring the Surface Residual Stresses in Shot Peened Steel Components by Magnetic Barkhausen Noise Method," no. April, pp. 16–20, 2012.

[70]   M. A. S. Torres, "An evaluation of shot peening , residual stress and stress relaxation on the fatigue life of AISI 4340 steel," vol. 24, pp. 877–886, 2002.

[71]   M. Smith, J.-B. Levesque, L. Bichler, D. Sediako, J. Gholipour, and P. Wanjara, "Residual stress analysis in linear friction welded in-service Inconel 718 superalloy via neutron diffraction and contour method approaches," *Mater. Sci. Eng. A*, vol. 691, no. February, pp. 168–179, 2017.

[72]   P. Xie, H. Zhao, Y. Liu, P. Xie, H. Zhao, and Y. Liu, "Measuring residual stresses in linear friction welded joints composed by dissimilar titanium Measuring residual stresses in linear friction welded joints composed by dissimilar titanium," vol. 1718, no. September, 2017.

[73]   S. Materialia, "Assessing welding residual stress in A335 P12 steel welds before and after stress-relaxation annealing through instrumented ... before and after stress-relaxation annealing through," no. May 2014, 2003.

[74]   D. Z. Ã, W. Jie, G. Zha, T. Wang, and G. Yang, "Effect of annealing on the residual stress and strain distribution in CdZnTe wafers," vol. 305, pp. 50–54, 2007.

[75]   M. Preuss, J. Q. da Fonseca, A. Steuwer, L. Wang, P. J. Withers, and S. Bray, "Residual Stresses in Linear Friction Welded IMI550," *J. Neutron Res.*, vol. 12, no. 1–3, pp. 165–173, 2004.

[76]   P. S. Prevéy, "X-ray diffraction residual stress techniques," *Met. Handbook. 10. Met. Park*, no. 513, pp. 380–392, 1986.

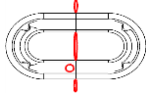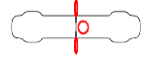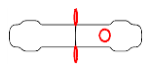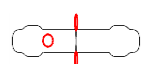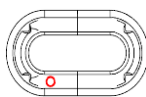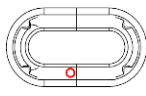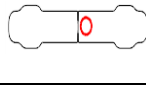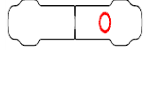[77]   P. S. Prevey, "X-Ray Diffraction Characterization of Residual Stresses Produced by Shot
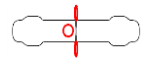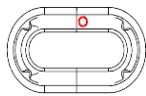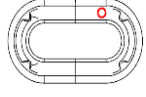
Peening."
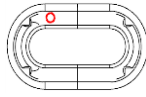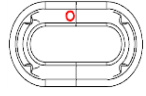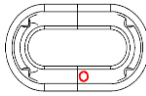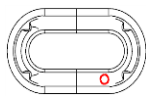
[78]   F. Frendo and U. Pisa, "Comparison of the hole-drilling and X-ray diffraction methods for measuring the residual stresses in shot peened ...," no. February 2014, 2005.

[79]   J. P. Nobre, M. Kornmeier, A. M. Dias, and B. Scholtes, "Use of the Hole-drilling Method for Measuring Residual Stresses in Highly Stressed Shot-peened Surfaces," pp. 289–297.

[80]   A. Torrents, H. Yang, and F. A. Mohamed, "Effect of Annealing on Hardness and the Modulus of Elasticity in Bulk Nanocrystalline Nickel," vol. 41, no. March, pp. 621–630, 2010.
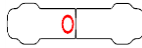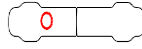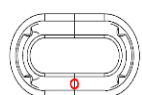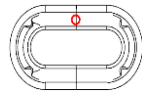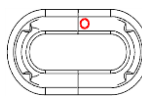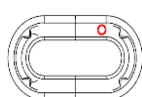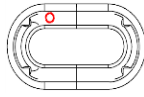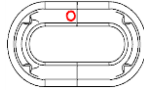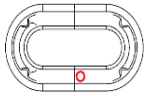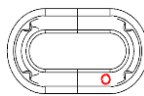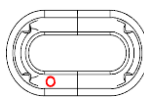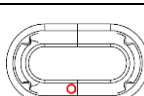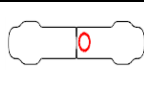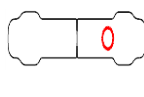
Measurement nr.	Sample code	Condition	Location	Moving/Stationary	Dist. To WCL (mm)	Chain Model	PWHT	Illustrative information	RSM Results (MPa)				Observations
									σ_x max	σ_y min	σ_y max	σ_y min	
1.	1F	F_H	TL	-	-	Hero	-		-41	-544	-431	-31	
2.	1F	F_H	TL	-	-	Hero	-		-12	-374	-15	-337	
3.	2F	F_H	BL	-	-	Hero	-		-	-	-	-	Shot peened condition - Similar RS field in all locations
4.	2F	F_H	BL	-	-	Hero	-		-	-	-	-	Shot peened condition - Similar RS field in all locations
5.	3F	F_H	LS	-	-	Hero	-		-	-	-	-	Shot peened condition - Similar RS field in all locations
6.	3F	F_H	LS	-	-	Hero	-		-60	-560	50	-352	
Minimum Number of Samples (F_H) – Half Chain Links													
3													
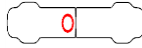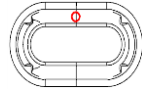
7.	1A	A$_H$	TL	M	3	Hero	-		236	-98	-27	-352	
8.	1A	A$_H$	TL	M	23	Hero	-		-41	-455	-130	-409	Sample 1A can be used to measure far from the WCL. Distance between measurements ≥20mm
9.	1A	A$_H$	TL	S	-23	Hero	-		-82	-334	-90	-585	If S and M are symetric the next measurement can be carried out only either on S or M
10.	2A	A$_H$	TL	S	-3	Hero	-		249	-18	-63	-246	
11.	3A	A$_H$	TR	S	-3	Hero	-		195	-43	16	-195	
12.	3A	A$_H$	BL	M	23	Hero	-		-	-	-	-	Obtained symmetry – not necessary to perform on both S and M
13.	3A	A$_H$	BL	S	-23	Hero	-		-	-	-	-	If the results are symmetric to 1A the next measurement can be carried out only on S or M

14.	4A	A_H	BL	S	-3	Hero	-		261	-49	-116	-331	
15.	5A	A_H	LS	M	3	Hero	-		49	-279	-104	-388	
16.	5A	A_H	LS	M	23	Hero	-		-28	-475	-106	-521	Sample 5A can be used to measure far from the WCL. Distance between measurements ≥20mm
17.	6A	A_H	LS	S	-23	Hero	-		-60	-311	-58	-321	
18.	6A	A_H	LS	S	-3	Hero	-		95	-126	-91	-490	

Minimum number of samples (A_H) – **Half chain links**

12

19.	1N	N_H	TL	M	3	Hero	-		254	-10	-113	-320	
20.	1N	N_H	TL	M	23	Hero	-		-86	-233	-146	-358	Sample 1N can be used to measure far from the WCL. Distance between measurements ≥20mm

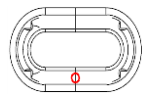|													
21.	1N	N$_H$	TL	S	-23	Hero	-		-98	-407	-108	-578	If S and M are symetric the next measurement can be carried out only either on S or M
22.	2N	N$_H$	TL	S	-3	Hero	-		257	-143	33	-412	
23.	3N	N$_H$	BL	M	3	Hero	-		-	-	-	-	
24.	3N	N$_H$	BL	M	23	Hero	-		-	-	-	-	
25.	3N	N$_H$	BL	S	-23	Hero	-		-	-	-	-	If the results are symmetric to 1N the next measurement can be carried out only on S or M
26.	4N	N$_H$	BL	S	-3	Hero	-		-	-	-	-	
27.	5N	N$_H$	LS	M	3	Hero	-		224	-87	-122	-290	
28.	5N	N$_H$	LS	M	23	Hero	-		-53	-346	-112	-357	Sample 5N can be used to measure far from the WCL. Distance between measurements ≥20mm

No.													
29.	6N	N_H	LS	S	-3	Hero	-		113	-110	-118	-371	
30.	6N	N_H	LS	S	-23	Hero	-		-31	-441	-8	-357	
31.	7N	N_H	LS	-	0	Hero	-		-	-	-	-	It was not possible to measure in the WCL since it was impossible to make the surface flat
32.	8N	N_H	BL	-	0	Hero	-		-	-	-	-	It was not possible to measure in the WCL since it was impossible to make the surface flat
33.	8N	N_H	TL	-	0	Hero	-		-	-	-	-	Sample 5N can be used to measure TL

Minimum number of samples (N_H) – **Half chain links**

16

No.													
34.	1P	P_H	TL	M	3	Hero	✓		-33	-637	-14	-569	
35.	1P	P_H	TL	M	23	Hero	✓		-42	-600	-16	-562	Sample 1P can be used to measure far from the WCL. Distance between measurements ≥20mm

36.	1P	P$_H$	TL	S	-23	Hero	✓	(diagram)	-35	-617	-65	-602	If S and M are symetric the next measurement can be carried out only either on S or M
37.	2P	P$_H$	TL	S	-3	Hero	✓	(diagram)	24	-538	-12	-667	
38.	3P	P$_H$	BL	M	3	Hero	✓	(diagram)	-	-	-	-	
39.	3P	P$_H$	BL	M	23	Hero	✓	(diagram)	-	-	-	-	
40.	3P	P$_H$	BL	S	-23	Hero	✓	(diagram)	-	-	-	-	If the results are symmetric to 1P the next measurement can be carried out only on S or M
41.	4P	P$_H$	BL	S	-3	Hero	✓	(diagram)	-	-	-	-	
42.	5P	P$_H$	LS	M	3	Hero	✓	(diagram)	2	-394	14	-437	
43.	5P	P$_H$	LS	M	23	Hero	✓	(diagram)	-7	-510	8	-489	Sample 5P can be used to measure far from the WCL. Distance between measurements ≥20mm

44.	6P	P_H	LS	S	-3	Hero	✓		-39	-391	18	-416	
45.	6P	P_H	LS	S	-23	Hero	✓		-39	-611	-59	-602	
46.	7P	P_H	LS	-	0	Hero	✓		-	-	-	-	It was not possible to measure in the WCL since it was impossible to make the surface flat
47.	8P	P_H	BL	-	0	Hero	✓		-	-	-	-	
48.	8P	P_H	TL	-	0	Hero	✓		-	-	-	-	Sample 5P can be used to measure TL

Minimum number of samples (P_H) – **Half chain links**

16

Minimum total hero samples = 3 (F_H) +12 (A_H) +16 (N_H) +16 (P_H) = 51 half chain links